This volume is the property of the University of Oklahoma, but the literary rights of the author are a separate property and must be respected. Passages must not be copied or closely paraphrased without the previous written consent of the author. If the reader obtains any assistance from this volume, he or she must give proper credit in his own work.

I grant the University of Oklahoma Libraries permission to make a copy of my thesis/dissertation upon the request of individuals or libraries. This permission is granted with the understanding that a copy will be provided for research purposes only, and that requestors will be informed of these restrictions.

NAME [redacted]

DATE 09/25/2013

A library which borrows this thesis/dissertation for use by its patrons is expected to secure the signature of each user.

This thesis/dissertation by PRIYAVRAT SHUKLA has been used by the following persons, whose signatures attest their acceptance of the above restrictions.

NAME AND ADDRESS	DATE

UNIVERSITY OF OKLAHOMA

GRADUATE COLLEGE

NANOINDENTATION STUDIES ON SHALES

A THESIS

SUBMITTED TO THE GRADUATE FACULTY

in partial fulfillment of the requirements for the

Degree of

MASTER OF SCIENCE

By

PRIYAVRAT SHUKLA
Norman, Oklahoma
2013

NANOINDENTATION STUDIES ON SHALES

A THESIS APPROVED FOR THE
MEWBOURNE SCHOOL OF PETROLEUM AND GEOLOGICAL ENGINEERING

BY

[redacted]

Dr. Chandra Rai, Chair

[redacted]

Dr. Carl Sondergeld, Co-Chair

[redacted]

Dr. Deepak Devegowda

Dedicated to my parents

Acknowledgements

I would like to begin by thanking the almighty who has made everything possible. I deeply thank my family for their constant support and trust while I pursued my studies. Their constant inspiration, boundless love and affection have helped me achieve this.

I express my sincere gratitude to my advisors Dr. Chandra Rai and Dr. Carl Sondergeld for their guidance during the course of my thesis. I thank them for giving me time from their busy schedule for evaluating my work and giving invaluable suggestions. They are a constant source of motivation and an immense source to learn from. I can only dream of achieving their level of excellence in this field. Successful completion of my thesis were possible without their support. I also thank Dr. Deepak Devegowda for his help and guidance during my studies at OU. Get-togethers at his home very were enjoyable.

I want to express my sincere thanks to Mark Curtis, Gary Stowe, Jeremy Jernigen, Bruce Spears and Aravinda for making my lab work more comfortable. They never let shortage of resources come in way of my research work. Any new thing I wanted was made available by Gary and Jeremy never let any machine ill-perform. MPGE staff also played a big role in making the road to my education smooth.

I wholeheartedly thank the Unconventional Shale Gas Consortium and Experimental Rock Physics Consortium members for their invaluable suggestions and financial support to make this research possible.

Last but not the least I want to thank all my friends: Abhijeet, Adi, Dongre, Eric, Govindu, Himanshu, KV, Sarvesh, Shantanu, Subbu and Vineet who were my family here and made my stay in Norman delightful and enjoyable. They have made an immense contribution in my success.

Table of Contents

List of Tables

List of Figures

Abstract

Shale resources promise a new era for energy independence of United States. The promise is intrinsically tied to our ability to economically hydraulic fracture the shale. These extremely tight formations are impossible to produce without hydraulic fracturing, which in turn requires knowledge of mechanical properties of rocks. However, the chemical and mechanical instability of shales sometimes prohibits the recovery of full length cores and/or plugs necessary for conventional mechanical testing. Nanoindentation provides a means to study the mechanical properties of these rocks (essentially the Young's modulus and hardness) using smaller specimen, even drill cuttings, fragments and sidewall cores. The measurements obtained are accurate and reliable and agree well with dynamic measurements. Additionally, the ability of measuring over the whole pay zone through drill cuttings helps in improving hydraulic fracturing design. The technique was essentially developed to measure mechanical properties of small materials and thin films. This thesis focuses on the applicability of nanoindentation in shales. It also attempts to develop a correlation to estimate rock mechanical properties based on the measurements of principal rock components which affect its mechanical behavior; these components include mineralogy, porosity and organic content. Seven different shales comprising a total of 276 samples were tested in this study. Porosity, TOC and mineralogy were measured on all the samples, followed by nanoindentation testing. Nanoindentation testing was carried out in horizontal as well as vertical directions thus enabling the determination of anisotropy in Young's modulus. Vertical Young's modulus ranged between 11 to 93 GPa while horizontal Young's modulus ranged between 30 to 93 GPa. Average ratio of horizontal to vertical modulus was found to be 1.64. Vertical hardness ranged between 0.36 to 6.98 GPa while horizontal hardness ranged between 0.48 to 6.67 GPa.

The precise measurement capability of nanoindenter enables to study the rock frame and organic content separately. Studies were conducted on kerogen to understand the effect of porosity and maturity on the organics. Samples of different organic porosities and maturities were tested. Average Young's modulus in organics was found to be 4 times lesser than that of matrix. This thesis also highlights the variation in mechanical properties when measured on rocks for which bedding directions are known versus randomly oriented simulated drill cuttings. Hydrocarbons are generated and stored at great depths below the Earth's surface. Measurements at high temperatures form another component of this study to understand the effect of temperature on Young's modulus and indentation hardness. 20 samples tested at 100 °C showed an average increase of 0.1% in Young's modulus from the values at room temperature. Effect of grain size on nanoindentation results is another aspect investigated in this thesis. Results are encouraging and have proved the applicability of nanoindentation on drill cuttings in heterogeneous rocks like shales.

CHAPTER 1: INTRODUCTION

1.1: US Shale Oil and Gas Industry

Production from shales has surpassed our understanding of them. The fact that shales contain oil and gas was known ever since oil and gas industry started developing. Low porosity and ultralow permeability of these fine grained rocks limited their importance to being mere seal rocks for conventional reservoirs. With the advent of precise methods for horizontal drilling and developments in hydraulic fracturing, commercial production from shales has become a reality and has turned shales in economic resources. In the US with over a million shale wells have been drilled and hydraulically fractured. Figure 1 shows a map of current and prospective shale plays in the US.

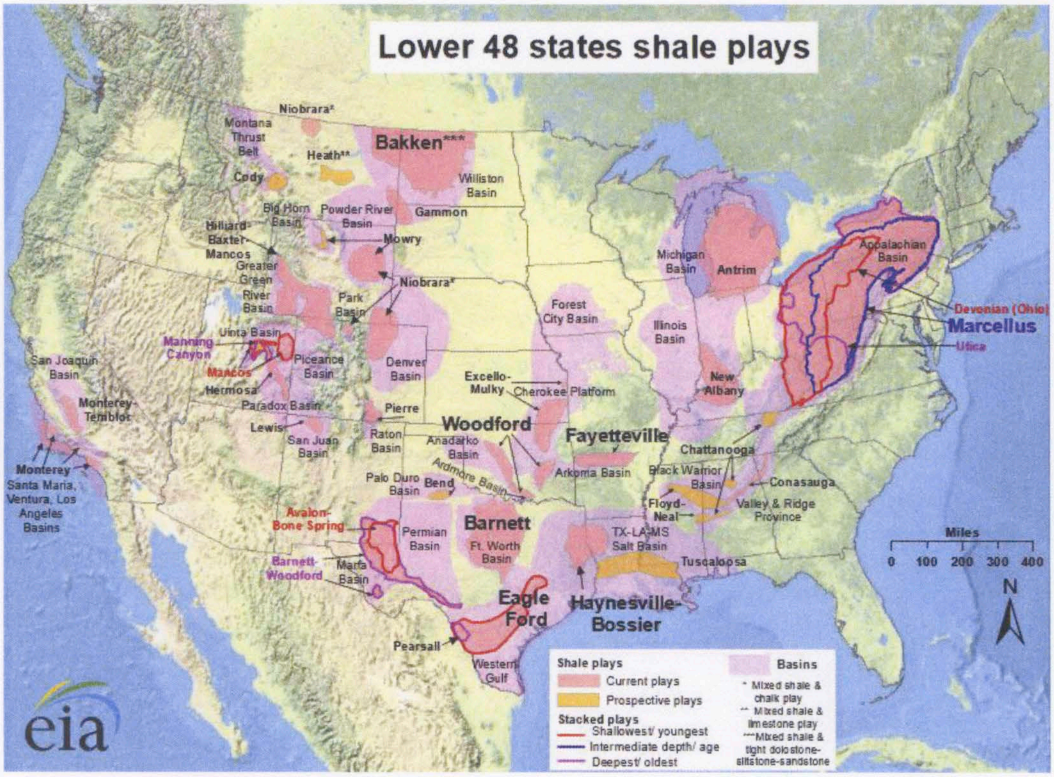

Figure 1: Map of current and prospective shale resources in the lower 48 states of the US (source: www.eia.gov).

According to Annual Energy Outlook 2013 published by EIA, the US natural gas production will rise from 23 trillion cubic feet (TCF) in 2011 to 33.1 TCF in 2040, which will be mostly dominated by increased shale contributions. As of January 2011, INTEK, Inc. estimated 750 TCF of shale gas resources in the lower 48 states. Most of this gas will come from the Marcellus, Haynesville and Barnett shales. Figure 2 presents US natural gas production trend starting from 1990 projected up to 2040.

INTEK, (2011), estimates the shales oil resources stand at 23.9 billion barrels in the lower 48 states. The major shale plays contributing to this production will be Monterey/Santos, Bakken and Eagle Ford. Pollastro et al., (2008), estimate an undiscovered volume of 3.65 billion barrels of oil, 1.85 tcf associated/dissolved natural gas and 148 million barrels of NGL in the Williston basin of Montana and North Dakota.

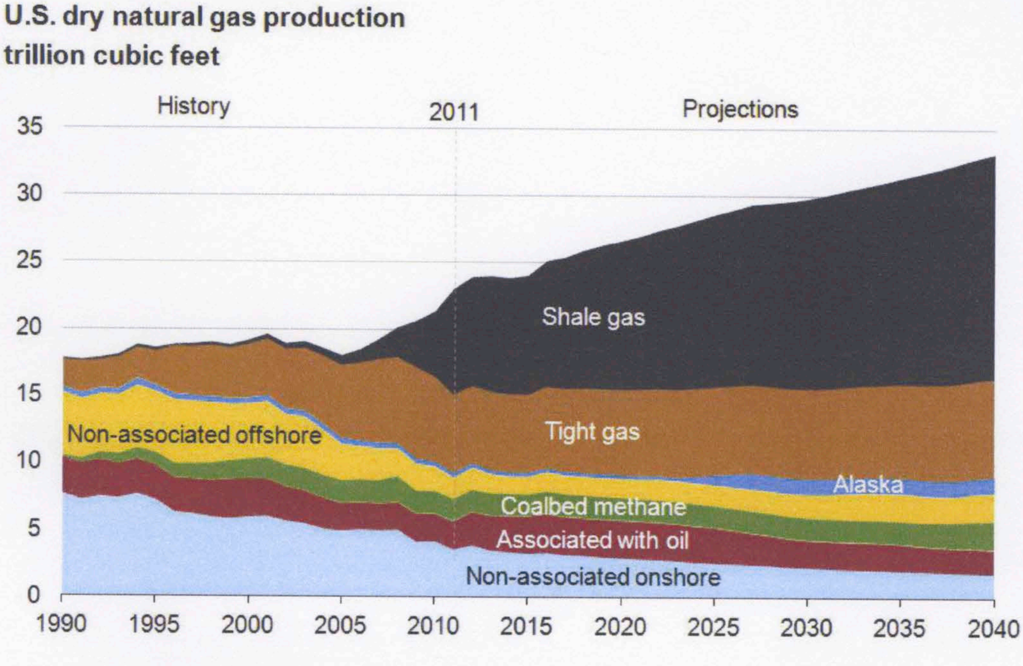

Source: U.S. Energy Information Administration, *Annual Energy Outlook 2013 Early Release*

Figure 2: US natural gas production trend from 1990 projected up to 2040 (EIA, 2013). Contribution from shale gas production dominates the increase.

1.2: Introduction to Shales

Shales are the most abundant sedimentary rock. They are fine grained clastics and carbonates within which hydrocarbons are commonly generated and are characterized by low matrix porosity and permeability. Complex microstructure also make them very different from conventional reservoirs as shown in Figure 3 which demonstrates the differences in shales, sandstones and carbonates at micron scales. Variability in mineralogy and organic content makes each shale different from the other. Each shale may be different in its geology, geochemistry and geomechanical properties and will require unique drilling, completion and production techniques (Cramer, 2008). "Shales vary aerially and vertically within a trend, even along a wellbore" (King, 2010).

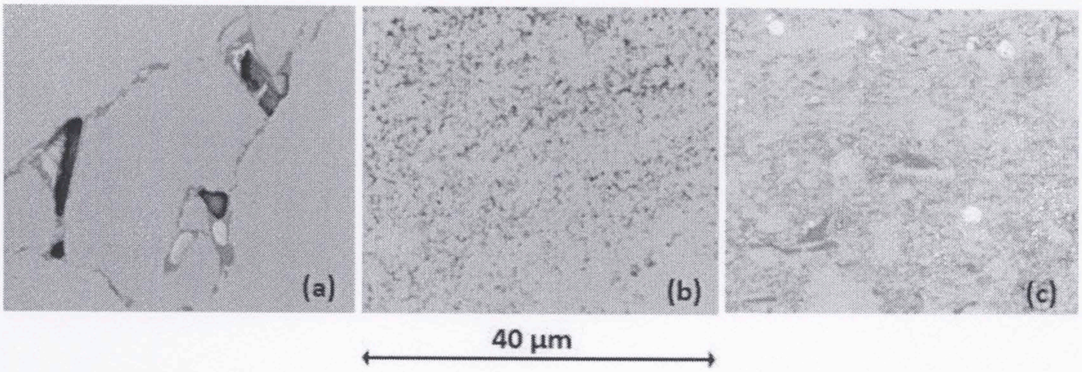

Figure 3: Scanning Electron Microscopy images of a sandstone (a), carbonate (b) and shale (c) showing difference in microstructure of the three rocks.

Shales are thinly laminated with interbedding of siltstone and sandstone. Interlinking these laminations and opening existing natural fractures could be an efficient way to produce from shales. Higher clay content in shales makes them anisotropic (Mba and Prasad, 2010) which leads to errors in interpreting well log data and corresponding calculations of mechanical properties. Hydraulic fracture designs can be adversely by ignoring anisotropy. Sayers, (2008), emphasize "understanding of shale anisotropy is important to obtain reliable information of reservoir fluid, lithology and pore pressure from seismic data, and to understand time-to-depth conversion errors and non-hyperbolic moveout". This could lead to drilling of dry holes (Sondergeld et al., 2000). Scanning Electron Microscopy (SEM) work by Curtis et al., (2012) suggest presence of organic as well as inorganic porosity in shales. Organics will have a propensity to be oil wet whereas inorganics tend to be water wet. Considerable hydrocarbons will be contained in very small sized pores where hydrocarbon phase behavior can be entirely different. These pores can hold large quantities of free and adsorbed gas (Ambrose et al., 2011) that can be recovered using modern drilling and completion techniques. Production trends in Barnett shale indicated a growth from 94 MMSCFD to 3 BSCFD in 10 years (NCI, 2008), during which major advances in shale gas drilling and completion were made. Understanding pore size distribution in shales is therefore very important. Magnetic Resonance Imaging (MRI), Mercury Injection Capillary Pressure (MICP), CT scans and SEM are being used to understand the complex network within shales. Work is ongoing across various laboratories to develop techniques for petrophysical characterization of shales. Laboratory studies are also affected by challenges in obtaining and preserving samples for testing.

1.3: Shale Deposition, Maturity and Quality

Sediments get deposited in basins through the work of exogenic forces like rivers, oceans, lakes, wind and glaciers. Due to continuous deposition of sediment above, they get buried and the process of thermal maturation of organic matter begins for the generation of hydrocarbons. This process as explained by Hunt, (1979), initiates with diagenesis that occurs after burial to a few hundred feet at temperatures less than 122 ^{o}F. During this process, buried sediments and organic matter (primarily lipids from animal tissue and plant matter, or lignin from plant cells) undergo changes in composition and texture due to cooking under temperature, pressure and microbial action. Some biogenic gas is generated during the process. Catagenesis takes place at temperatures between 122 and 302 ^{o}F when hydrocarbons, both oil and gas are generated owing to the disintegration of kerogen and clays. Metagenesis is the last step in maturation which takes at temperatures between 302 and 392 ^{o}F. Dry gas and some non-hydrocarbon gases are left at the end of this process after cracking of oil molecules. Biogenic gas is usually a very small fraction of total gas contained in the shale as confirmed by isotopic characterization of produced gases (Hunt, 1979). Generally, as maturity increases the thermogenic gas content in a shale increases. Rocks with higher TOC and thermal maturity are better producers of oil and gas (Jarvie et al., 2004). As the atomic hydrogen-to-carbon (H/C) ratio of organic matter increases, the quantity of expelled hydrocarbons increases (Hunt, 1979).

Common ways to measure organic maturity are vitrinite reflectance (Ro) and rock pyrolysis (T_{max}). R_o works much better in gas window while T_{max} gives better results in oil window. Espitalie et al., (1985), has presented a relationship between R_o and T_{max}. Other ways like spore coloration index (SCI) and weight% carbon in kerogen, Thermal Coloration Index (TAI) are also used to quantify maturity. Figure 4 shows the various scales for a comparison between different maturity indices. Thermogravimetric analysis is also being keenly studied as an index to describe rock maturity.

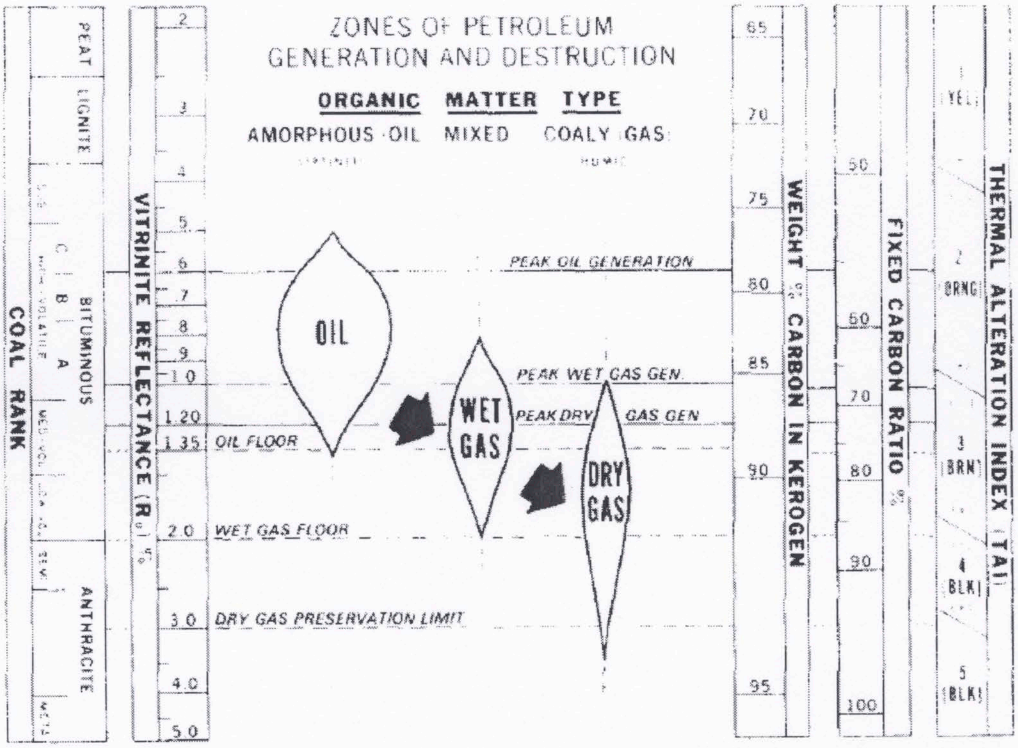

Figure 4: Comparison of several commonly used maturity indices and their correlation to oil and gas generation and destruction limits (reproduced from Dow, 1977).

Maturity of a shale alone does not make it prospective. Total organic carbon (TOC) in the rock will determine the volume of hydrocarbons available inside. TOC of less than 0.5 weight% is considered poor and that of more than 5 weight% is considered excellent. Measuring TOC in a rock sample is possible using laboratory methods.

Shales are fissile and break along thin laminae or parallel bedding. Some shales may be naturally fractured; these fractures may be closed or open. Due to ultralow matrix permeability, shales are usually hydraulically fractured which can also open existing natural fractures within the shale. Recovery factors from shale reservoirs are estimated to be low, 5% to 20% (Faraj et al, 2004), but better fracture designs can result in higher recovery factors.

1.4 Motivation

US oil and natural gas industry has seen a resurgence with shale resource development. Many of the wells in exploratory stages are cored and logs are run for understanding what is present downhole. One of the objectives of doing this is to obtain mechanical properties of the formation drilled. Such measurements then assist in designing hydraulic fractures and to counter wellbore instability problems commonly encountered while drilling in shales. Development wells are not always cored but sonic logs are run. Coring is an expensive procedure and it is not always possible to recover a full sized core in shales due to their chemical and mechanical instability. Subsequently taking core plugs (1 inch diameter) required for mechanical testing may also be challenging. Sonic log data also does not come cheap and high anisotropy in shales may affect the mechanical properties derived from this data. But it is always possible to obtain small fragments and sidewall cores from the wells. If nothing else can be recovered, cuttings are always generated during drilling at no additional cost. If fragments, sidewall cores and drill cuttings can be used to obtain Young's modulus of rocks then it will result in a considerable cost saving. Nanoindentation offers such a possibility. Drill cuttings are available at all depths so measurements can be carried out along the length of the well. At places where no other mechanical property data is available, nanoindentation data can be used as a reliable surrogate.

Shales have variable mineralogy and mechanical properties of organics and clays have always remained elusive. Most measurements of properties of organics were made by dissolving the rock matrix (Zeszotarski et al., 2004). This subjectivity has also led to uncertainty in predicting seismic properties of shales since properties of individual components are not well understood (Ahmadov, 2009).

Hydraulic fracturing requires inputs such as Young's modulus, closure stress gradient, Poisson's ratio, fracture toughness and rock type etc. Nanoindentation can also provide hardness of a rock which are useful in understanding proppant embedment.

This study was undertaken with the following objectives:

1. To understand the relationship between basic petrophysical properties of shale and its Young's modulus and hardness.
2. To compare nanoindentation Young's modulus (E_i) with dynamic Young's modulus (E_d) for shales.
3. To establish applicability of nanoindentation to obtain meaningful mechanical data from simulated drill cuttings.
4. To understand the effect of temperature on elastic modulus and hardness in shales.
5. To understand the elastic properties of organics and relate these properties to organic porosity and thermal maturity by testing organics from different maturity windows.
6. To understand the variation in Young's modulus with hydraulic fracture density.

1.5 Synopsis

This study is divided into 5 chapters. Chapter 1 gives an introduction for the study and the motivation behind it. Chapter 2 discusses the theory and principles behind nanoindentation testing. Chapter 3 covers the experimental procedures in carrying out petrophysical measurements and nanoindentation testing. Chapter 4 summarizes the relevant results and discusses their applicability. Finally in Chapter 5 we conclude the findings from our studies.

CHAPTER 2: LITERATURE REVIEW

After several years of production from shale resouces, a new understanding about exploration from these systems has developed. Though mature enough, it is still in its nascent stage. Precise techniques like Leco TOC, Rock Eval, LPP, FTIR, XRD, NMR, TGA, SEM, dynamic testing, nanoindentation, ion milling, hydraulic fracturing, well logging etc., were developed or adapted from other domains to characterize shales. Some of these techniques are discussed in subsequent pages.

This chapter reviews the existing state of knowledge in shales. It describes the structure, mineralogy and geochemistry of shales. Some frequently carried out lab measurements on shales which are a part of this study are explained. It also discussed the principle and technique of nanoindentation and what makes it so applicable to shales. Some challenges and sources of error are also covered.

2.1 Mudrocks and Shales

Mudrocks are fine grained siliciclastic sedimentary rocks which include siltstone, claystone, mudstone and shale. They are the most abundant (50-80 vol%) sedimentary rocks on the Earth's crust (Prothero and Schwab, 2004). They are predominantly silt (6.25 μm to 3.9 μm) and clay (<3.9 μm). Shales are a class of mudrocks in which clay minerals are aligned and laminated. Laminations also make shales more fissile compared to other mudrocks, causing them to break and peel off along bedding plane very easily. In general terms, shales are fine grained sedimentary rocks having particle size less than 4 microns. Common clay minerals in sedimentary rocks are kaolinite, illite, chlorite, smectite and mixed clay containing illite and smectite. Features common to all clay minerals are their small crystal size, complex and variable mineralogy, instability, reactiveness and varied growth habit (Rai and Sondergeld, PE 6283, 2011). Shales are deposited in low energy environments in deep sea or in continental shelf with relatively deep water. They have preferential alignment of minerals in the form of sheets which can be 0.5mm (papery parting) to 10mm (slabby) thick (Prothero and Schwab, 2004). A typical shale contains 30% quartz, 10% feldspar, 50% clay and 10% carbonates or iron oxide (Boggs, 1992).

2.2 Clay Structure

Prothero and Schwab, 2004 have discussed clay minerals as hydrous aluminum phyllosilicates containing variable amounts of iron, magnesium, alkali metals, alkaline earth metals and some cations. Al^{3+} in some clays can be easily replaced by Fe^{2+} or Mg^{2+} leading to a net negative charge which makes the clay reactive. Negative charge is neutralized by water thus explaining high water absorbing capacity of clays. Clay minerals are classified having two dimensional sheets of corner sharing SiO_4 and/or AlO_4. Some clays are more reactive than others depending on the net charge present on them. Kaolinite has tight bonding of layers with hydrogen cations between them which inhibit water from entering and expanding the clay. Illite has a 2:1 structure but strong ionic bonding between layers is imparted by potassium making them less reactive to water. Smectite (montmorillonite) structure is very expandable due to the presence of smaller charge. These clays can double in volume once they absorb water. Chlorite has 2:1 structure but is not very reactive to water due to the presence to Mg^{2+} and Fe^{2+} ions between the layers (Prothero and Schwab, 2004).

2.3 Geochemical Analysis of Shales

Industry has used geochemical analysis to determine shale quality and its oil and gas potential. Some methods developed for such an analysis are discussed in this section.

2.3.1 Kerogen and Types of Kerogen

As discussed in Chapter 1, shales contain considerable amount of organic matter which makes it a source rock. When shales are buried, kerogen is formed by decomposition of organic matter which may be terrestrial or aquatic. Based on the origin and age of organic matter it may have more plant matter or animal matter. This forms the basis of classification of kerogen. Table 1 shows different types of kerogen, their origin and hydrocarbon potential. Type I kerogen has high hydrogen to carbon (H/C) ratio (>1.3) and low oxygen to carbon (O/C) ratio (<0.1). Type III kerogen instead has low H/C ratio (<1.0) and high O/C ratio (>0.2). Type II kerogen is known to generate both oil and gas. While type IV kerogen mostly produces coal. This is better expressed using a Van Krevelen diagram as presented in Figure 5.

Table 1: Classification of kerogen based on its environment, type, form, origin and hydrocarbon potential (Adapted from NExT notes, 2008).

Environment	Kerogen type	Kerogen Form	Origin	Hydrocarbon Potential
Aquatic	I	Alginite	Algal bodies	Oil
		Amorphous kerogen	Structureless debris of algal origin	
	II		Structureless planktonic material, primarily of marine origin	
Terrestrial		Exinite	Skins of spores and pollen, cuticle of leaves and herbaceous plants	
	III	Vitrinite	Fibrous and woody plant fragments and structureless, colloidal humic matter	Gas, some oil
				Mainly gas
	IV	Inertite	Oxidized, recycled woody debris	None

2.3.2 Total Organic Carbon in Shale

Total organic carbon is commonly abbreviated as TOC and is a measure of weight percent of organic carbon. 1 wt. % TOC means 1 gram of organic carbon in 100 gram of sample (Jarvie, 1991). Measurement of TOC is the first step to assess the potential of a source rock to generate hydrocarbons. TOC is divided in three categories: the extractable organic matter (EOM), the convertible and the residual carbon (Jarvie, 1991). EOM is the already formed hydrocarbon present in the rock. Convertible carbon has not yet been converted to hydrocarbons but has the potential to form hydrocarbons under right pressure and temperature conditions. Residual carbon does not have any hydrocarbon generating potential.

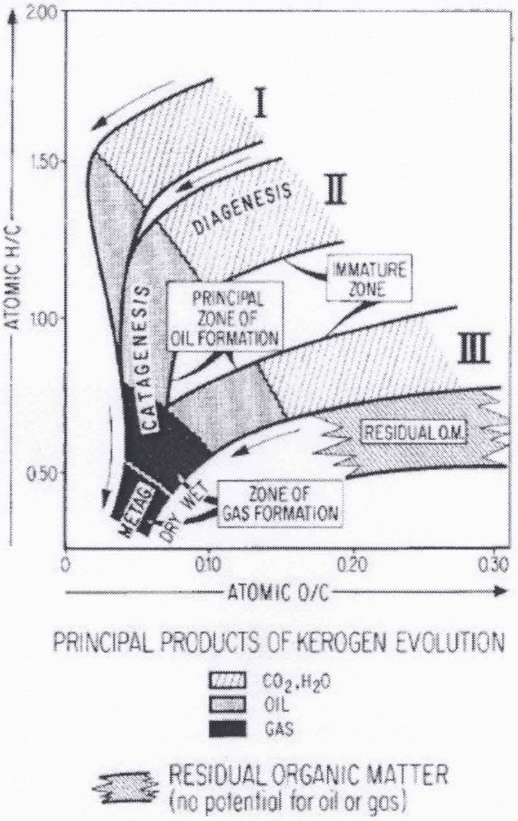

Figure 5: Van Krevelen diagram presenting various kerogen types on H/C versus O/C axes and showing products of maturation. (Tissot et al., 1980).

2.3.3 Rock Eval Pyrolysis

Rock Eval pyrolysis experiments are used to quantify TOC as well as to establish the type of kerogen present inside the rock. Source Rock Analyzer™ (SRA) by Weatherford Laboratories is one such instrument designed to identify and characterize source rock by heating samples to a programmed temperature in an inert atmosphere. Figure 6 presents a schematic of SRA output.

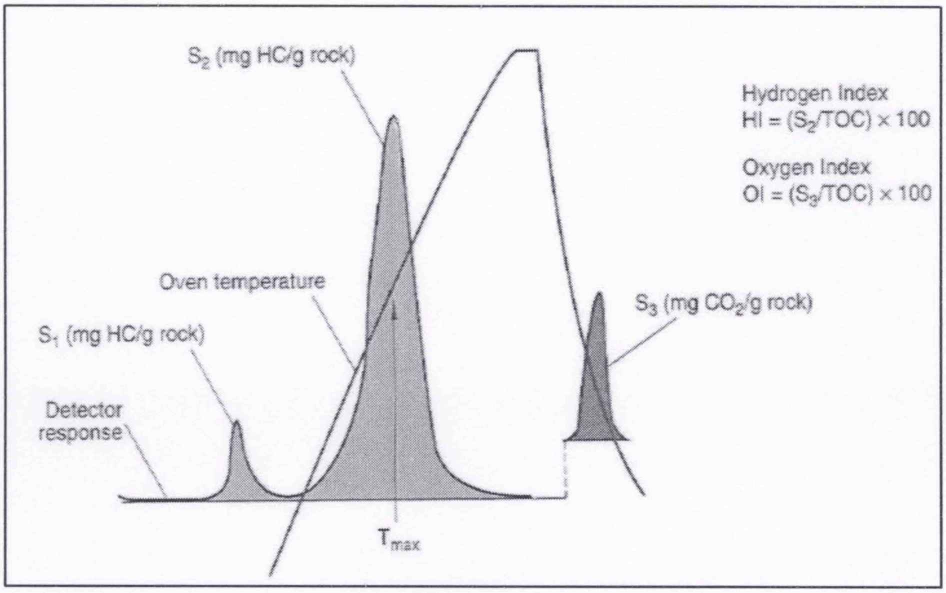

Figure 6: A pyrogram showing hydrocarbon and CO_2 evolution from a rock sample during pyrolysis experiment (increasing time and temperature from left to right). Hydrogen and oxygen indices are calculated as shown (Hunt, 1996).

SRA quantitatively determines the amount of free hydrocarbons (S_1) and the amount of hydrocarbons generated by thermal cracking of nonvolatile organic matter (S_2) using flame ionization detector (FID). Pyrolysis of kerogen results in production of CO_2 upto a temperature of 400°C (S_3) which is determined using infrared (IR) detectors. The temperature at which maximum hydrocarbons are released from cracking of kerogen during pyrolysis is called T_{max}.

2.3.4 Vitrinite Reflectance

Vitrinite reflectance (R_o) is a widely used indicator of thermal maturity because its applicability extends over a long maturity range. Kerogen in shales can be divided into four macerals; alginite, exinite, vitrinite and inertite, which were shown in Table 1. Vitrinite comes from plant material present in the source rocks. Vitrinite reflectance is an optical technique which is based on the change in the reflectance of light from a polished surface of vitrinite. About ten to twenty measurements need to be carried out for a reasonable estimate of R_o measured in percentage which refers to the fraction of incident light that is reflected back to the microscope. With greater maturity molecular structure of the maceral changes and more light is reflected (Hunt, 1996) hence R_o is higher. Figure 7 shows vitrinite of three different maturity levels from Barnett shale as reported by Jarvie, (2004).

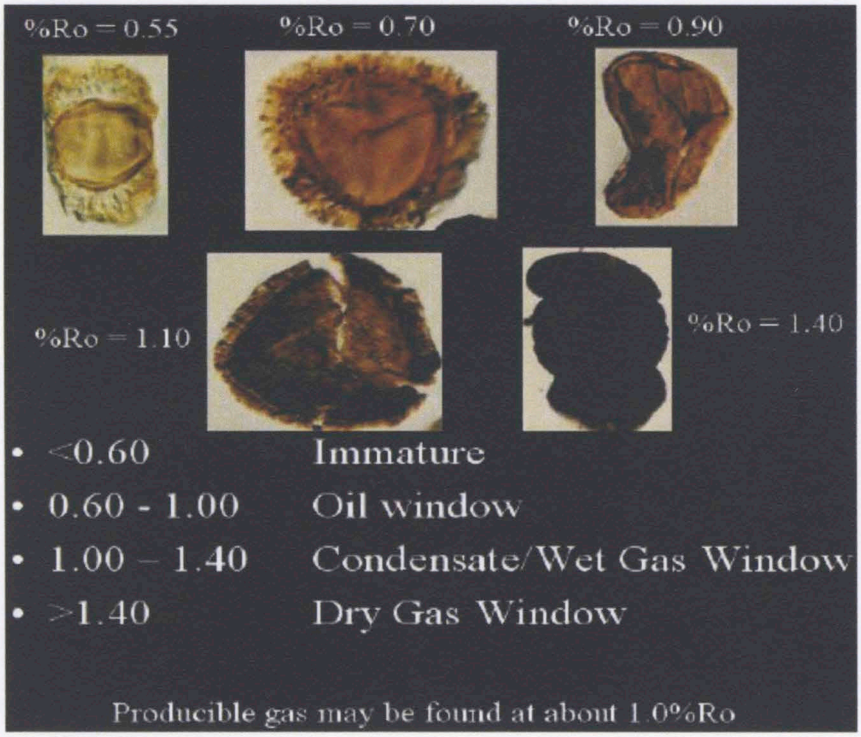

- <0.60 Immature
- 0.60 - 1.00 Oil window
- 1.00 – 1.40 Condensate/Wet Gas Window
- >1.40 Dry Gas Window

Producible gas may be found at about 1.0%Ro

Figure 7: Barnett shale samples from different maturity (%R_o) levels. Samples with R_o above 1.0% are thermally mature and have potential to produce commercial hydrocarbons (Jarvie, 2004).

2.3.5 Thermogravimetric Analysis and FTIR Gas Analysis

Thermogravimetric analysis (TGA) is based on continuous measurement of the change in sample weight which is exposed to linearly rising temperature. The effluent gases released during the heating process are analyzed using FTIR (discussed in Chapter 3). A small amount of finely powdered sample (40 mg) is used for this test. The rate of heating is usually set to 4°C/min. The results of the test are influenced by the sample quantity, ambient atmosphere and rate of heating. Hence these parameters should be standardized for all the samples to be tested. The result for TGA analysis is represented in the form of a thermogram and is divided in three stages. Stage 1, weight loss at T < 350 °C. There is an accelerated change in weight in stage 2 from 350 to 500°C which displays an inflexion point. Stage 3 extends up to 600°C, over which there are slight changes in weight (Durand, 1980). Sometimes a faster change in weight is observed during stage 1. TGA helps to determine type of kerogen and its oxygen or hydrogen richness.

2.4 Comparison between Indentation Hardness and Conventional Hardness

Hardness as previously mentioned is the ratio of indenter load to the projected area of contact, and measures the resistance of a material to permanent deformation. It is classified in two types: microhardness (load < 1kg) and macrohardness (load > 1kg), Kaufmann (2003). Indentation hardness (H_{IT}) is a microhardness and it is measured when the indenter is pressed against the specimen at peak load. Knoop hardness is also microhardness. On the other hand macroharndess tests such as Brinell Hardness Number (BHN) measure hardness after the load is released. Rockwell hardness and Vickers hardness are also macrohardness. Hardness is not considered as a fundamental property of a material, but it is useful as a qualitative tool to differentiate materials (Kaufmann, 2003). Deeper indentations are produced in softer materials while harder materials produce shallower indentations. Kaufmann (2003) have discussed the criteria for selecting any particular test for a material based on the following parameters

- Hardness range of the material to be tested
- Surface condition (roughness)

- Whether or not the work piece can be modified prior to testing
- Homogeneity/heterogeneity of the material
- Number of tests to be performed
- Level of automation available

"Hardness values can be directly compared only of the same test is used, since the geometry of the indenter and force applied influence the outcome of the test. For each type of hardness test conducted, a different equation is used to convert the measured dimension, depth or diameter, to a hardness value" Kaufmann (2003).

For rigid-plastic solids where there is negligible elastic recovery, the H_{IT} and BHN should match. For substances such as ceramics or rubber, the ratio of Young's modulus to hardness (E/H) is low, the measure of H_{IT} is the combined effect of elastic and plastic deformations.

The reason indentation hardness is measured at peak load is that it is very difficult to image a nanoindentation impression to calculate its area. Such a problem is not encountered in calculation of BHN because the diameter of indenter sphere is 10 mm which creates a sufficiently large impression which can be imaged with an optical microscope. Also the loads used are 500 to 3000 kg which are applied for 30-60 seconds. BHN is expressed by the following expression presented in www.engineeringtoolbox.com:

$$\mathrm{BHN} = \frac{2P}{\pi D(D-\sqrt{D^2-d^2})} \qquad (2.1)$$

where, D is the diameter of indenter (mm), and d is diameter of contact circle at full load (mm). P is the applied load in kg. Figure 8 shows a schematic of Brinell hardness test.

Nanoindentation also has the advantage that it can be used to investigate mechanical properties of thin films and small individual components such as organics, and other minerals. At low loads (1-2 mN), these indentations extend only over a few grains and can give an idea about the relative change in modulus over the sample area. At higher loads (300-500 mN), larger areas can be investigated and yield hardness value much closer to macohardness (Kumar, 2012a).

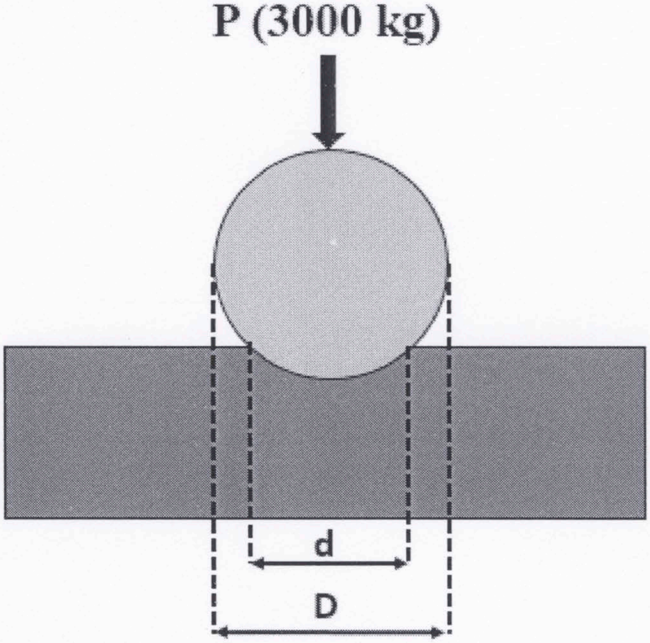

Figure 8: Schematic image of Brinell hardness test showing dimensions ball indenter and loaded specimen. Loads in the range 500-3000 kg are used.

Table 2 provides a comparative idea about hardness of some metals and minerals measured by some commonly used techniques and using nanoindentation. Nanoindentation hardness was measured in this study and by Kumar, (2012a) whereas other hardness values were taken from Kuhn and Medlin (2000), Parker (1967), Kaufmann (2003), Harper (2001) and Taylor and Cooke (1949). It should be noted that macrohardness is not a reliable indicator of hardness of minerals but is often used for a relative idea. Measurement of hardness is important to understand proppant embedment issues in shales; softer shales will be more prone to proppant embedment.

Table 2: Comparison of static indentation hardness of some metals and minerals measured using different techniques arranged in increasing order or Mohs hardness. Quantitatively, hardnesses are in the same sequence as Mohs hardness with a few exceptions.

Metal/Mineral	Brinell Hardness	Mohs Hardness	Nanoindentation Hardness	Vickers Hardness	Knoop Hardness	Rockwell Hardness
Aluminum	0.7-1.5	2-2.9	0.28±0.07	0.8-1.7	-	-
Copper	-	2.5-3	0.92±0.04	-	-	0.4-0.5
Biotite	-	2.5-3	5.37±0.4	-	0.9	-
Calcite	-	3	2.3±0.26	1-1.4	-	1.42
Brass	1.5-1.6	3-4	1.63±0.1	1.7-1.9	-	0.6-0.8
Pyrex	-	6	-	2	-	-
Fused Silica	-	5.3-6.5	9.03±0.07	6.2	-	2.9-5.9
Pyrite	-	6-6.5	11.25±2.5	-	-	-
Quartz	-	7	12.44±0.13	4.7-12.35	7-7.7	-

2.5 Previous Nano-scale Work on Shales

Nanoindentation is a relatively new technique for the Oil & Gas industry. Some researchers have also made use of Atomic Force Microscopy (AFM) to study shales. This section presents a summary of work carried out on shales and organics.

2.5.1 Elastic Properties of Shales

Abousleiman et al., 2007, studied samples from Woodford shale outcrops using nanoindentation. They measured mineralogy using XRD and found samples to be rich in quartz and clay. Porosity was measured using density method after removing organics and was found to be in the range of 16-19% and TOC between 11-18 wt%. Samples for nanoindentation were polished to 0.01 micron roughness. A summary of their results obtained on samples tested in vertical and horizontal directions is presented in Table 3. Generally lower values of Young's modulus were observed in vertical (13.9-

22.9 GPa) as compared to horizontal (16.1-20.6 GPa) directions. However, sample 154/166 display exactly the opposite trend. Indentation hardness ranged from 0.57-0.77 GPa in the vertical direction to 0.65-1.26 GPa in the horizontal direction.

Table 3: Hardness and indentation Young's modulus for Woodford shale (Abousleiman et al., 2007). H1 and H3 denote and hardness, and E1 and E3 denote Young's modulus parallel and perpendicular to bedding, respectively.

Samples	Hardness, GPa		Indentation moduli, GPa	
	H1	H3	E1	E3
131-0	0.67	0.72	17.1	13.9
154-12	0.77	1.17	17.3	21.8
166-0	0.57	1.26	17.7	22.9
175-10	0.77	0.72	20.6	17.0
185-10	0.48	0.65	16.1	16.1

Measured shale anisotropy was related to a multi-scale description of shales by Ortega et al., (2010). They also found agreement between results from acoustic and nanoindentation measurements and similar finding were made by Kumar et al., (2012b), from their study on 61 samples from Woodford, Haynesville and Kimmeridge shales.

Mechanical properties of shales were studied in tandem with mineralogy, porosity and TOC. Such studies can help establish the variation in mechanical properties with changes in rock composition. Aoudia et al., (2010), studied 72 samples of Woodford shale from Tosoba basin in West Texas. 36 different parameters were measured which included density, TOC, compressional and shear velocity, rock moduli, Poisson's ratio, mineralogy and 17 geochemical constituents. TOC, illite, apatite, calcite, and magnesite were found to be the major parameters affecting Young's modulus.

$$\mathrm{E} = -4.23[\mathrm{TOC}] - 0.41[\mathrm{Illite}] + 1.50[\mathrm{Apatite}] + 15.4[\mathrm{Calcite}] - 1.01[\mathrm{Magnesite}] \ldots\ldots \tag{2.2}$$

where, the mineral concentrations [.] are expressed in wt%.

Kumar el al., (2012a) also studied 133 samples from Woodford, Barnett, Haynesville and Eagle Ford shales and presented an equation for Young's modulus, in GPa, as

$$E = 72 - 2.27[\varphi] - 1.83[TOC] - 0.2[Clay] + 0.045[Quartz + Carbonate] \ldots. \quad (2.3)$$

φ is porosity in vol%, and TOC, Clay, Quartz+Carbonate is in wt%. Sondergeld et al., (2000), studied 72 samples from Kimmeridge shale and found P-wave anisotropy parameter (ε) to be strongly correlated with TOC (Figure 9a). Similar findings were also made by Vernik and Liu, (1997) and Vernik and Nur, (1992), for low porosity shales (Figure 9b).

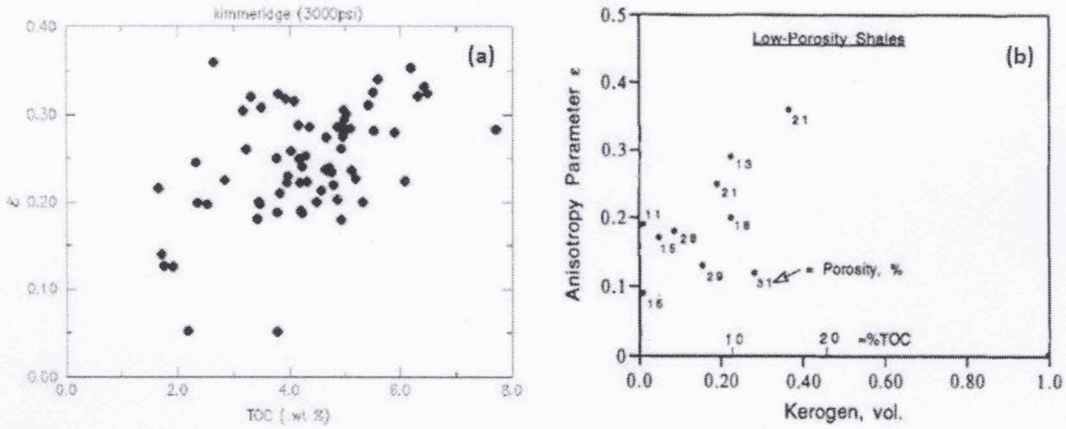

Figure 9: Plots of P-wave anisotropy parameter (ε) versus organic content. (a) Increasing P-wave anisotropy with TOC for 72 Kimmeridge samples (Sondergeld et al., 2000). (b) Increasing P-wave anisotropy with increasing organic content for low porosity shales (Vernik and Liu, 1997).

2.5.2 Elastic Properties of Organics

Zargari et al., (2011), have studied properties of organics using nanoindentation reporting an increase in Young's modulus with maturity. Kumar et al., (2012c), reported decrease in Young's modulus with increasing organic porosity. Curtis et al., (2012) studied organics in 8 Woodford shale samples spanning from 0.51 %R_o to 6.36 %R_o to relate thermal maturity and organic porosity using FIB milling and SEM imaging. They also found presence of fractures inside the organics which were attributed to fracturing of kerogen during oil generation. Both Zargari et al., (2011) and Curtis et al., (2012), have found organics to be stress supporting which makes the study of organics even more important.

Kumar, et al., (2012a) studied Young's modulus in immature (R_o = 0.37%) to highly mature (R_o = 6.3%) organics from Woodford and Kimmeridge shales. They found dependence of Young's modulus on organic porosity with organic modulus lying between 4.7 and 15.3 GPa. Organic porosities in their study ranged between 0 to 11.8%. Zeszotarski et al., (2004) studied organics in Woodford shale samples in vertical and horizontal directions using AFM based nanoindentation technique. The samples used in their study were collected from outcrops and showed TOC of 22 wt% and T_{max} of 421°C. Young's modulus and hardness were measured on three orthogonal faces to see evidence of anisotropy in mechanical properties of organics. Organics were identified using contrast in finishing of polished surfaces of kerogen and harder minerals. While harder materials were found to produce a very smooth surface, organics produce a rippled surface. This contrast was used to image the area of organics in AFM (Figure 10). No conclusive evidence of anisotropy was found in mechanical properties of organics. Along the three faces, hardness ranged from 0.55 to 0.57 GPa and Young's modulus varied between 10.5 to 11.1 GPa.

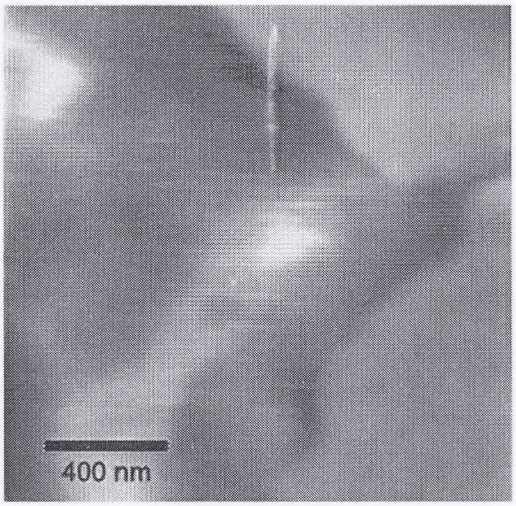

Figure 10: Organic in Woodford shale identified using AFM technique. Rippled region shows presence of organic and smooth surfaces show mineral boundaries (Zeszotarski et al., 2004).

Ahmadov et al., (2009), studied organics in horizontal samples from Bazhenov formation from 3800 m depth with TOC in the range 7 to 21 vol%. They used AFM in combination with confocal laser scanning microscopy (CLSM) and SEM imaging to calculate elastic properties of organic matter. Measured Young's modulus was found to be between 10-15 GPa.

CHAPTER 3: EXPERIMENTAL PROCEDURES

This chapter describes experimental procedures followed for petrophysical measurements of porosity, mineralogy, TOC and acoustic velocity. It also discusses the nanoindentation set up and methodology followed for testing. A description of sample preparation and polishing is presented. SEM imaging which was used to analyze pre and post-indentation data is briefly explained. Various shales studied during the course of this thesis include: Barnett, Eagle Ford, Haynesville, Kimmeridge, Ordovician, Wolfcamp, and Woodford.

3.1 Porosity Measurement

Porosity of a rock quantifies the amount of pore volume. It is defined as the ratio of pore volume to bulk volume and expressed in volume percentage or volume fraction. It is mathematically expressed as

$$\phi = \frac{V_P}{V_B} x100 = \frac{V_B - V_G}{V_B} x100 \ldots\ldots\ldots\ldots\ldots\ldots \quad (3.1)$$

where, V_P is the pore volume of the rock, V_B is the bulk volume of the plug, V_G is the grain volume and ϕ is the porosity. V_B was measured using Archimedes principle through mercury immersion which measures the volume of mercury displaced when a sample is immersed.

To estimate porosity of the sample, the space occupied by water and free hydrocarbons needs to be accounted to get hydrocarbon and water free porosity. Karastathis, 2007, developed a technique for this at the IC^3 lab. About 6-8 grams of shale sample is kept in the oven for 12 hours at 100°C. After this, the sample is cooled in a desiccator for 20-30 minutes before recording its bulk volume. The sample is then thoroughly crushed in an enclosed vessel and allowed to settle. Powdered shale is then carefully recovered in low pressure pycnometer (LPP) cells, ensuring that the weight loss is not more than 0.6% before and after crushing. Sample is heated again at 100°C for at least 6 hours before being cooled and run inside the LPP machine. The machine works on the principle of Boyle's law. Helium is introduced in the cells at a low pressure of 20 psi. Pressure drop across the sample with and without the sample is used to measure grain volume and grain density of the sample. Obtained grain volume can be corrected for lost weight by the following expression

$$V_G^- = V_G + \frac{\Delta m}{\rho_G} \qquad (3.2)$$

where, V_G^- is the corrected grain volume and Δm is weight loss while crushing. Figure 11 shows images of crushing vessel and LPP machines.

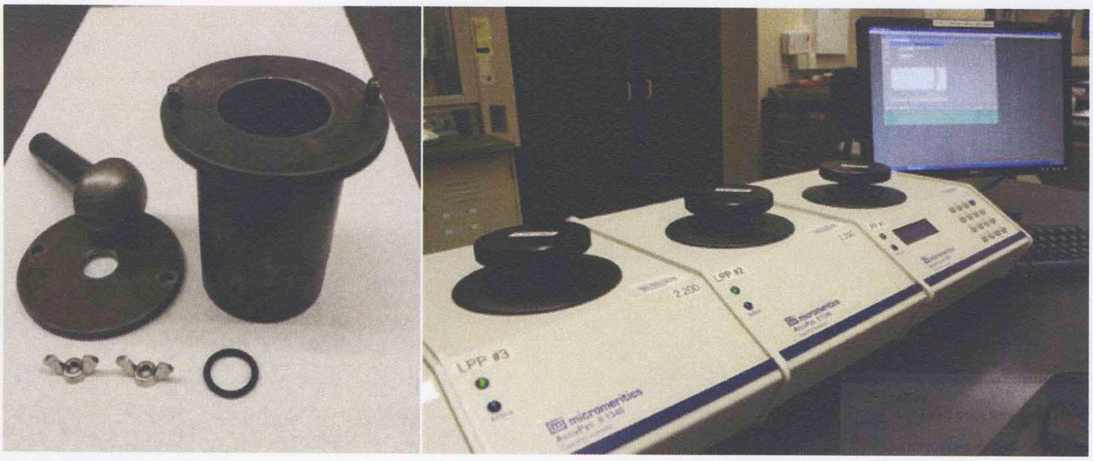

Figure 11: Equipment for shale porosity measurement. (Left) Crushing vessel for powdering shale. (Right) Micrometrics low pressure pycnometer for measurement of grain volume and grain density.

3.2 FTIR Mineralogy

Methods to quantitatively determine mineralogy include point counting, wet chemistry, X-Ray diffraction (XRD), Fourier Transform Infrared Spectroscopy (FTIR). Quantitative estimation of mineralogy in this study was done using transmission FTIR technique. It is a faster technique which enables its use even at the wellsite. Sixteen commonly found minerals in rocks can be resolved; these include: quartz, calcite, dolomite, aragonite, siderite, illite, kaolinite, smectite, chlorite, mixed clays, oligoclase feldspar, orthoclase feldspar, albite, pyrite, apatite, and anhydrite. It is based on absorption of mid-infrared energy (4000 to 400 cm^{-1}) by minerals. Covalent bonds in different minerals resonate at different frequencies over this range. When infrared radiation passes through a sample, some of it is absorbed and some is transmitted. FTIR measures the transmittance and the corresponding absorbance is calculated using the following equation

$$A = -\log_{10}\frac{T}{100} \qquad (3.3)$$

where, A is absorbance and T is transmittance in percent (Griffiths and De Haseth, 2007). Hence FTIR spectrum resolves the minerals in the sample with different absorption peaks identifying various mineral components (Sondergeld and Rai, 1993). Inversion of FTIR spectra provides mineral composition in weight percentage.

To perform FTIR, a small amount of sample is taken from the crushed LPP sample, in a pestle and mortar. It is further ground to a very fine powder using acetone as a cooling liquid while grinding. Next step is to remove the organic matter present in the shale. For this, the sample is put inside a low temperature plasma asher for 6 to 12 hours to oxidize and remove the organic matter. Sample is then kept inside loosely sealed vials and placed in the oven at 100°C for at least 2 hours to remove any moisture. To perform FTIR experiment, a small amount of powdered sample (5 mg) is mixed with potassium bromide (KBr) powder (300 mg) and pressed under 10 ton pressure to form a transparent disc. This disc is placed inside the sample holder and spectra is acquired.

One must ensure fine grinding of sample and removal or any moisture which may be present.

3.3 TOC Determination

Organic richness of shale is measured in terms of total organic carbon (TOC). Measurement of TOC by LECO C844 instrument requires 90 to 100 mg of finely powdered sample accurately weighed using a precise balance over a carbon free filter paper. Sample is then washed in dilute hydrochloric acid by pouring the acid over it. Acid washing dissolves inorganic carbon present in the sample. This is followed by washing the sample with water to remove any leftover acid. Sample is then dried in the oven at 100°C. This dried sample is wrapped inside the filter paper and kept in a crucible. Small amount of copper (~0.5 gram) and aluminum (~0.5 gram) are also added to the crucible before covering it with a cap. During the experiment, organic carbon in combusted in a pure stream of oxygen to form CO_2. Any carbon monoxide (CO) generated is also converted to CO_2 by the heated catalyst. Sulfur oxide produced during oxidation is removed from the stream by a filter. The gas stream then passes through a pair of Infrared Detector cells which detect short and long path lengths for measurement of high and low range signals coming from CO_2. Weight of CO_2 formed during oxidation is converted to TOC and expressed as weight percent based on dry sample weight. Figure 12 shows an image of sample weighed for TOC determination and its acid washing. It also shows the LECO C844 machine used for TOC measurement.

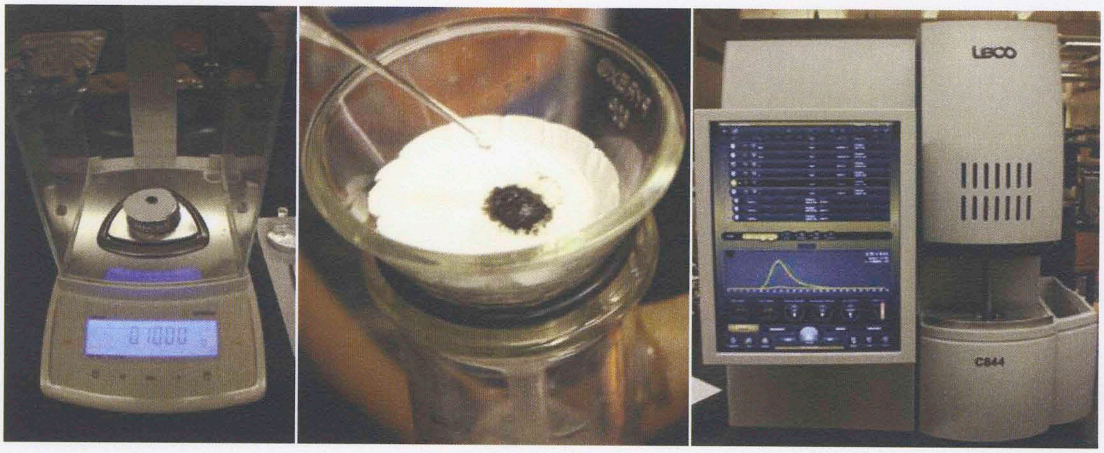

Figure 12: (Left) Finely powdered shale sample weighed to 100 mg for TOC determination. (Center) Acid washing of shale sample to dissolve inorganic carbon. Bubbles evolved during acid washing are clearly visible. (Right) LECO C844 machine for determination of TOC.

3.4 Rock Eval Pyrolysis

Theory behind pyrolysis was discussed in Chapter 2. The experimental procedure followed is explained in this section. A fresh shale sample is powdered and passed through a 40 mesh sieve. 60-100 mg of the sample is weighed into a glass vial and poured through the metal funnel housing into the metallic crucible. It is then capped and placed in the autosampler, a robotic system which picks up samples from the sample tray. A standard is measured along with a series of unknowns. 97 samples can be placed in autosampler tray. Sample is first heated to 300°C for 3 minutes. Free hydrocarbons are volatilized and detected by the FID detector and quantified as S_1 in mg of hydrocarbon per gram of rock. Temperature is then increased at 25°C/minute to 600°C. During this period, hydrocarbons are generated from cracking of kerogen in the rock and is called the generative potential of the rock. FID quantifies these hydrocarbons in mg of hydrocarbons per gram or rock (S_2). CO and CO_2 released is detected by IR cells.

CO_2 released between 300-400°C (S_3) is referred as organic CO_2 and expressed in mg of CO_2 per gram of rock.

Hydrogen index (HI) is determined as mg of hydrocarbons in S_2 per gram of TOC and oxygen index (OI) is the ratio of mg of CO_2 in S_3 per gram of TOC (Espitalie, 1977). These parameters could by approximately correlated with H/C ratio and O/C ratio on a Van Krevelen diagram. Hence a plot of HI versus OI could be interpreted in the same manner as a Van Krevelen diagram (Hunt, 1996). This kind of analysis can be highly erroneous at low TOC values. Pyrolysis still is a faster and simpler technique compared to elemental analysis on which Van Krevelen diagrams are based.

3.5 Vitrinite Reflectance Measurement

Vitrinite is one of the four macerals found in organic matter. Vitrinite reflectance ($\%R_o$) is used as an indicator of maturity or organic content. There are two methods to measure R_o, either by dissolving the inorganic content by hydrochloric acid and hydrofluoric acid and analyzing the leftover organic matter after drying and polishing it. This method does not help to understand the distribution of organic matter in the sample. The other method is to polish the sample which contains both organics and inorganics. To measure R_o, sample is studied under a reflecting microscope and the value reported as percent reflectance in oil (Dow, 1977).

3.6 Acoustic Velocity

Ultrasonic pulse transmission technique is used to measure compressional (V_P) and shear wave (S_1 and S_2) velocities (Screiber et al., 1973). 1 inch diameter core plugs were taken and polished to make the two sides parallel. A thin layer of honey is applied at the top and bottom of plug in order to have a good coupling for acoustic signals. The plug is enclosed in neoprene jacket and held between two transducers using hose clamps. The transducer stack consists of piezoelectric crystals (PZT-5A) having a resonant frequency of 1 MHz and 1 KHz. One of the crystals is in compressional mode and two are in orthogonally polarized shear mode. The samples are tested under different confining pressured from 250 to 5000 psi. Since no pore pressure is applied, so the effective pressure is the same as confining pressure. Waveforms are recorded at each pressure; wave arrivals are manually picked by the user.

3.7 Nanoindentation

Nanoindentation is a technique developed for getting mechanical properties of small quantity of substances. The technique was developed in the 1970's but was used mainly for design purposes by the ceramic, polymer, metal, electronics and medical industries. It uses a very small force and can measure the Young's modulus and indentation hardness of a sample. Continuous recording of loading and unloading enables to get these properties without imaging the residual impression (Oliver and Pharr, 2004). Indenters used are of known geometries and are usually made of diamond. Precise high resolution electronic instruments in the machine monitor loads and displacement of indenter inside the sample surface at nanometer scale (Hay and Pharr, 2000). Indentations can be carried out in a depth control mode or at a fixed load. When combined with SEM imaging, nanoindentation becomes a very powerful tool. Measurements at small scale allow for measuring properties of individual grains and organics comprising the rock. The Agilent G200 nanoindenter used for this study also allows to test samples at temperatures as high as 350^{0}C. We have studied the applicability of nanoindentation on sedimentary rocks including shales, sandstones and carbonates. This section describes the procedures followed for making measurements on shale samples studied.

3.7.1 Sample Preparation for Nanoindentation

Sample preparation is one of the most critical aspect for nanoindentation. Bad sample preparation affects results adversely. The surface has to be flat and smooth. Smoothness of surface is important because contact area is calculated on the basis on contact depth and area function. An undulated surface adversely affects these calculations. A rough surface will also result in large standard deviation in the results obtained (Kumar, 2012a). The degree of smoothness also depends on the magnitude of displacements and the tolerance for uncertainty in contact area. There is a size limitation for samples used for nanoindentation. The selected sample should not be more than 8 mm in thickness and if the sample is in the form of a disc, its diameter should be no more than 1 inch. Broken pieces from shales can also be used as long as they are within the specified size range or embedded in a host medium. The selected sample is first polished progressively on a glass plate using sand papers from 60 to 3000 grit size. At the end of dry mechanical polishing, the maximum thickness difference between any two points in the sample should not be more than 0.01 mm.

Sample with high quartz and carbonate content can be difficult to polish to the specified threshold. Also if sample surface is large, then ensuring parallel top and bottom surfaces may be difficult. In such cases a precision polisher could be used as shown in Figure 13. The sample is mounted to an arm which can be lowered to the circular disc. The arm can rotate as well as move to and fro over the disc. The disc can also rotate at specified rotations per minute. A variety of specially designed abrasive papers from course to fine could be attached to the disc. Water is continuously supplied through a nozzle to lubricate the system during polishing. Continuous motion of sample and disc produces nearly parallel surfaces of high quality.

Figure 13: Allied Multiprep polisher. This technique delivers smooth and parallel sample surfaces due to continuous motion of the sample and disk and precise alignment of motion system.

Mechanical polishing is followed by broad beam argon ion milling to further reduce surface roughness. We have used a Fischione dual beam Argon ion milling device (Model 1060). Samples of diameter up to 1 inch can be easily milled. Duration of milling can be decided based on the top surface area of the sample and its composition. Samples rich in quartz and carbonates usually require longer milling times. During this process sample is kept under vacuum and ionized argon gas is accelerated and impinged on sample surface at angles almost parallel to sample surface. Two ion beams are focused on the sample surface. Power and focus of the beams can be adjusted by the user based on the sample. Excessive power can also result in damage to the sample surface due to heating. During ion milling, the sample can be continuously rotated for uniform exposure on all sides. This removes most of the surface imperfections left behind after mechanical polishing. Achieving a perfectly smooth surface is difficult, but a combination of dry polishing, wet polishing and ion milling can help reduce errors in nanoindentation results due to surface roughness. Figure 14 shows an image of Fischione dual beam argon mill. Figure 15 show survey scans of an ion-milled sample and un-ion-milled sample, where the roughness scale in the ion-milled sample varies from 0 to 1546 nm while that in the un-ion milled sample varies from 0 to 3243 nm. Difference in roughness of these two samples is shown in X and Y profiles along the center of the sample (Figure 16) which indicates that topography in the ion milled sample varies from 500 to 1500 nm. In the un-ion milled sample topography variation was observed between 100 to 2000 nm which indicates this un-ion milled sample is much rougher. Sample roughness affects the measurement of Young's modulus. This is shown in Figures 17 and 18 where histograms of Young's modulus on ion-milled and un-ion-milled shale sample are presented. Larger scatter in Young's modulus can be observed for un-ion milled sample.

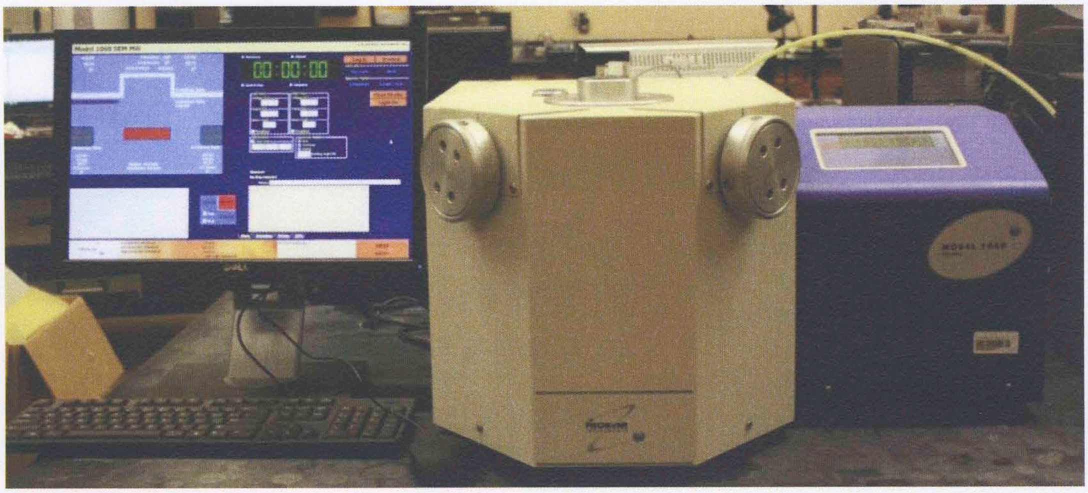

Figure 14: Fischione 1060 Mill.

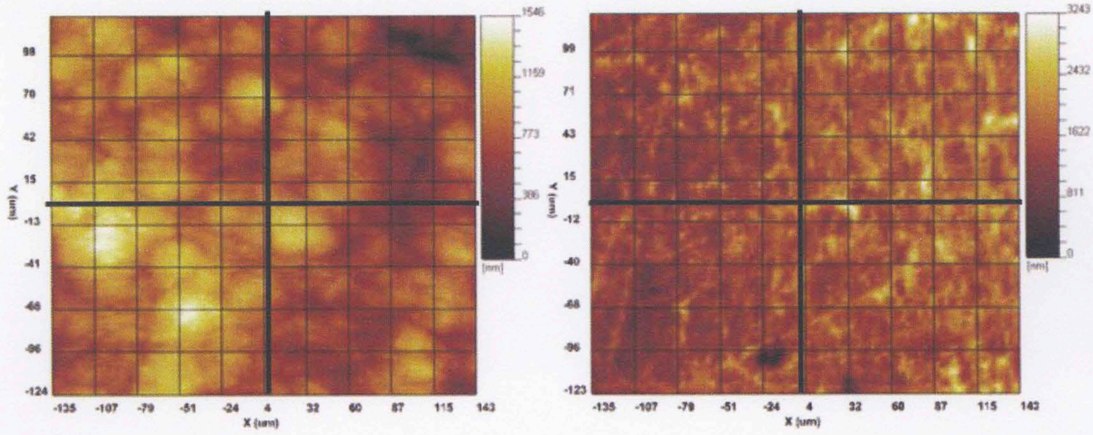

Figure 15: Survey scanning topography profiles of two shale samples, ion-milled (left), un-ion-milled (right).

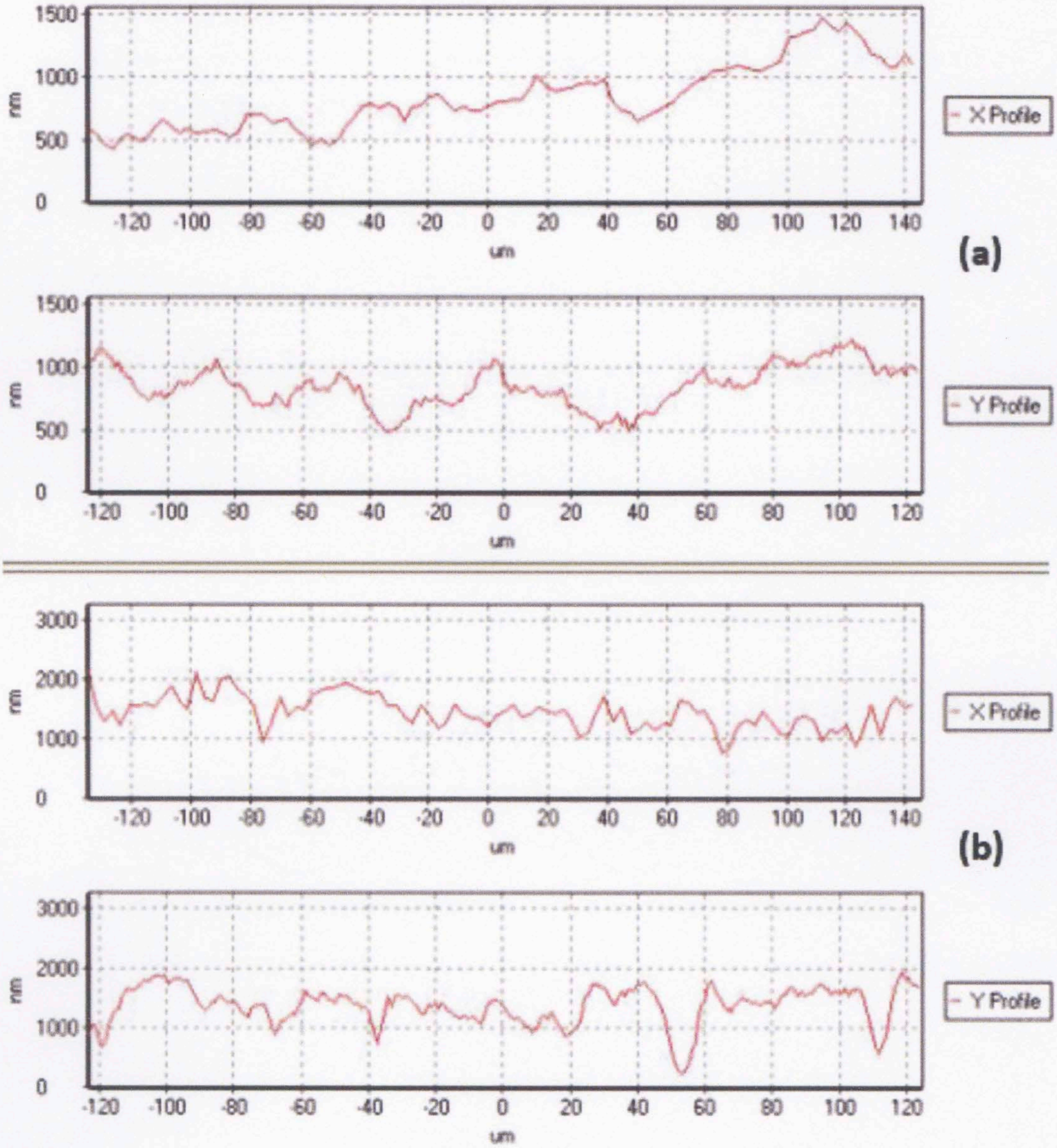

Figure 16: X and Y profiles along bold black lines in Figure 15, for (a) ion-milled, and (b) un-ion-milled shale samples. More roughness is observed in the un-ion milled surface. Notice the variation in sample topography in X and Y directions for both ion milled and un-ion milled sample. Note scales are different between (a) and (b).

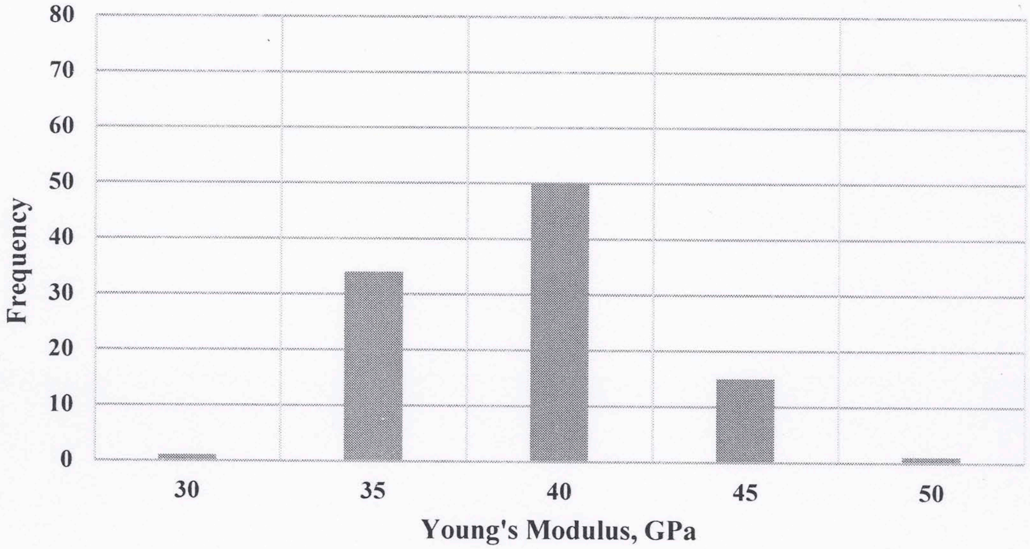

Figure 17: Histogram of Young's modulus measured on a Wolfcamp shale sample without ion milling. Average Young's modulus is 39 GPa and the standard deviation is 3.4 GPa.

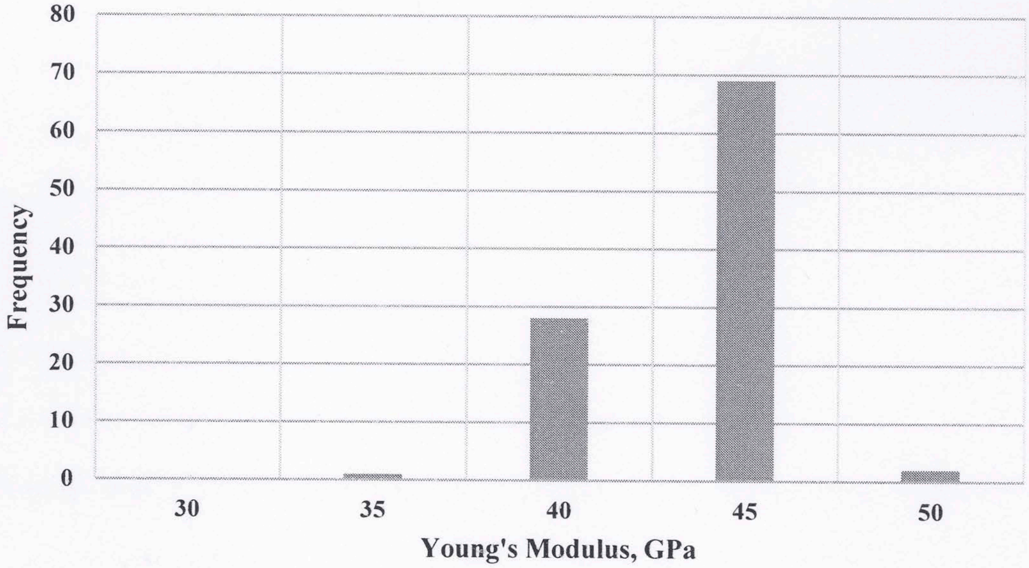

Figure 18: Histogram of Young's modulus measured on a Wolfcamp shale sample with ion milling. Average Young's modulus is 43.5 GPa and standard deviation is 2.1 GPa.

3.7.2 Theory, Procedure and Calculations

The objective of nanoindentation tests is to determine the Young's modulus (E) and hardness (H) of the specimen material. Conventionally, Young's modulus is obtained from stress versus strain curves as the slope of curve within the elastic limit.

$$E = \frac{\Delta stress}{\Delta strain} \quad (3.4)$$

It describes the resistance offered by a material to withstand deformation under the effect of tensile or compressive forces. Conventional measurement techniques for hardness rely on the measurement of the size of residual impression created after releasing indenter load. Hardness is a measure of the resistance of a material to permanent deformation under the influence of a force.

Such tests use higher loads (more than 10000 N) require samples of larger size (few centimeters) which may not always be available. Nanoindentation technique was developed to measure Young's modulus and hardness on very small samples (few millimeters) and thin films, and can be performed at loads as low as 1 nN. Size of residual impression in a nanoindentation test is of the order of microns which cannot be accurately imaged. Hence the system relies on continuous monitoring of load and displacement of indenter inside the specimen. Using an indenter of known geometry allows accurate estimate of indentation size to calculate Young's modulus and hardness.

Nanoindentation Theory

A single nanoindentation test comprises of a loading and unloading cycle during which load on sample and depth of penetration of the indenter are measured as load is applied from zero to maximum specified load. Then the load is reduced back to zero which constitutes the unloading cycle. Figure 19 shows some commonly observed load (P) versus displacement (h) curves for 6 different kinds of materials during one loading-unloading cycle. The shape of these curves provide information about phase transformations, cracking and delamination of films (Fischer-Cripps, 2011). Shales have load-displacement curves resembling that in sapphire and fused silica (Figure 19 b&e).

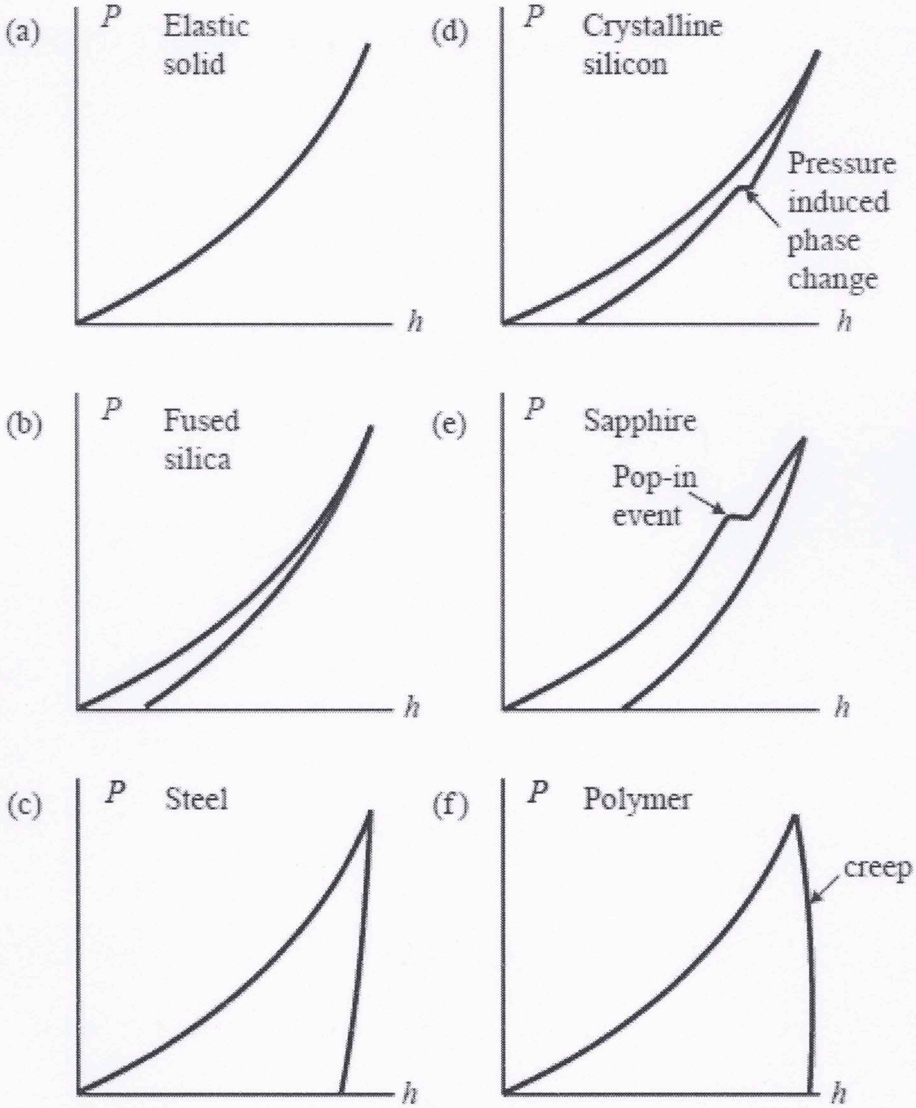

Figure 19: Load-displacement curves for 6 different materials showing distinct behaviors encountered in each material: (a) elastic solid, (b) brittle solid, (c) ductile solid, (d) crystalline solid, (e) brittle solid with cracking while loading, and (f) polymer exhibiting creep (Fischer-Cripps, 2011).

Resistance to deformation by an elastic body is defined as stiffness. Objects with higher Young's modulus are stiffer and have a steep unloading curve (Shukla et al., 2013).

Indenter Types

Indenter tips are usually manufactured from diamond due to its high hardness and elastic modulus. Such properties eliminate the need to factor the displacements in indenter itself during calculations. Indenters made of sapphire, tungsten or hardened steel lack stiffness and require corresponding corrections to be made when using such indenters.

Calculation of E and H rely on indenter geometry which makes it necessary to have a known simple geometry. Four kind of indenter geometries are commonly used for nanoindentation testing: (a) Pyramidal or Berkovich, (b) Spherical, (c) Cube corner, and (d) Conical. Each tip has its own advantage and each one is selected based on the objective to be achieved. Berkovich indenter is most frequently used for nanoindentation testing and was used in this study as well.

Indentation Procedure

Nanoindentation testing involves application of a fixed force on an indenter which presses against the sample thereby creating an indentation mark on the sample surface. Figure 20 presents the schematic of nanoindenter. A software controlled system sets up a load (1nN to 500mN) to be applied by the force actuator on the indenter shaft. This load is applied at a fixed rate until the peak load is reached. The displacement of the indenter shaft is monitored using a capacitive displacement sensor. A microscope aids in site selection. Indentation can also be done in the form of 2D arrays be specifying the number of indentations and spacing between indentations in X and Y directions.

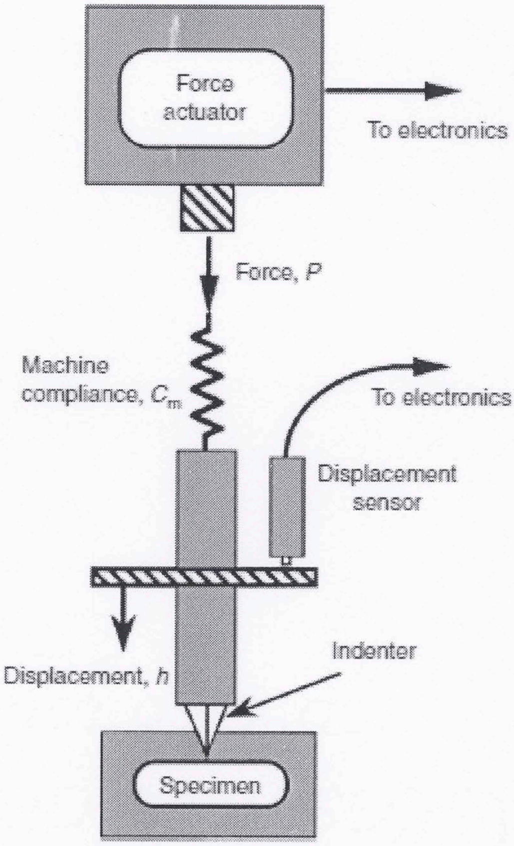

Figure 20: Schematic of nanoindenter showing the magnet and coil actuator assembly and capacitive displacement measurement assembly (Hay and Pharr 2000).

Loading and unloading of a sample during nanoindentation generally leaves a residual mark on the sample. This confirms that some deformation is plastic but there is also some elastic recovery. It is in this elastic zone that the unloading curve follows a straight line and using the slope of the curve, properties like E and H can be calculated. For a purely elastic deformation the depth of indentation should be limited to less than 10 nm. Figure 21 shows an image of indentation on fused silica demonstrating the scale of a single indentation impression formed using a force of 500mN.

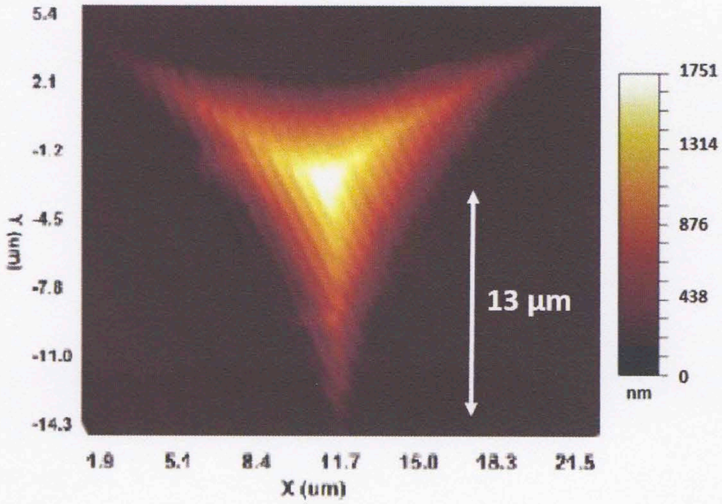

Figure 21: Survey scanning topography image of single indentation on fused silica generated by nanoindenter. Radius of impression is 13 microns.

Calculation of Young's Modulus and Hardness

A set of calculations need to be made to arrive at the final values of E and H. This procedure was presented by Oliver and Pharr, (2004) and discussed as follows:

1. Generating load-displacement data for the loading-unloading cycle. Four quantities must be established from this as shown in Figure 22: P_{max} (maximum load), h_{max} (maximum displacement), contact stiffness, $S = {}^{dP}/_{dh}$ (slope of upper portion of unloading curve), and h_f, final depth of indentation.
2. The upper 25% of the unloading curve can be approximated by the power law relation

   $P = \alpha(h - h_f)^m$ .... (3.5)

   where, P is the load, h is the total displacement with respect to initial undeformed surface, α and m are power law fitting constants. Power law exponent, m, varies in the range $1.2 \le m \le 1.6$.

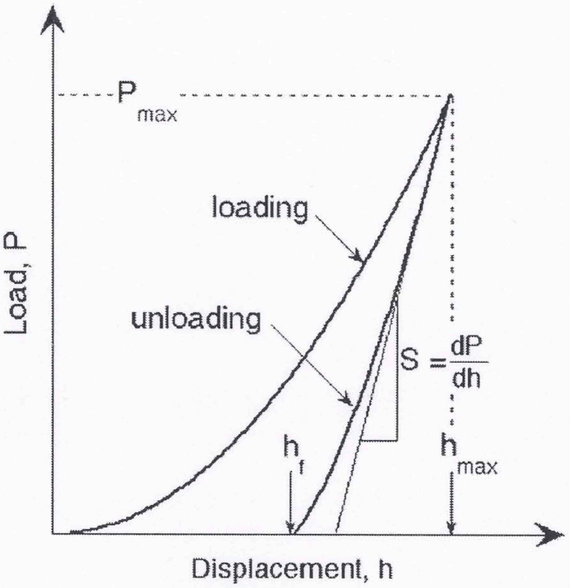

Figure 22: Schematic showing load-displacement data and important parameters (Oliver and Pharr, 2004).

3. The calculation of E and H for indentations carried out by a Berkovich indenter is modeled using conical indenters the half included angle, ϕ = 70.3 that gives same depth-area relationship. A certain amount of surface sink-in is assumed and any pile-up around the indentation is ignored which some elastic-plastic materials show. Figure 23 shows elevation view of an indentation showing sink-in (h_s), which is calculated as

   $h_s = \epsilon \frac{P_{max}}{S}$... (3.6)

   where, ϵ is constant for each indenter geometry but ϵ = 0.75 is used for most analysis.

   Hence contact depth between the indenter and sample, can be expressed using equation 3.6 as

   $h_c = h_{max} - \epsilon \frac{P_{max}}{S}$.. (3.7)

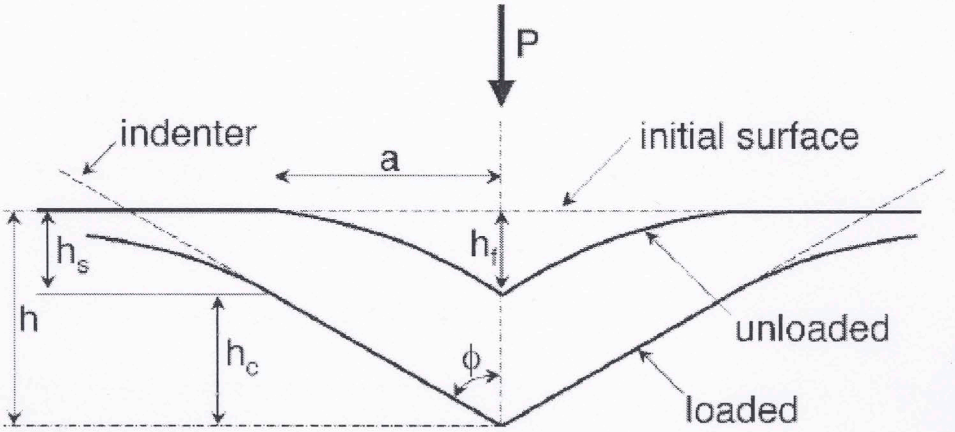

Figure 23: Elevation view of an indentation impression showing sink-in and parameters describing contact geometry (Oliver and Pharr, 2004).

4. Contact stiffness can be expressed analytically as the differential of equation (3.8) at maximum depth of penetration h_{max} as given by Kumar (2012a) as

   $$S = {}^{dP}/_{dh} = \alpha m(h - h_f)^{m-1} \quad \text{.......} (3.8)$$

5. The area of impression and subsequent calculation of E and H depend on the indenter area function calibrations. Once calibrated, measurement of contact depth, h_c, tells about indentation area ,A, since

   $$A = f(h_c) \quad \text{.......} (3.9)$$

6. Hardness can be calculated at maximum load by

   $$H = \frac{P_{max}}{A} \quad \text{.......} (3.10)$$

   Since hardness is calculated at maximum contact area under load, it may differ from conventional hardness measurements based on residual impression area. This issue may be more pronounced if there is significant elastic recovery during unloading.

7. Elastic modulus is related to contact area and unloading stiffness by the relation

$$S = \beta \frac{2}{\sqrt{\pi}} E^* \sqrt{A} \quad \text{(3.11)}$$

where, E^* is effective elastic modulus which accounts for elastic displacements in the sample and indenter, and β is a parameter depending on indenter geometry. β =1.034 for a Berkovich indenter.

Young's modulus of the sample can be calculated using the relation

$$\frac{1}{E^*} = \frac{1-\upsilon_i^2}{E_i} + \frac{1-\upsilon^2}{E} \quad \text{(3.12)}$$

where, υ_i and E_i are Poisson's ratio and Young's modulus of the indenter, and υ and E are Poisson's ratio and Young's modulus of the sample. For diamond indenter, υ = 0.07, Ei = 1141 GPa. For calculation of E, the Poisson's ratio of sample needs to be assumed. Figure 24 shows the dependence of calculated Young's modulus on Poisson's ratio for a shale sample at room temperature. It seems clear that for ±0.1 change in Poisson's ratio there is roughly 6% change in Young's modulus.

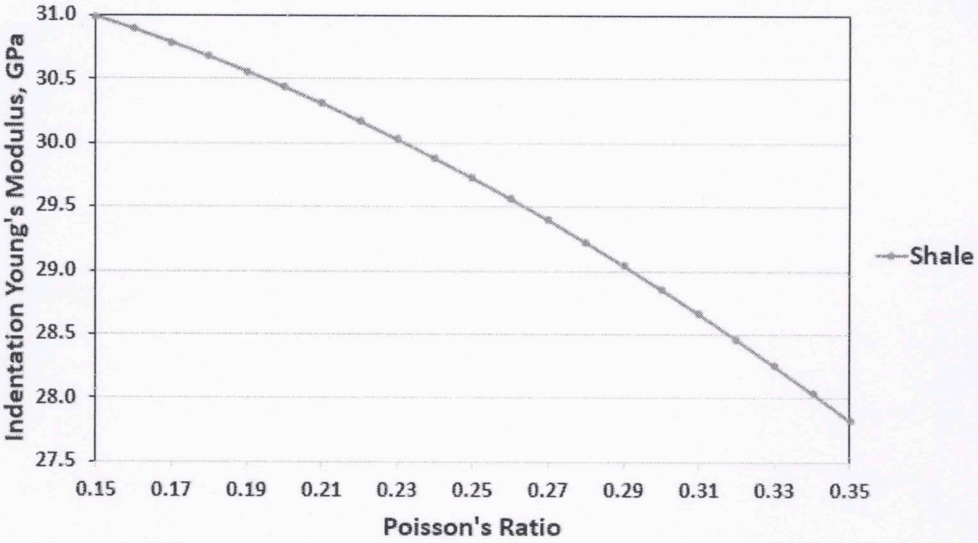

Figure 24: Young's modulus depends on Poisson's ratio weakly. Approximately 6% change in E with ±0.1 change in υ is observed.

3.7.3 Equipment Description

Agilent G200 Nanoindenter was used for nanoindentation experiments during this study. Figure 25 shows the image of a G200 nanoindenter. Due to extreme sensitivity of the system, environmental isolation becomes necessary. This is provided with a combination of minus k vibration isolation table and thermal/sound insulated vibration isolation cabinet. The machine is equipped with an optical microscope with two lenses of different magnification (10X and 40X). A computer controlled software (Nano Suite) helps to plan the location of indentations. Table 4 summarizes some important specifications for the G200 nanoindenter.

Table 4: Important specifications for G200 Nanoindenter (G200 user manual).

Standard Indentation Head Assembly	
Displacement resolution	<0.01 nm
Maximum indentation depth	>500 μm
Load application	Coil/Magnet assembly
Displacement measurement	Capacitance gauge
Loading Capability	
Maximum load	500 mN
Load resolution	50 nN
Indentation Placement	
Usable sample area	100 x 100 mm
Positional accuracy	1 μm
Microscope	
Video screen	25 X
Objective	10 X and 40X

Motion system guides the movement of stage on which the sample is mounted. Positioning tables are X/Y directional piezo stages and are used to position the sample under the microscope or indenter. Force during nanoindentation is generated by passing current through a coil wrapped around a circular magnet. Indenter displacement inside the sample is sensed by measuring voltage change due to movement of indenter shaft between two fixed metallic plates.

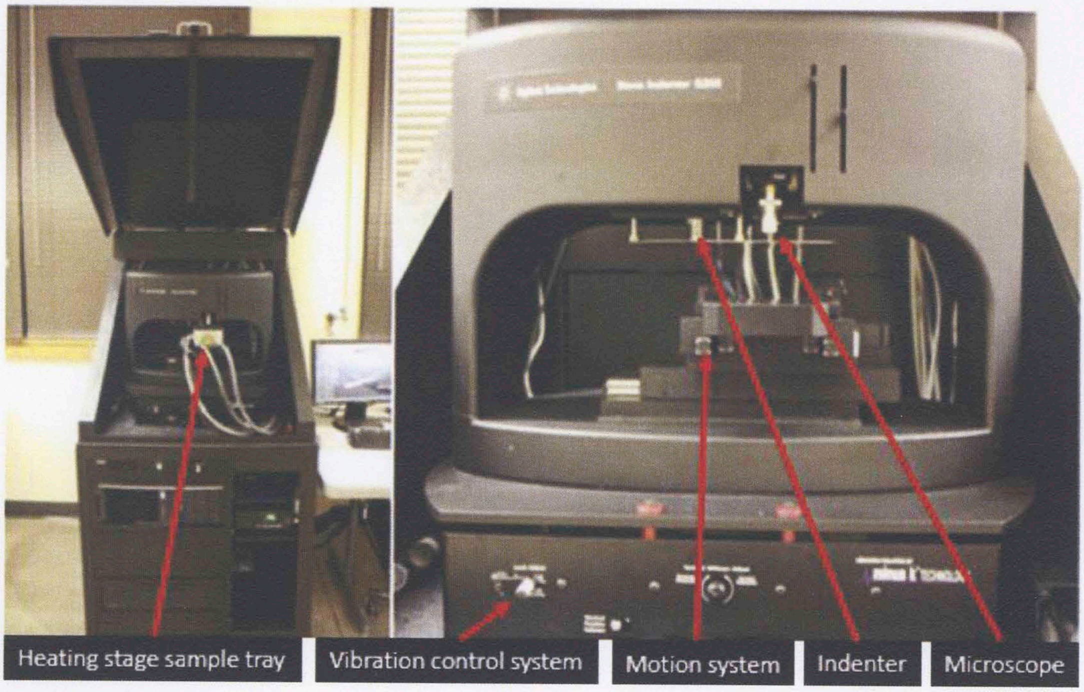

Figure 25: (Left) Agilent G200 nanoindenter showing heating stage tray, temperature control system and coolant and gas lines. (Right) Anti-vibration assembly showing microscope, indenter and head shielding plate. Vibration control stage dampens and vibration in the cabinet.

3.7.4 Sample Mounting for Nanoindentation

Procedure for mounting samples for room temperature and high temperature is different. This section discussed both the procedures.

Following procedure is followed to mount samples for testing at room temperature

- Sample disk is heated to about 160°C on a heating plate (Figure 26) for about 5 minutes
- A small amount of crystal bond is applied to sample disk and the polished sample is mounted onto it and allowed to cool to room temperature
- Sample is inserted into one of the holes in G200 sample tray (Figure 26) and the tray is loaded on top of the motion system for nanoindentation.
- A pre-mounted fused silica crystal (factory installed) is used for focusing the microscope to a specified height. Sample is also adjusted to the same height using thumb screws on the G200 sample tray.

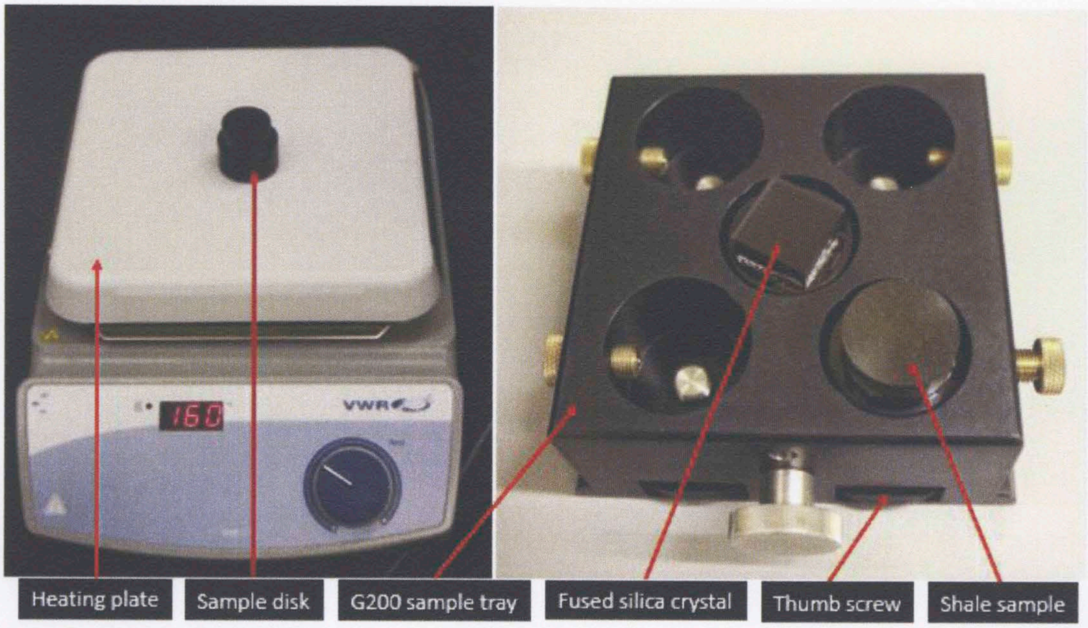

Figure 26: (Left) Heating plate set to 160°C for mounting the sample. (Right) G200 sample tray with standard fused silica crystal at the center and shale sample at one of the corner slots. Height of the sample can be adjusted using thumb screws.

Procedure for testing at elevated temperatures is different from room temperature testing. A specially designed hot stage tray (Figure 27) is used for this purpose. Sample is mounted on a different disk which can be easily attached to heating stage using a set of screws. A special polymer (commercial name: POLY 2000) is used for mounting samples. Hot stage tray can be used to test samples at temperatures as high as 350°C which are achieved with the help of two heating elements. Coolant lines (Figure 27) are installed on the stage to avoid unnecessary heating of adjoining equipment. K200 (commercial name) is used as a coolant for use up to 350°C. Coolant is circulated with the help of a pump. A metallic heat shield is installed to dissipate any heat going to indenter shaft and capacitive plates. Heating stage also has a thermocouple to measure temperature while a display panel is used to set the temperature. Following steps outline the procedure used for mounting samples for high temperature testing

- POLY 2000 is well shaken to mix all contents
- A small amount of polymer is taken using a spatula an evenly spread on sample disk
- Polished sample with rough bottom surface is then mounted on the disk and allowed to settle for at least 8 hours at room temperature.
- Sample disk is then attached to heating stage using screws. Lubricant is applied to screw threads before this.
- Heating stage does not have thumb screws, so the height of the sample is adjusted using side rails which are adjusted in accordance to G200 standard fused silica crystal during installation.
- Hot stage tray is then loaded on top of the motion system for nanoindentation.

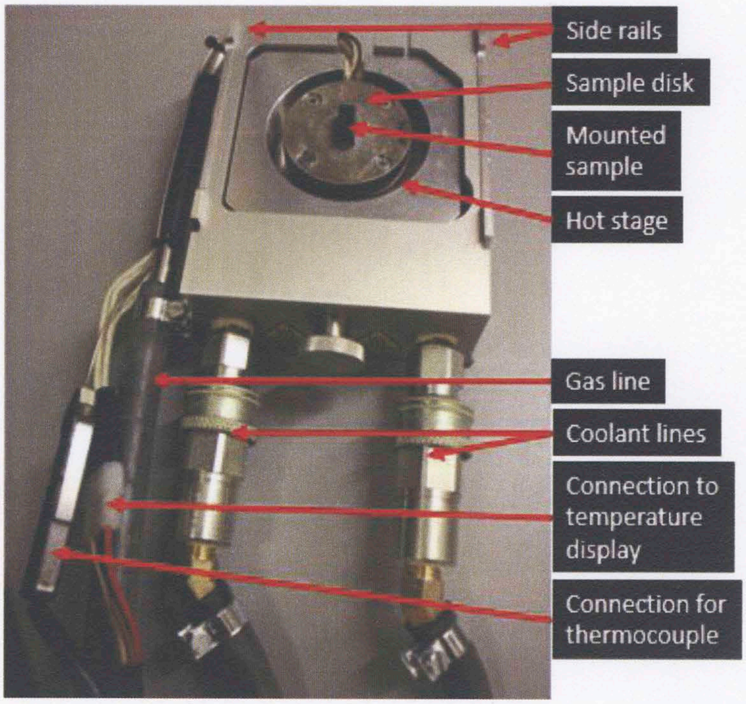

Figure 27: Hot stage tray used for testing at elevated temperatures. Tray is equipped with heating system, coolant lines, gas line and thermocouple.

3.7.5 Nanoindentation Procedure

Once the sample is mounted and placed inside the sample tray, its height needs to be adjusted in accordance with the reference factory mounted fused silica sample height. This is done in order to ensure that sample is within the reach of the indenter, which has a very limited vertical movement range. Microscope is also initialized to correct focus using fused silica crystal as a reference. Following this, the stage is moved so that sample comes under the microscope. If there is a particular spot which needs to be indented then it is located using the microscope. Otherwise a random smooth area is selected for nanoindentation.

Indentations can be performed in many ways and the correct method has to be selected based on the objective. Some of the commonly used methods are

- XP methods: This method is used for indentations at room temperature. It can be performed either under depth control mode (we have used 500 nm) in which a threshold depth of investigation can be specified. It is particularly useful when testing the properties of thin films or organics. The other way is to perform indentations under load control mode (we have used 300-500 mN) in which a threshold maximum load limit is provided. This method is used for testing macro properties such as for rock matrix or metal surfaces.
- Hot Stage methods: This method is used for testing at elevated temperatures and is used under load control mode.
- Survey Scanning: This method is used when the surface of a sample has to be scanned for is smoothness or to generate a map for depth of indentations after running nanoindentation.

XP and Hot Stage methods also require specification of the "tip" to be used for performing all calculations. Tips are defined during calibration stage for temperature intervals of 25^{o}C. Frame stiffness changes as the temperature changes, therefore the correct tip needs to be selected before testing at any temperature. Frame stiffness calibrations are discussed later.

Once the correct method and tip are selected, four arrays of 5x5 indentations are made. Spacing between each indentation is suitably selected (10-20 times the maximum depth of penetration) so that there is no interference between individual indentations and arrays. Figure 28 shows a SEM back scatter electron (BSE) topography image of four arrays of indentation on a shale sample. Figure 29 and 30 show plots of force versus time and force versus displacement. Increase of force represent loading section while decrease of force represent unloading section. The holding section represents displacement at constant load which is used for creep investigation. Resulting Young's moduli and hardnesses from 100 indentations tests are averaged to obtain the final value for a sample. Figure 31 shows 100 load-displacement curves generated for one sample at a peak load of 500 mN.

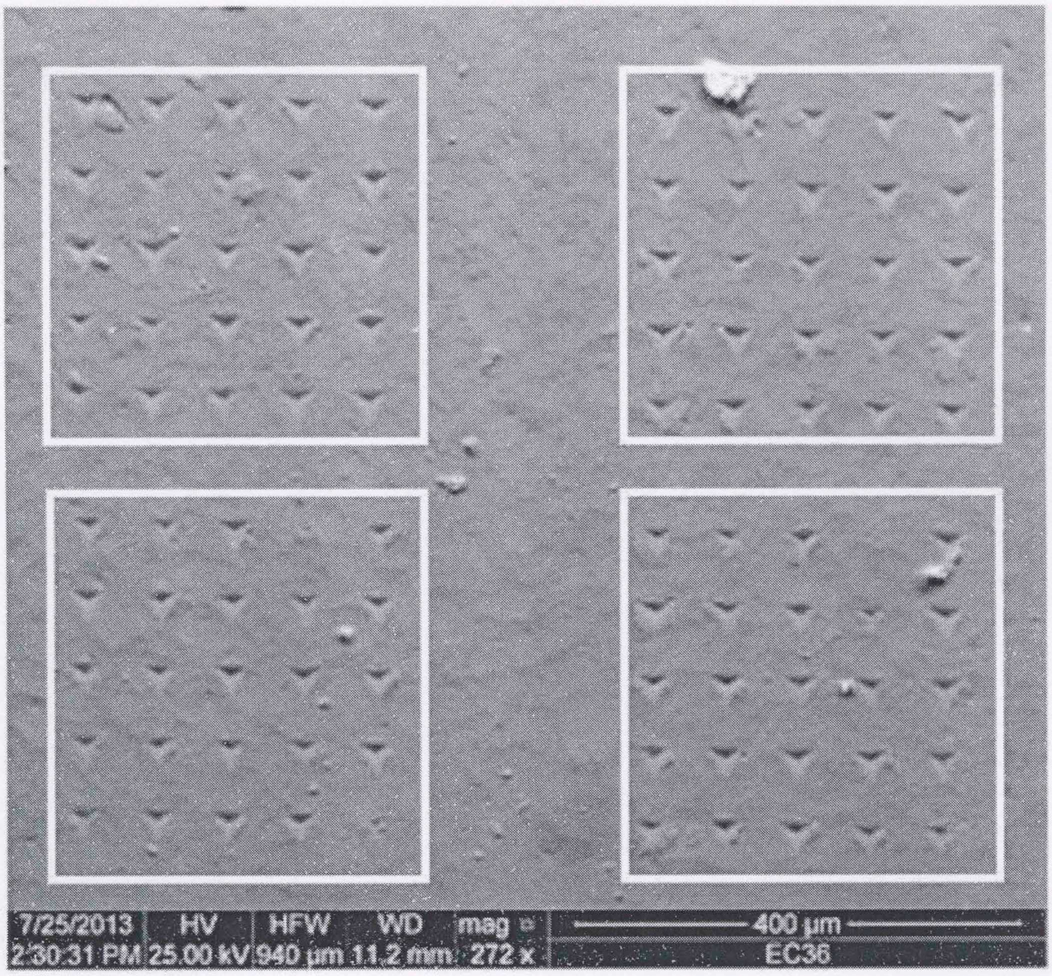

Figure 28: BSE topography image of four arrays of 5x5 indentations on shale. Single array of indentations is 350x350 µm and spacing between individual indentations is 65 µm.

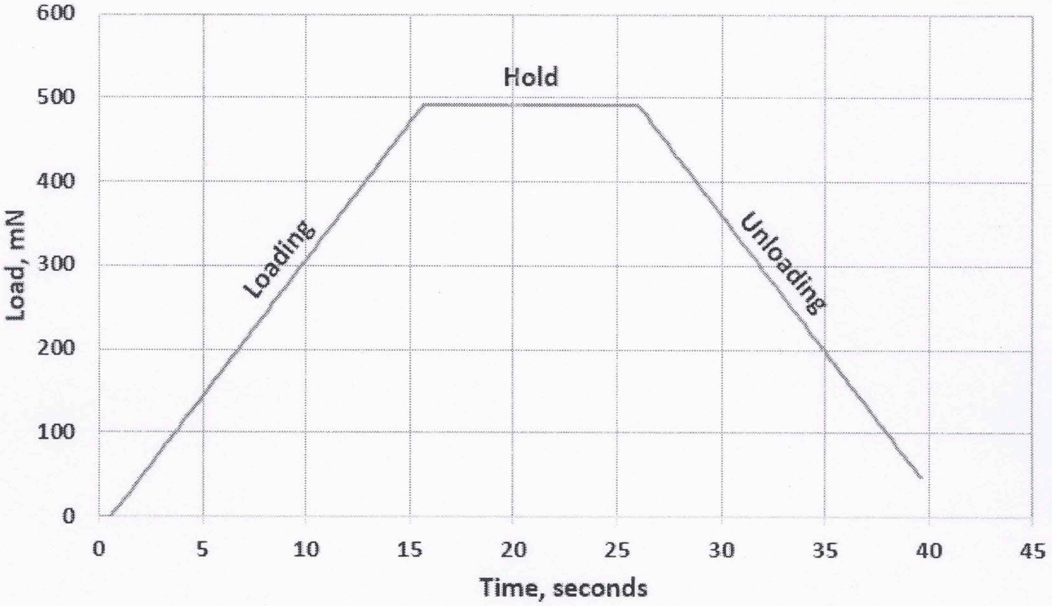

Figure 29: Variation of load versus time during a single nanoindentation test on a shale sample. Peak load threshold was set to 500 mN.

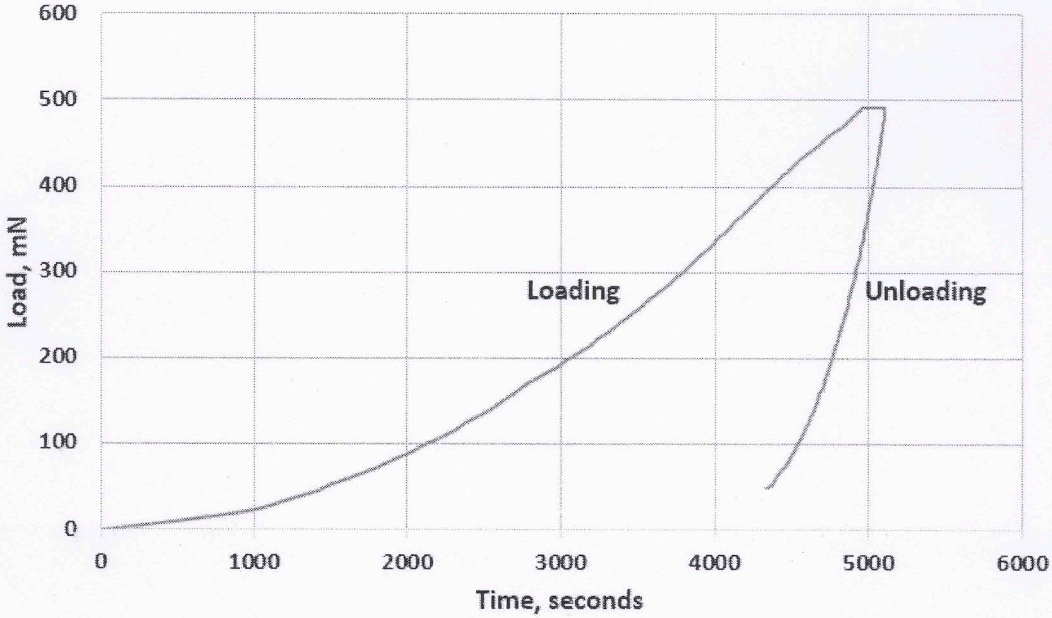

Figure 30: Load-displacement curve plot for a Wolfcamp shale sample under depth control mode of 500 mN.

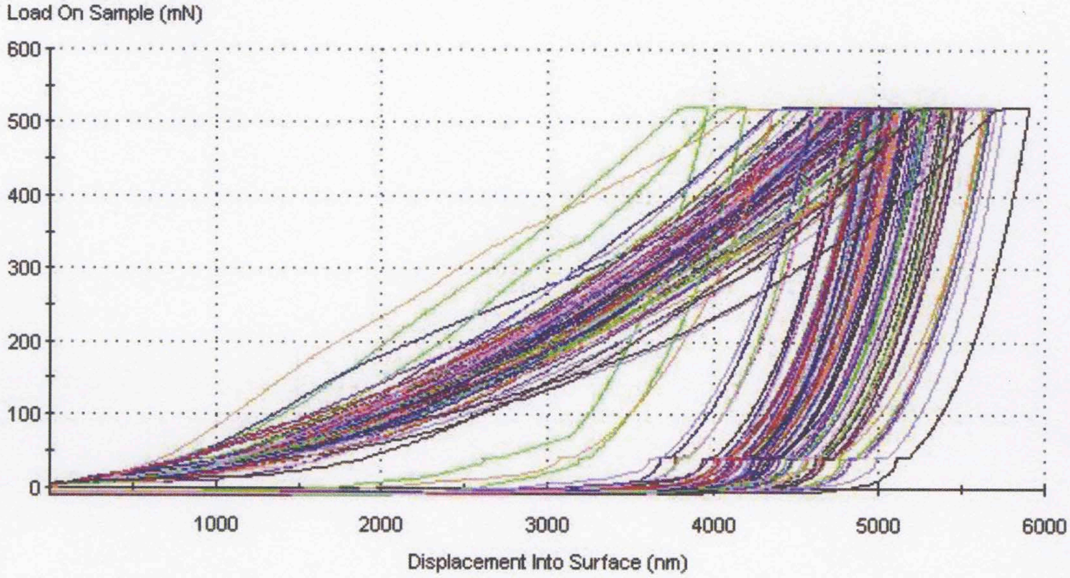

Figure 31: 100 load-displacement curves for tests on Wolfcamp shale. 500 mN was used as peak load for each indentation.

3.7.6 Nanoindentation Calibrations

Reliable results from nanoindentation are dependent of instrument calibrations. Measurements on fused silica are often a quick check of the accuracy of results. In spite of this several calibrations are necessary to minimize for errors resulting from machine compliance or frame stiffness and area function of indenter. All calibrations are performed using polished fused silica specimen.

Frame stiffness calibration: has to be performed for G200 sample tray as well as the Hot Stage sample tray due to differences in machine compliance for the two trays. Temperature also has an effect on frame stiffness of Hot Stage sample tray. Hence frame stiffness has to be determined over a range of temperatures to be used, by testing on a fused silica crystal. Indentations are done at decreasing depth of investigation (displacement) of the indenter inside the fused silica crystal. Stiffness squared over load (S^2/P) is plotted versus displacement and the shape of this curve helps determine frame stiffness. The logic of looking at S^2/P versus displacement for calibration purposes stems from the fact that for pyrex (now Borofloat) and fused silica, the S^2/P is constant with depth. There is a known acceptable range of S^2/P and it should be constant for these two materials. If the data trends up or down, a frame stiffness correction is needed. Once the data is flat with increasing depth then it tells that frame stiffness is correct. Data less than 500 nm depth of penetration can be ignored if it does not fall along the flat trend. This is followed by checking the plot of Young's modulus versus displacement. When frame stiffness is correct, the value of Young's modulus should be constant with respect to displacement (see Figure 32). If this is not the case then it tells that area function of the indenter needs to be adjusted.

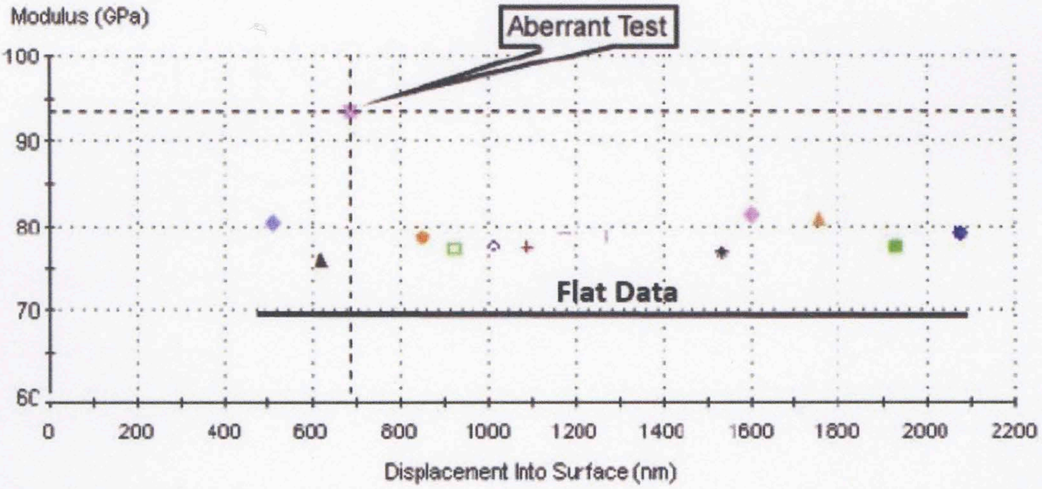

Figure 32: Plot of stiffness squared over load versus displacement into surface used for frame stiffness calibration. These tests are done for both sample trays and at multiple temperatures. A flat line indicates correct frame stiffness.

- **Area function calibration:** continuous use of an indenter for a period of time could result in slight changes in its shape. Since the calculation of Young's modulus and hardness depend on displacement and area of indenter, therefore a wrong indenter geometry could result in erroneous results. Indenter area function, A = f(d), is a functional description of the geometry of the part of the indenter that is designed to be in contact with test material. The ideal function for a Berkovich tip is $A = 24.56d^2$. The purpose of indenter area function calibration is to determine the best fit to the experimental data. Hence the fitted form for the indenter is expressed in the form of a polynomial as

$$A = m_o d^2 + m_1 d + m_2 d^{\frac{1}{2}} + m_3 d^{\frac{1}{4}} + m_4 d^{\frac{1}{8}} + \cdots \ldots\ldots\ldots\ldots\ldots\ldots (3.13)$$

An algorithm in the Nano Suite software is used to calculate the values of m_o, m_1, m_2.... At least 16 indentation need to be performed for this. The first indentation is at maximum load (300-500 mN generally) and subsequent indentations are at loads depreciating by a factor of 0.85 from the load at previous indentation. Once area function is calibrated, the plot of S^2/P versus displacement and Young's modulus versus displacement must be a flat horizontal line.

3.7.7 Sources of Errors

Measurement of mechanical properties at small scales are affected by slightest changes in parameters which can lead to errors. These errors could be due to environmental changes or incorrect depth measurements or non-ideal indenter shape. Pile-up (material piles up adjacent to the indenter; true contact depth becomes greater than theoretically predicted) and sink-in (material sinks-in close to the indenter; true contact depth is less than predicted theoretically) of sample surface as a result of indentation can also result in serious errors. Some methods were developed to minimize these errors.

Thermal Drift

Thermal drift results from temperature changes in the surrounding environment. It depends on the thermal equilibrium inside the cabinet and is generally lower when tests begin one hour after closing the cabinet. Thermal drift could affect nanoindentation in two ways. It could be during an indentation experiment when small thermal displacements could affect calculations. To account for this the rate of change of depth is measured at a constant load towards the end of the experiment. The thermal drift rate thus computed is used to adjust the depth readings throughout the test (Fischer-Cripps, 2011). Thermal drift may also affect creep in the specimen when the load is held constant during plastic flow as indenter sinks into the specimen. Thermal drift corrections have to be made for each indentation. Hay and Pharr, (2000), have discussed the effect of thermal corrections on load-displacement curves (Figure 33). The figure shows that thermal drift correction results in lower indention depth, thus increasing the resultant Young's modulus.

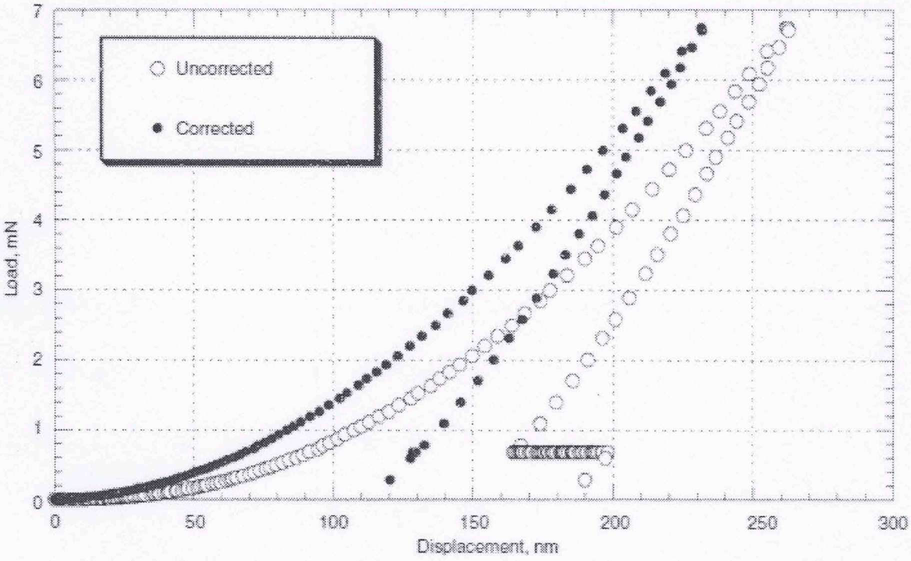

Figure 33: Load-displacement data for fused silica showing effect of thermal drift corrections (Hay and Pharr, 2000).

Environmental Corrections

Small changes in ambient temperature affect nanoindentation results due to dilation or contraction in the specimen, indenter or machine parts. To account for such errors a near constant temperature (±1°C) must be maintained close to the set-up. Software also accounts for a threshold thermal drift before which testing cannot begin. This value is usually taken to be 0.05 nm/sec.

Mechanical vibrations of the test set-up affect the depth sensing resolution of the indenter. A soundproof housing and anti-vibration table help minimize such errors.

Sample roughness can result in severe errors, especially in sample in which the depth of investigation is less (organic and thin films). This error can be minimized by careful polishing of the sample to achieve a smooth top surface and near parallel top and bottom surfaces.

Careful instrument calibrations for area function and frame stiffness are very important to get reliable test results.

3.7.8 Nanoindentation on Standard Specimens

A number of standard samples including fused silica and pyrex, minerals namely quartz, calcite, biotite etc., and metals were tested before large scale testing on shales and other rocks. Kumar (2012a) has discussed some of results in his thesis. Resulting Young's modulus values from these tests were compared to standard values present for each of these substances in the literature (see Table 5). The values from literature were taken from papers and books by various researchers including Simmons and Wang (1971); Mavko et al., (2003); Agilent Technologies, (2009) and www.engineeringtoolbox.com.

Table 5: Comparison of measured nanoindentation Young's modulus with published values based on this study and results by Kumar, (2012a).

Materials	Measured (GPa)	Literature (GPa)	Source
Fused Silica	73±0.2	74	Agilent Technologies (2009)
Pyrex	65±0.6	64	Agilent Technologies (2009)
Quartz	99±1	90-100	Simmons and Wang (1971)
Calcite	79±1 (001) 83±1 (010) 87±1 (100)	69-98	Simmons and Wang (1971)
Brass	119±4	100-125	www.engineeringtoolbox.com
Copper	113±3	90-155	Simmons and Wang (1971)
Pyrite	297±33	250-310	Simmons and Wang (1971)
Aluminum	71±1	69-75	Agilent Technologies (2009)
Biotite	37±9	33-102	Mavko et al. (2003)

CHAPTER 4: RESULTS AND DISCUSSION

This chapter presents the results from the analysis of different organic rich shales studies during the course of this thesis. A total of 276 samples were tested using nanoindentation, 134 from Wolfcamp, 69 from Woodford (60 samples by Kumar, (2012a), 36 from Barnett, 16 from Haynesville, 13 from Eagle Ford, 5 from Kimmeridge and 3 from Collingwood, Kumar, 2012a). Petrophysical measurements were carried out on all samples which included: porosity, mineralogy and TOC. Table 6 summarizes number of measurements from each shale studied. Acoustic wave velocities were measured for Wolfcamp shale and data for other shales was taken from Gupta (2012). Mechanical properties of organics were also investigated using nanoindentation. Samples and simulated drill cuttings were tested at elevated temperatures using hot stage. Other rock samples (sandstones, carbonates) were also tested for applicability of nanoindentation on such rocks.

Table 6: Summary of number of samples from each shale and corresponding number of measurements of petrophysical and other parameters in this study.

Play	No. of Samples	Young's Modulus		Hardness		ϕ	TOC	Mineralogy	Acoustic Data	Reference
		Horz	Vert	Horz	Vert					
Wolfcamp	134	134	108	134	108	134	134	134	77	This study
Woodford	9	9	9	9	9	9	9	9	53	This study
	60	60	0	60	0	60	60	60		Kumar, 2012 (a)
Barnett	36	36	25	36	25	36	36	36	0	Kumar, 2012 (a)
Haynesville	16	16	0	16	0	16	16	16	14	Kumar, 2012 (a)
Eagle Ford	13	13	0	13	0	13	13	13	0	Kumar, 2012 (a)
Kimmeridge	5	0	5	0	5	5	5	5	5	Kumar, 2012 (a)
Collingwood	3	3	0	3	0	3	3	3	0	Kumar, 2012 (a)

4.1 Sample Mineralogy

Mineralogy of all 276 samples was determined using FTIR. The average mineralogy for each shale tested is presented in Figure 34. Woodford samples are rich in clay and quartz. Barnett and Wolfcamp samples are rich in clay, quartz and carbonate. Haynesville samples are rich in clay and carbonate with calcite as carbonate mineral and mixed clay and illite as major clay minerals. Eagle Ford samples are rich in carbonate and clays with calcite as the dominant carbonate mineral. Kimmeridge shale is rich in clay and carbonate while Collingwood shale is mostly carbonate. All shales had clays present mostly as illite and mixed clays, while aragonite was the least dominant form of carbonate.

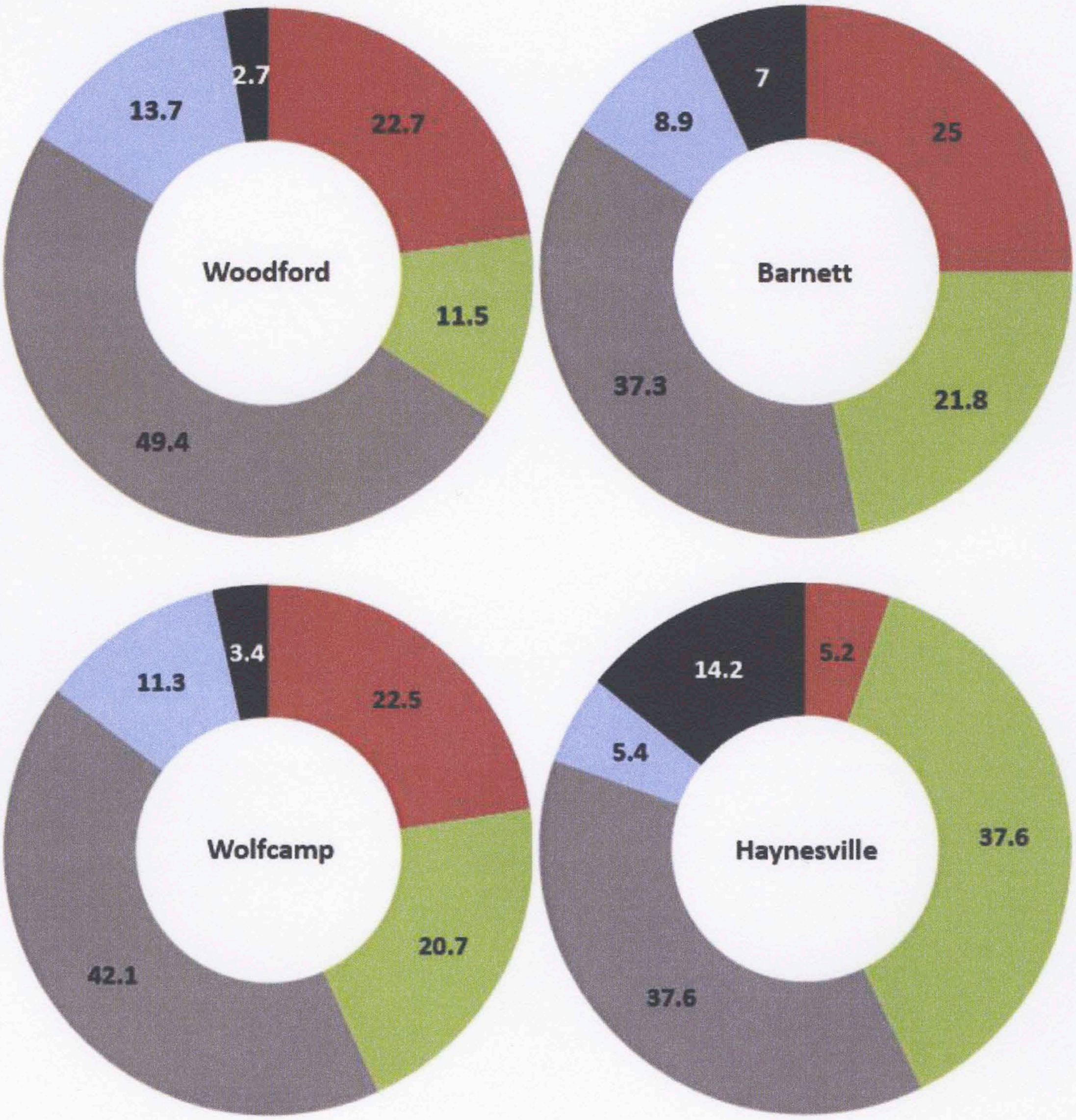

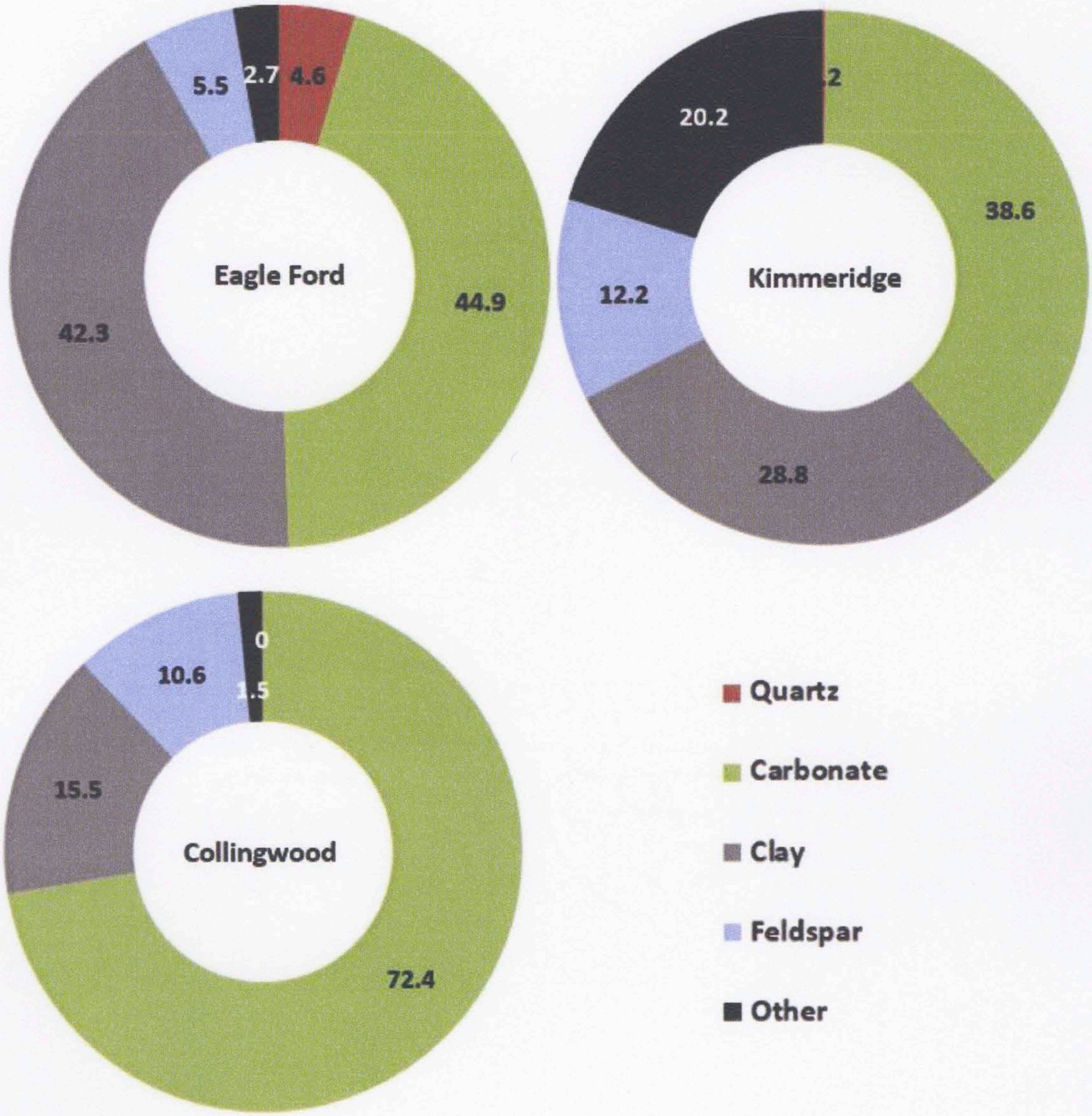

Figure 34: Average FTIR mineralogy of the shales presented in this study.

4.2 Sample Porosity

Figure 35 presents the average porosity for the different shales tested. The 99.999% confidence intervals for Woodford, Barnett, Wolfcamp, Haynesville, Eagle Ford, and Kimmeridge shales were found to be 6.2±0.7%, 5±1%, 4.2±0.8%, 8±2%, 7±1%, and 13±5% respectively.

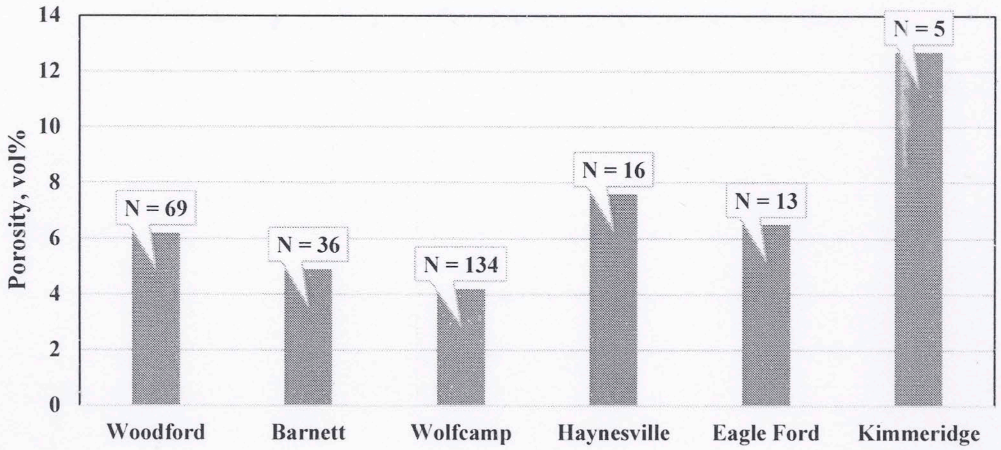

Figure 35: Plot of average helium porosity in different shales. The average porosity for Woodford, Barnett, Wolfcamp, Haynesville, Eagle Ford and Kimmeridge shales are 6.2±0.7%, 5±1%, 4.2±0.8%, 8±2%, 7±1%, and 13±5% respectively. N indicates number of samples from each shale.

4.3 Total Organic Carbon

Figure 36 presents a histogram of average TOC measured for all the shales studied. The 99.999% confidence intervals for Woodford, Barnett, Wolfcamp, Haynesville, and Eagle Ford shales were found to be 6±1, 4±1, 3±0.5, 3±2, and 3±1 wt% respectively. Kimmeridge shale showed the highest average TOC of 28%.

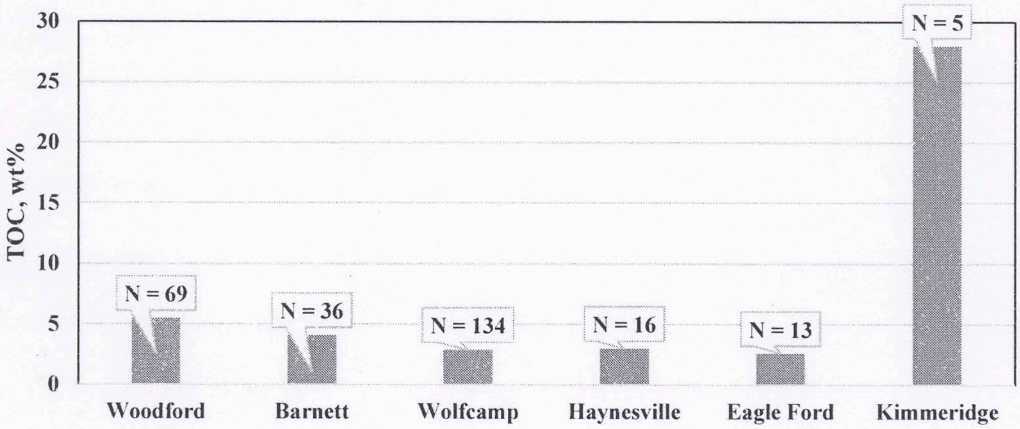

Figure 36: Plot of average TOC in different shales. The average TOC values for Woodford, Barnett, Wolfcamp, Haynesville, Eagle Ford and Kimmeridge shales are 6±1, 4±1, 3±0.5, 3±2, 3.0±1 and 28 wt% respectively. N indicates number of samples from each shale.

4.4 Nanoindentation Results for Different Shale Plays

Nanoindentation was carried out on shale samples following the procedures explained in Chapter 3. Indentations were performed perpendicular as well as parallel to the bedding for 108 Wolfcamp shale, 9 samples from Woodford shale and 25 samples from Barnett shale. Parallel to bedding indentations were done on 26 Wolfcamp samples and 60 Woodford, Haynesville, Eagle Ford, Collingwood samples (Kumar, 2012a). Indentations were done perpendicular to bedding on Kimmeridge shale samples (Kumar, 2012a). For all the shales, lower E_i and H_i were a result of higher clay content, TOC or porosity. Higher E_i and H_i were found for samples having higher content of quartz and carbonate, or lower concentration of softer components namely: porosity, TOC and clay. Bathija et al., (2009) and Mba and Prasad (2010) (from Akrad et al., 2011), have defined "soft" minerals as those having Young's modulus below 30 GPa. Such components include organic matter and clays minerals. "Hard" components include all other rock forming minerals.

4.4.1 Wolfcamp Shale

Indentation Young's modulus, E_i, were measured in the horizontal as well as vertical directions. In the horizontal direction E_i were found to be between 30 and 93 GPa with an average value of 47±4 GPa. In the vertical direction E_i were between 11 and 93 GPa with an average value of 31±6 GPa. Samples with lower E_i had higher amount of clays and organics whereas the ones showing higher E_i were rich in carbonates and showed lower porosity and TOC. Histogram for Young's moduli for 134 horizontal samples and 108 vertical samples are presented in Figure 37 and 38.

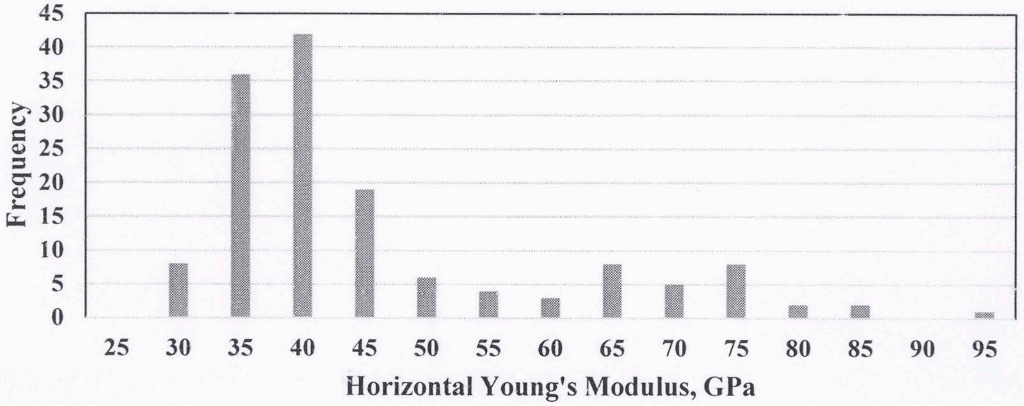

Figure 37: Histogram of horizontal E_i for 134 Wolfcamp shale samples. Average E_i is 47±4 GPa. Samples with higher TOC, clay and porosity showed lower E_i and vice versa.

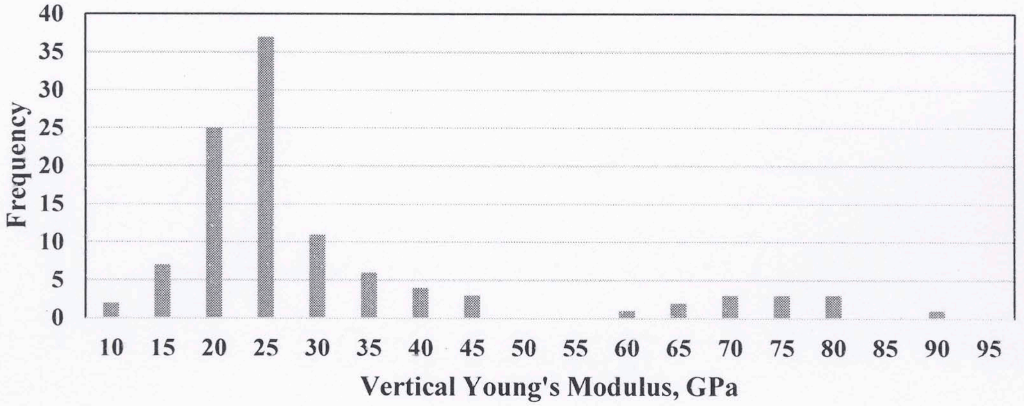

Figure 38: Histogram of vertical E_i for 108 Wolfcamp shale samples. Average E_i is 31±6 GPa. Samples with higher TOC, clay and porosity showed lower E_i and vice versa.

Hardness was also measured along with Young's modulus in both directions. In the horizontal directions H_i ranged between 0.48 to 6.67 GPa with an average value of 1.5±0.3 GPa. In the vertical direction H_i was found to be between 0.36 to 6.98 GPa with an average value of 0.9±0.3 GPa. Figure 39 and 40 show histograms for hardness measurements for 134 horizontal and 108 vertical samples from Wolfcamp shale.

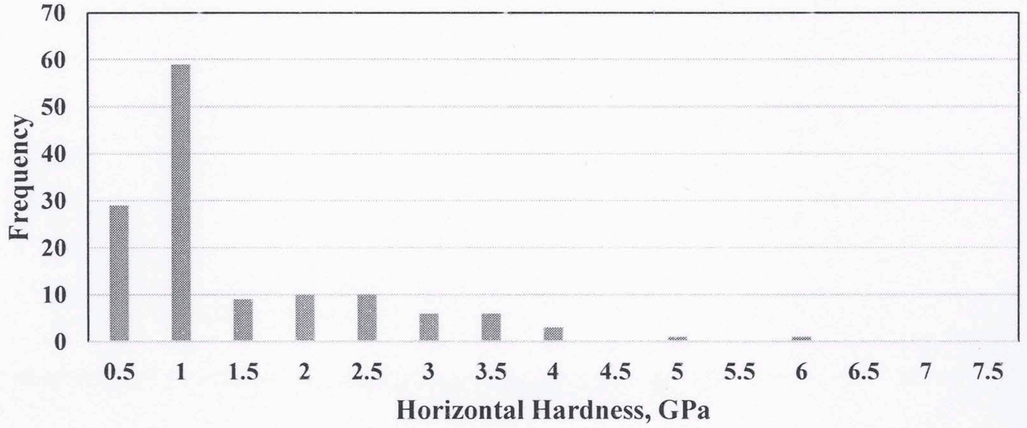

Figure 39: Histogram for horizontal H_i for 134 Wolfcamp shale samples. Average H_i is 1.5±0.3 GPa. Samples with higher hardness (>3 GPa) were found to be rich in carbonates.

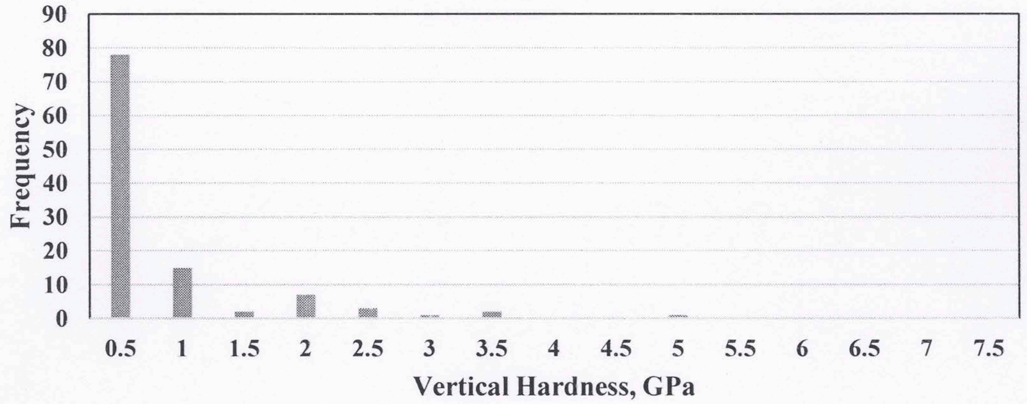

Figure 40: Histogram for vertical H_i for 108 Wolfcamp shale samples. Average H_i is 0.9±0.3 GPa. Samples with higher hardness (>3 GPa) were found to be rich in carbonates.

4.4.2 Young's Modulus and Hardness of Other Shales

Histograms for E_i for Woodford, Barnett, Haynesville and Eagle Ford shales (Kumar, 2012a) are shown in Figures 41 to 44. Histograms for Hi are shown in Figures 45 to 48.

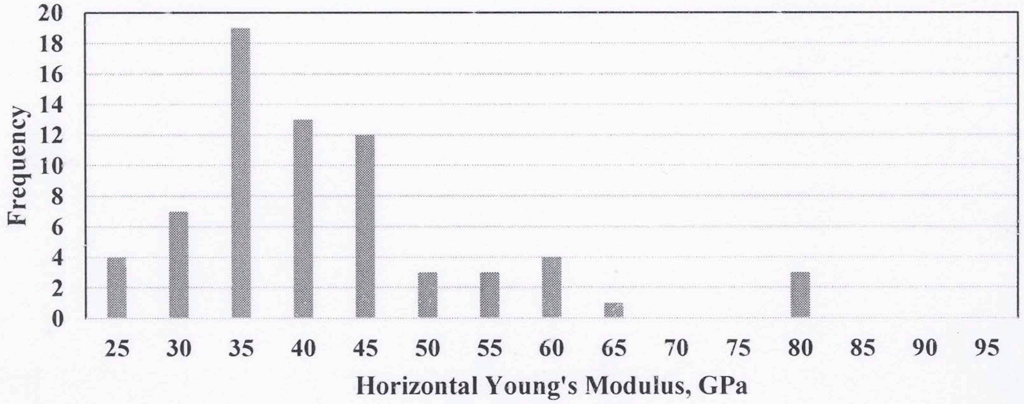

Figure 41: Histogram for horizontal E_i for 69 Woodford shale samples. E_i ranges from 23 to 82 GPa and average Ei is 42±5 GPa. Samples with low TOC, porosity and clay content showed higher E_i and vice versa.

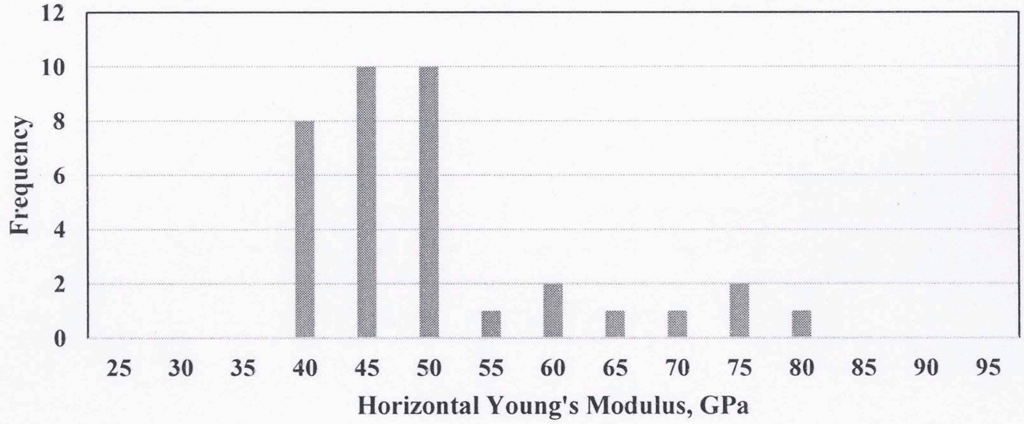

Figure 42: Histogram for horizontal E_i for 36 Barnett shale samples. E_i ranges from 39 to 78 GPa and average E_i is 50±6 GPa. Samples rich in carbonate or low in TOC and porosity showed higher Ei values.

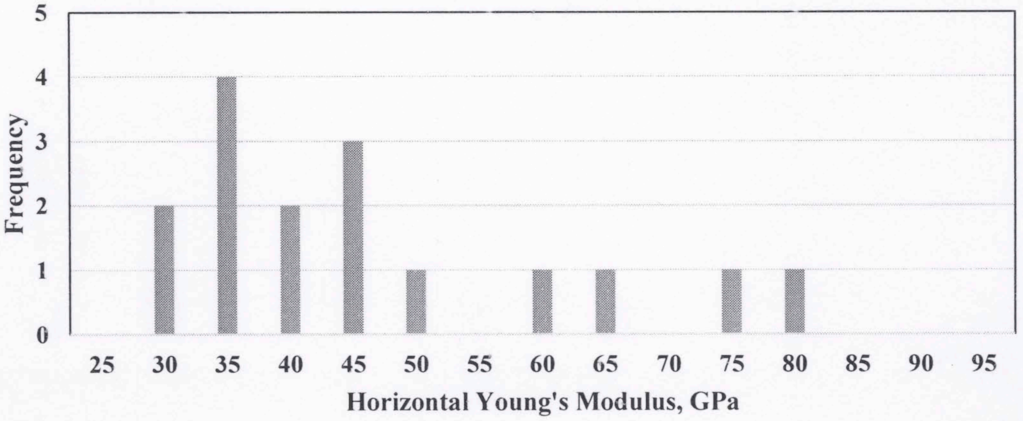

Figure 43: Histogram for horizontal E_i for 16 Haynesville shale samples. E_i ranges from 31 to 79 GPa and average E_i is 47±16 GPa. Samples rich in carbonate or low in TOC showed higher E_i values. Large variability in Young's modulus observed due to a smaller sample size.

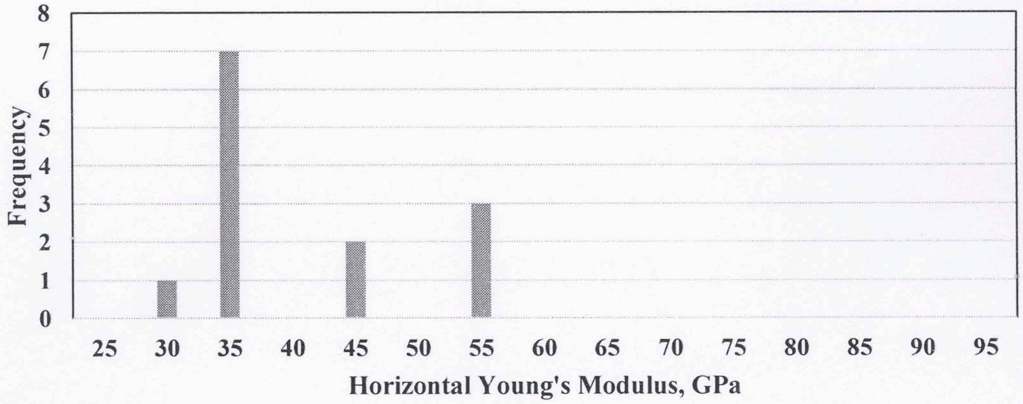

Figure 44: Histogram for horizontal E_i for 13 Eagle Ford shale samples. E_i ranges from 31 to 58 GPa and average E_i is 41±11 GPa. Samples with higher carbonate content exhibited higher E_i values.

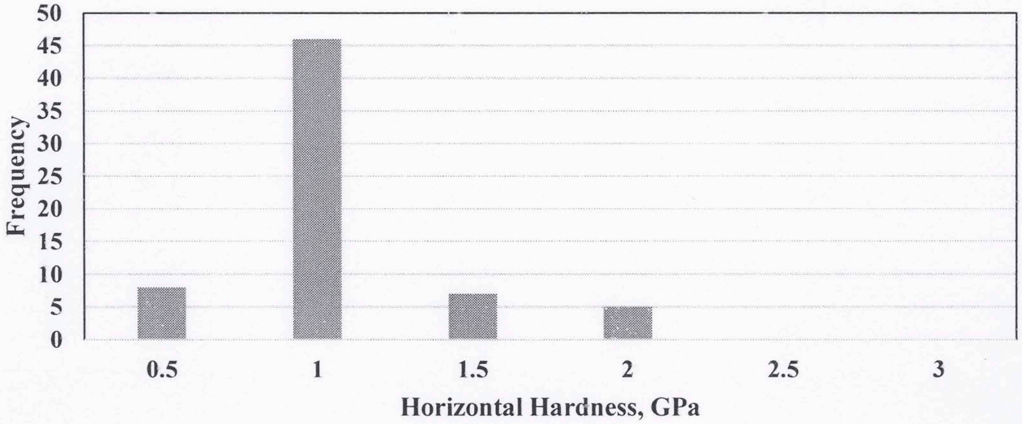

Figure 45: Histogram for horizontal H_i for 69 Woodford shale samples. H_i ranges from 0.54 to 2.12 GPa and average H_i is 1.1±0.2 GPa. Samples with higher hardness (>5 GPa) were found to be rich in quartz.

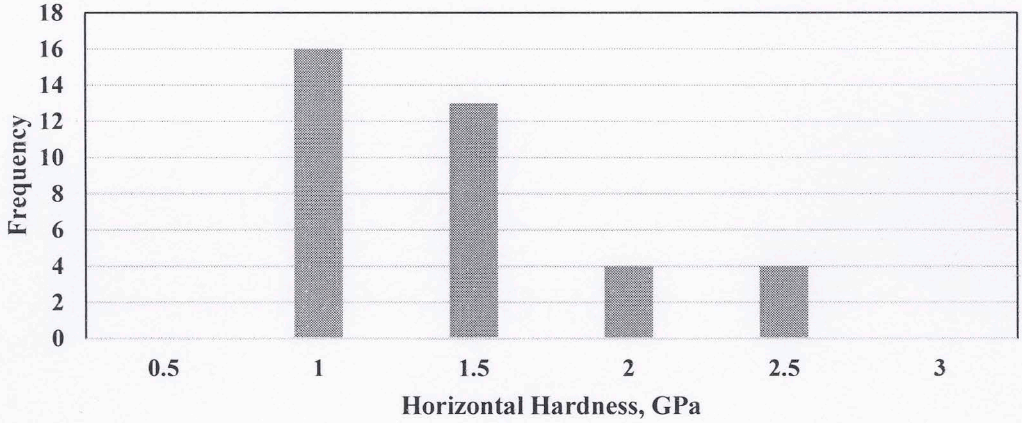

Figure 46: Histogram for horizontal H_i for 36 Barnett shale samples. H_i ranges from 0.78 to 2.6 GPa and average H_i is 1.4±0.3 GPa.

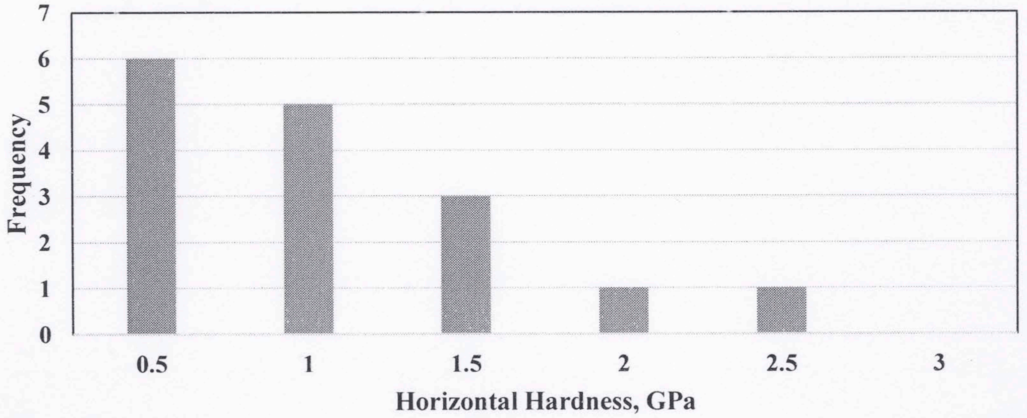

Figure 47: Histogram for horizontal H_i for 16 Haynesville shale samples. H_i ranges from 0.55 to 2.28 GPa and average H_i is 1±0.6 GPa. Samples rich in carbonate showed higher hardness.

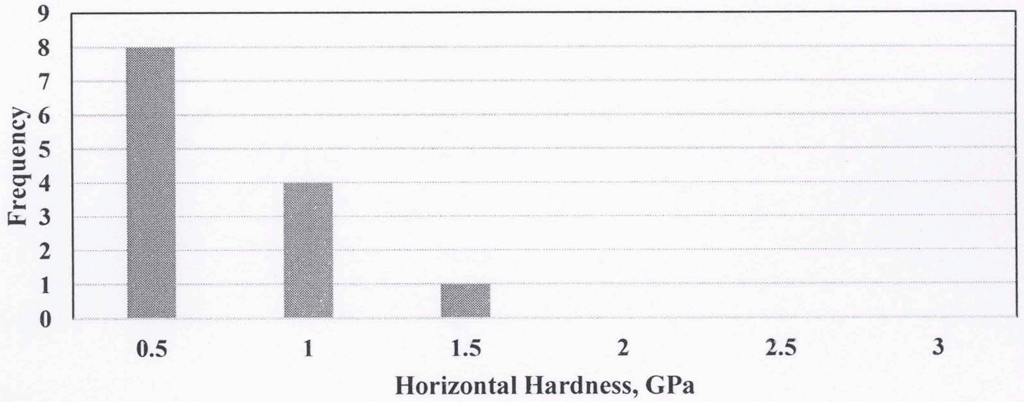

Figure 48: Histogram for horizontal H_i for 13 Eagle Ford shale samples. H_i ranges from 0.45 to 1.5 GPa and average H_i is 0.8±0.4 GPa.

Wider confidence interval in Eagle Ford and Haynesville shales was a result of smaller sample size. Three samples from Collingwood shale and 5 samples from Kimmeridge shale were also tested using nanoindentation. Collingwood samples showed high carbonate content of 73±4 wt%, low clay content of 16±3 wt% and no quartz. E_i ranged between 49 to 57 GPa with an average Ei of 54±5 GPa. H_i ranged from 1 to 1.3 GPa with average H_i of 1.2±0.2 GPa. Kimmeridge samples were rich in organics and showed a TOC of 28±20 wt% and porosity of 13±5.3%. E_i ranged from 5 to 11 GPa with average E_i of 7.4±3 GPa. H_i ranged from 0.26 to 0.35 GPa with average H_i of 0.3±0.04 GPa. Due to fewer number of samples in Kimmeridge and Collingwood shales, the standard deviation in values were used as the confidence interval for all the parameters reported. Table 7 presents a summary of horizontal E_i and H_i measurements and their 99.999% confidence intervals for all shales tested.

Table 7: Summary of average horizontal E_i and H_i and their 99.999% confidence intervals (CI) for all shales plays.

Shale	No. of	Average	CI_E, GPa	Average	CI_H, GPa
Wolfcamp	134	47	4.2	1.48	0.3
Woodford	69	42	5	1.07	0.2
Barnett	36	50	6	1.41	0.3
Haynesville	16	47	16	1.06	0.6
Eagle Ford	13	41	11	0.77	0.4
Kimmeridge	5	7.4	3	0.3	0.04
Collingwood	3	54	5	1.2	0.2

4.5 Effect of Heterogeneity on Nanoindentation Results

Variation in Young's moduli for a sample could be a result of improper polishing, incorrect calibrations or heterogeneity in the sample. We limit ourselves to discussions on sample heterogeneity assuming that other errors are negligible and do not vary based on tests on standards. Harder and softer minerals are unevenly distributed in some shales resulting in spatially varying Young's modulus.

Analysis of Wolfcamp shale data for three wells; Well#1, Well#2 and Well#3, is presented in Figure 49. The data shows different standard deviations for the three wells. Samples from these wells were tested at every 3 to 5 feet interval and the corresponding FTIR mineralogy charts are presented in Figures 50 to 52. 60 samples were taken from Well#1 and it was found to be mostly rich in quartz and clay with a few carbonate streaks in between. Bottom part of the well was part of a limestone and had high presence of carbonates. 48 samples were taken from Well#2 and it was found to be rich in quartz and clay throughout its depth. 26 samples were taken from Well#3 and it was rich in quartz and carbonate. Observations from all the wells suggest that nanoindentation results for samples rich in quartz and clay showed smaller standard deviation (less than 5 GPa) while samples rich in carbonates showed larger standard deviations (up to 17 GPa). It was observed that more than about 40 wt% carbonate in a sample results in this change of behavior. Such a trend can be clearly observed in Figure 49. Well#1 was rich in quartz and clay hence it also showed the distribution of standard deviations (shown in blue) skewed towards the lower side. Average standard deviation was 4 GPa. Well#2 was rich in quartz and clay and showed lower standard deviation (shown in red). Average standard deviation was found to be 3 GPa. Well#3 was rich in quartz and carbonate and showed standard deviations (shown in purple) on the higher side. Average standard deviation was found to be 10 GPa. Combined histogram for standard deviations from 3 wells is shown in orange. Although quartz is harder than carbonates, its presence did not make a significant difference because quartz grain size was in the shale particle size range. On the other hand carbonates were seen to be present as clusters with clear grain boundaries.

SEM studies reveal the reason, behind the larger standard deviations in Young's moduli (100 indentations) for samples having larger carbonate concentration. Figure 53 shows an Energy Dispersive Spectroscopy (EDS) map for an array of 25 indentations for a sample from Well#1. Here image 1 shows the BSE image of the sample indicating higher density material by bright color. The sample contained 33 wt% quartz, 51 wt%

clays, 8 wt% carbonates, 4.7 wt% TOC and 7.2% porosity. The EDS map shows uniform distribution of all the elements. Presence of silicon indicates quartz, aluminum is related to presence of clays. Some amount of calcium and magnesium was also present but was scattered uniformly throughout the area. Pyrite was present as iron sulfides in the sample in trace amounts. This uniformity in distribution of elements is reflected in the low scatter in Young's moduli values, i.e. ±2.4 GPa.

Figure 54 shows EDS map for another sample from Well#1 over a 25 indentation array. This sample contained 30 wt% quartz, 38 wt% carbonates, 23 wt% clays, 1.7 wt% TOC and 1.8% porosity. The EDS map shows non-uniform distribution of all the elements with carbonates being present as clusters at various locations. The BSE image shows carbonates mainly present as calcite ($CaCO_3$) and some as dolomite [$(Ca, Mg)CO_3$] by brighter color. Some indentations are on carbonate rich areas and some in clays. This led to larger scatter in the results 99.999 confidence intervals increased from from ±2 GPa to ±3GPa.

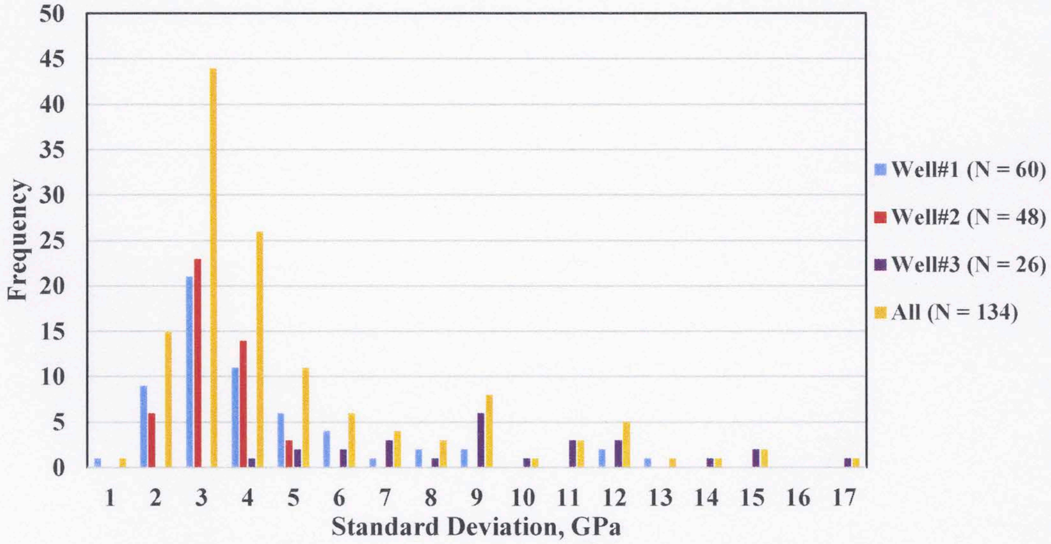

Figure 49: Histogram of standard deviation of Young's moduli for three wells (134 samples) from Wolfcamp shale. The mean standard deviation is 4.92 GPa.

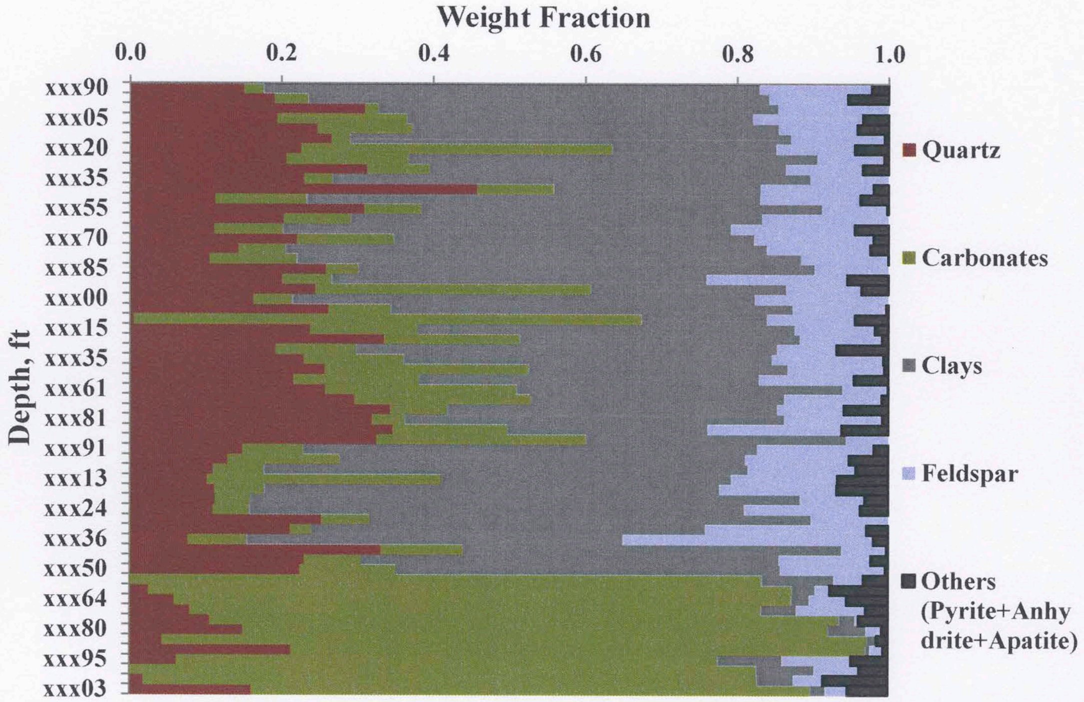

Figure 50: FTIR Mineralogy versus depth for Well#1. Top section of the well is rich in quartz and clay while bottom section was limestone. Few high carbonate streaks were also present.

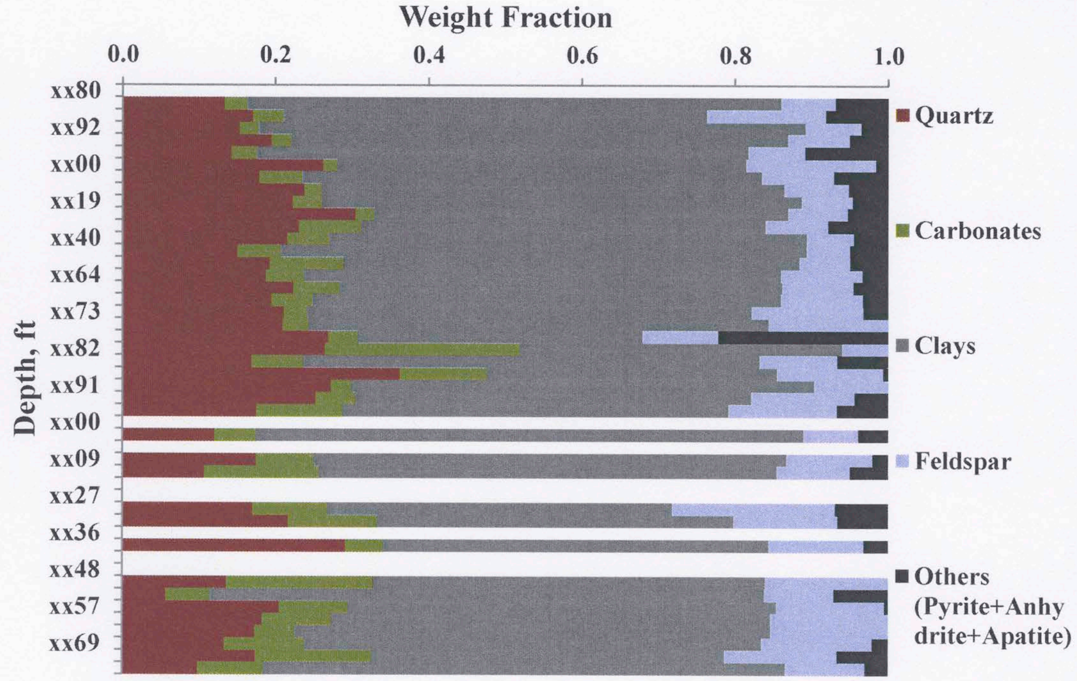

Figure 51: FTIR Mineralogy versus depth for Well#2 showing presence of quartz and clay throughout the well. Blank portions indicate missing data.

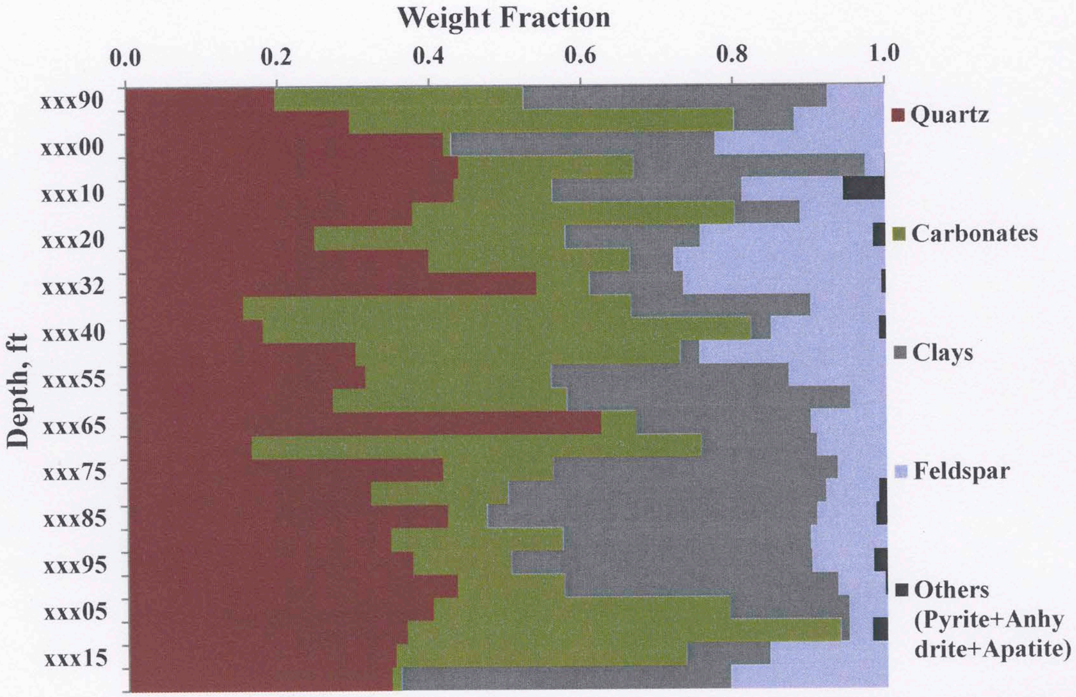

Figure 52: FTIR Mineralogy versus depth for Well#3 showing presence of quartz and carbonate throughout the well. Top half showed less clay compared to bottom half of the well.

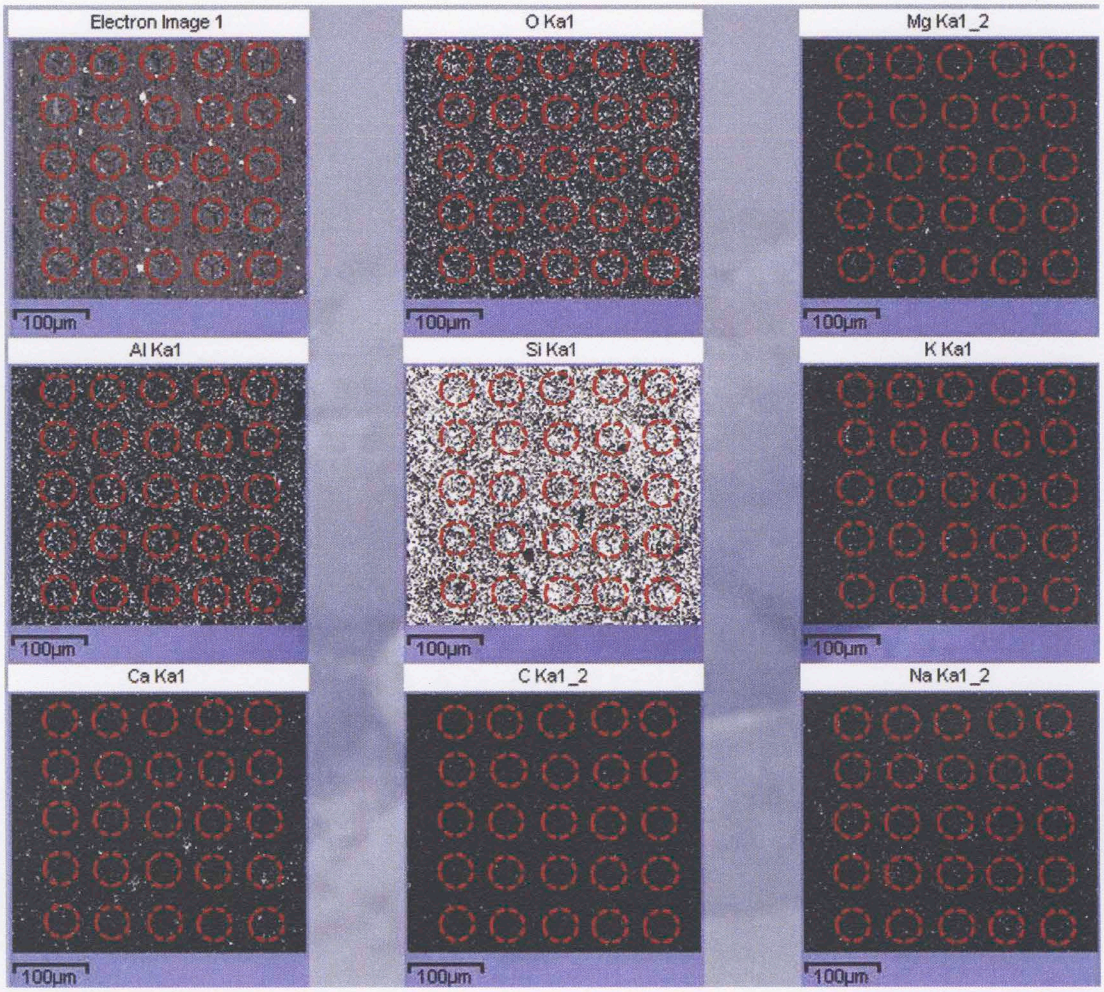

Figure 53: BSE image and Energy Dispersive Spectroscopy (EDS) elemental maps for 25 indentation sites after nanoindentation. Circles mark the indentation locations. Fairly uniform distribution of elements like Si, Al, Ca and Mg is observed implying sample mineralogical homogeneity. This led to smaller scatter in measured Young's modulus.

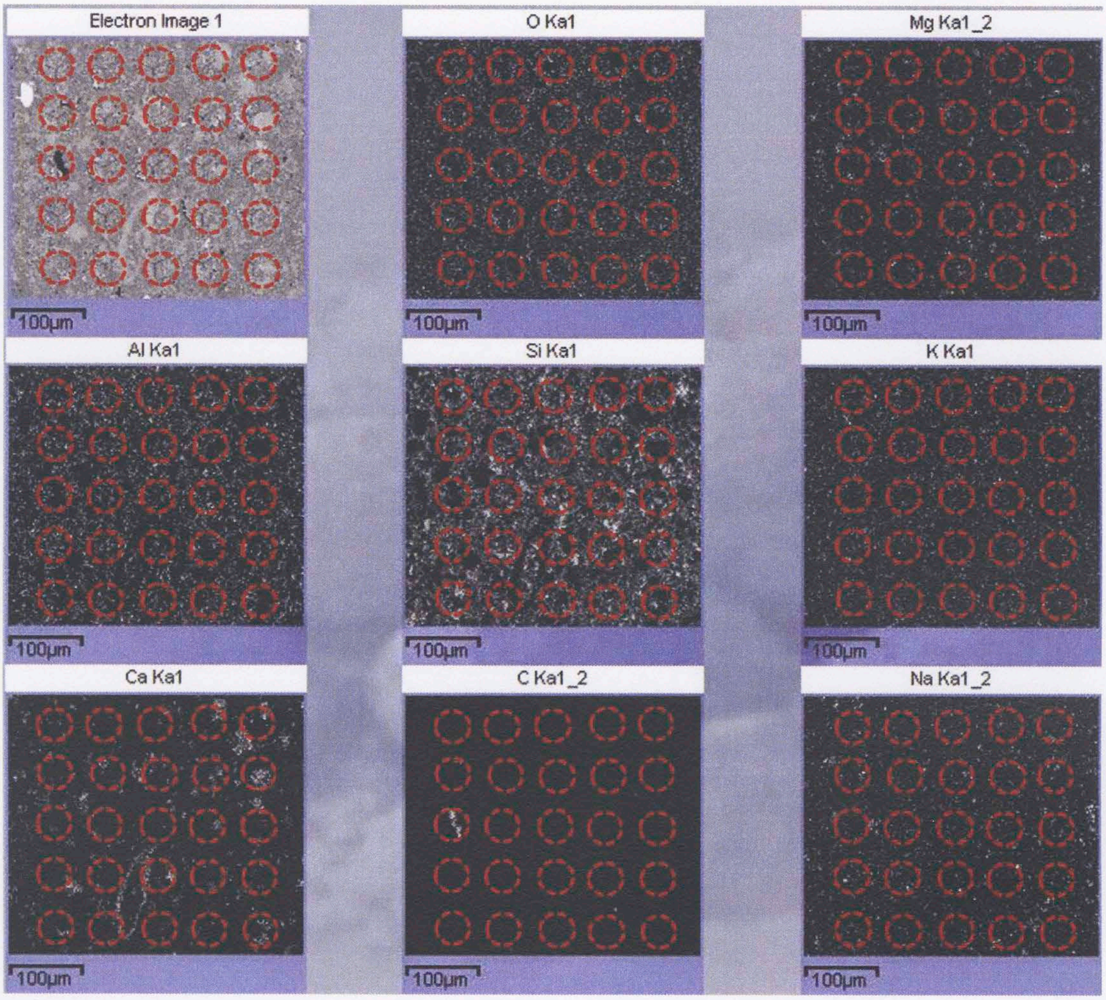

Figure 54: BSE image and Energy Dispersive Spectroscopy (EDS) elemental maps for 25 indentation sites after nanoindentation. Circles indicate indentations locations. Uneven distribution of elements was observed in this sample with Ca present as clusters. This led to larger scatter in measured Young's moduli.

Kumar, (2012a) has discussed his results on nanoindentation and the corresponding standard deviations for 100 indentations for samples from Woodford, Barnett, Haynesville, Eagle Ford, Kimmeridge and Collingwood shales. Figure 55 shows histogram of standard deviations for these shales as reported by Kumar, (2012a). Abousleiman et al., (2009) have studied samples from outcrops of Woodford shale and have found standard deviations from 1.95 to 3.8 GPa, which were considerably lower than the results reported by Kumar (2012a). These outcrop samples also showed low

Young's moduli of 8 to 10 GPa which could be the result of rock weakening due to weathering.

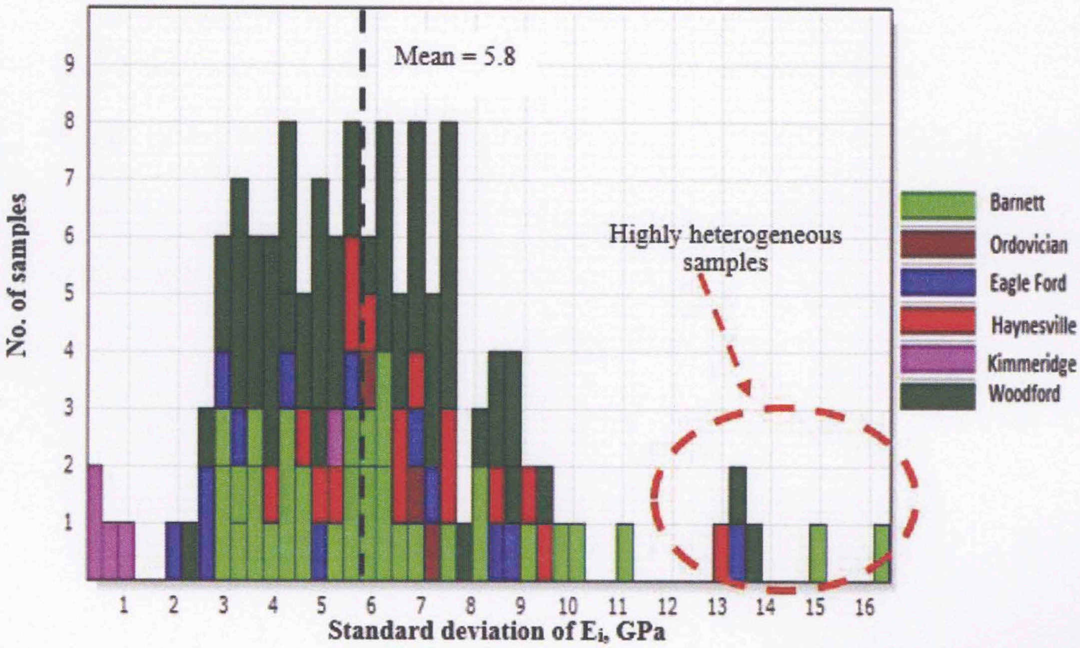

Figure 55: Histogram of standard deviations of Young's moduli for 144 shale samples. Mean standard deviation was 5.8 GPa; some highly heterogeneous samples showed standard deviation as high as 16 GPa (Kumar, 2012a).

This analysis indicates that there is variation in shale mineralogy across different shale plays. More calcite led to higher standard deviation in Young's modulus due to the inhomogeneous distribution of calcite. Variation in mineralogy was also observed vertically within each well. Streaks of high carbonate concentration were observed along the depth which have large Young's modulus values. Calcite was observed to be present in discrete clusters which also leads to lateral variation in mineralogy along the sample surface as indicated by SEM and nanoindentation studies.

4.6 Effect of Mineralogy, Porosity and TOC on Shale Mechanical Properties

Mechanical properties depend on rock composition and are affected by a number of factors which include soft components: porosity, TOC, clay content; and hard components: quartz, carbonates and pyrites. If all these parameters are measured accurately then they could be used to predict Young's modulus and hardness for a rock by developing empirical equations. Mineralogy, TOC and porosity were measured following the procedures explained in Chapter 3. Nanoindentation and petrophysical properties were measured on the same piece of sample. Vertical and horizontal indentation were made on two perpendicular vertical and horizontal faces of the sample. Plots of variation of TOC, porosity, grain density, bulk density, Young's modulus (vertical and horizontal) and indentation hardness (vertical and horizontal) with mineralogy for Well#1, Well#2 and Well#3 are presented in Figures 57 to 65. It can be seen in Figures 57, 60 and 63 that decrease in TOC is also accompanied by decrease in porosity which indicates that considerable amount of porosity is contained in the organics (Figure 56).

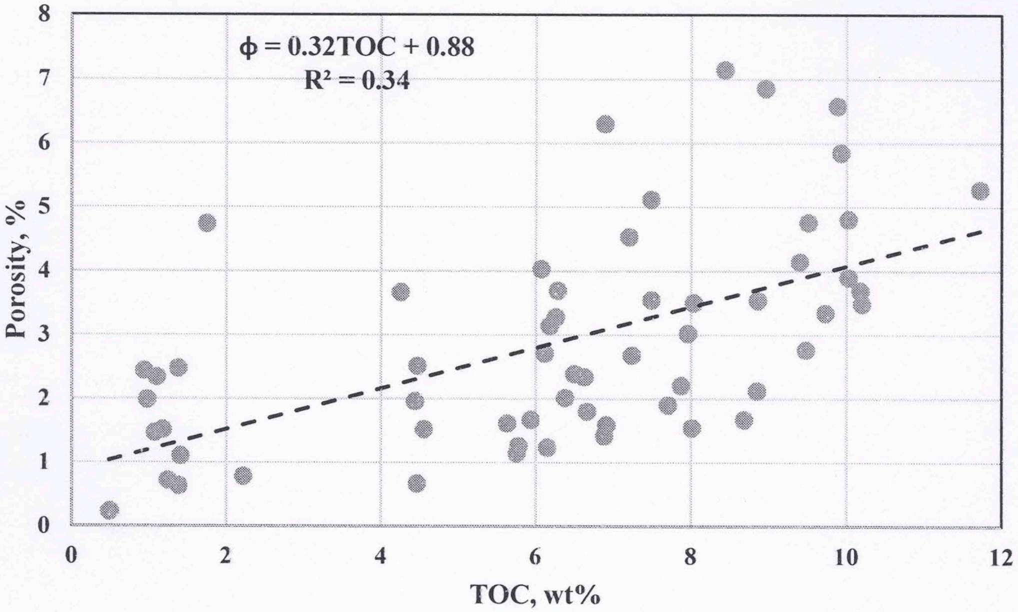

Figure 56: Plot of porosity versus TOC for Well#1. Porosity was found to increase with TOC indicating that porosity is also contained in organics. Well#2 and Well#3 did not show dependence between porosity and TOC.

At the same time, grain and bulk densities also decreased due to larger presence of low density material in the rock. Figures 58, 61 and 64 show the effect of mineralogy on Young's modulus. It was observed that higher concentrations of carbonates (more that 40%) results in a sharp increase in Young's modulus (E_H and E_V). Similar effect was observed due to the presence of quartz but increase in modulus as a result of high quartz concentration was not as significant. Young's modulus was found to decrease at depths where clay concentration was large. Similar observations were made for the variation of indentation hardness with mineralogy and are presented in Figures 59, 62 and 65.

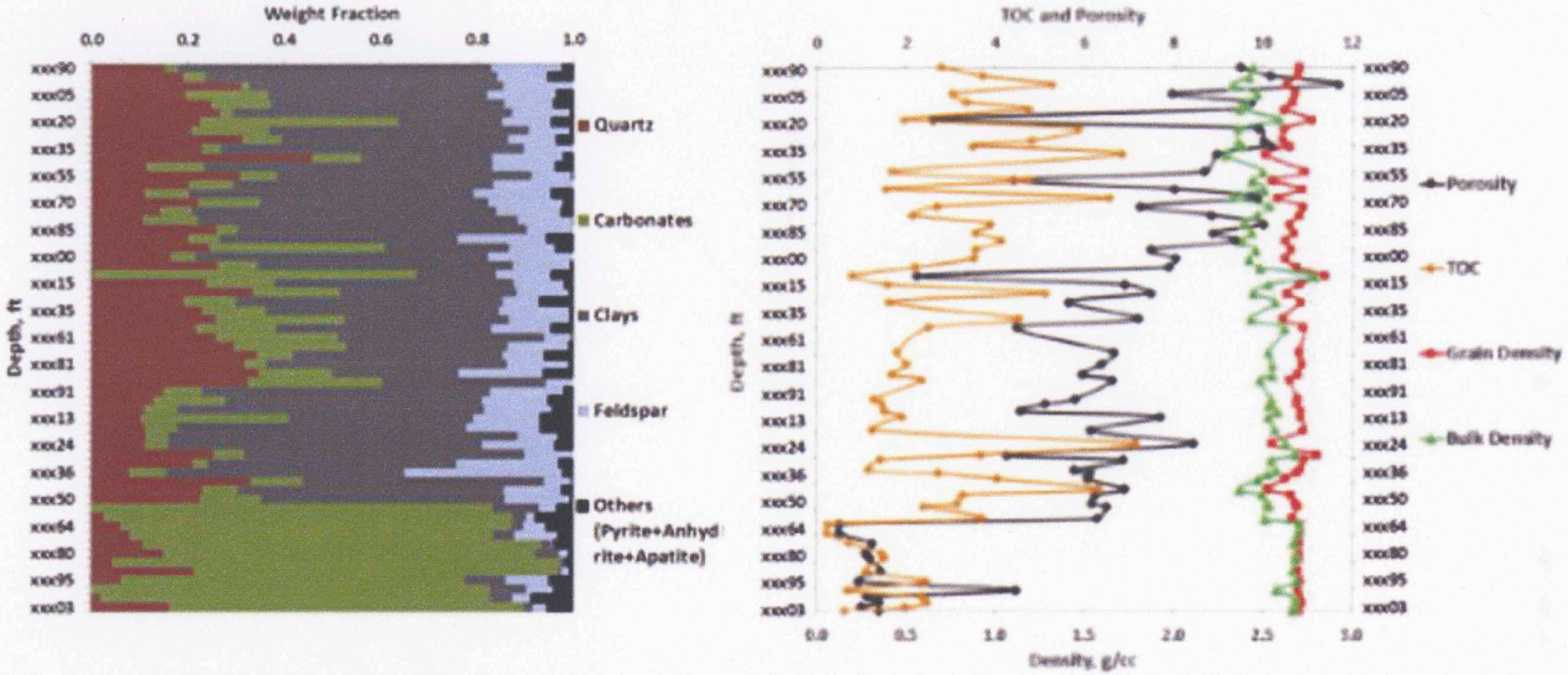

Figure 57: Plots for Well#1; (Left) Mineralogy versus depth. (Right) Porosity, TOC and density versus depth. Changes in mineralogy are related to changes in TOC, porosity, bulk density and grain density. Increase in TOC is related to increase in porosity and vice versa. High carbonate concentration at the bottom of the well was limestone.

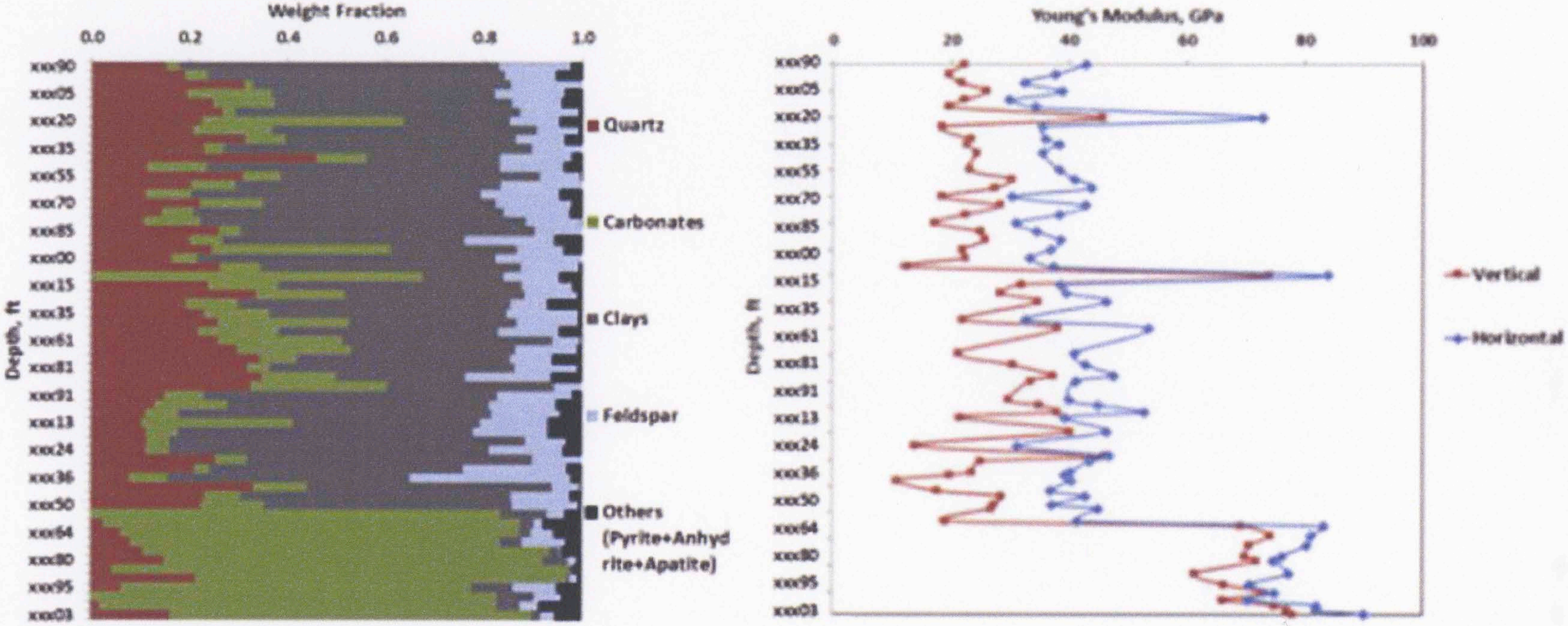

Figure 58: Plots for Well#1; (Left) Mineralogy versus depth. (Right) Vertical and horizontal Young's modulus versus depth. Good dependence of Young's modulus on mineralogy is observed. Note the strong anisotropy in Young's modulus; the average E_H/E_V=1.64. High Young's modulus are marked by more than 40% carbonate concentration. High carbonate concentration at the bottom of the well was limestone.

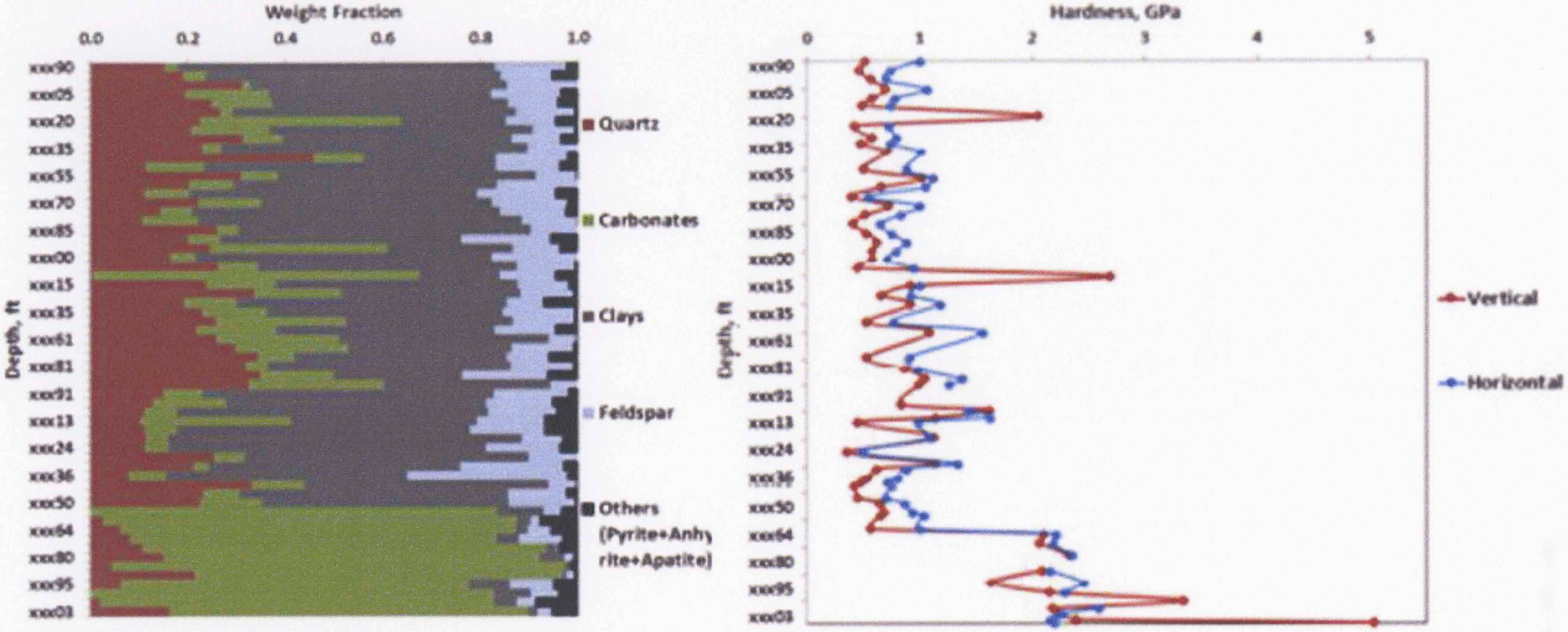

Figure 59: Plots for Well#1; (Left) Mineralogy versus depth. (Right) Vertical and horizontal indentation hardness versus depth. Good dependence of hardness on mineralogy is observed. High hardness is marked by more than 40% carbonate concentration. High carbonate concentration at the bottom of the well was limestone.

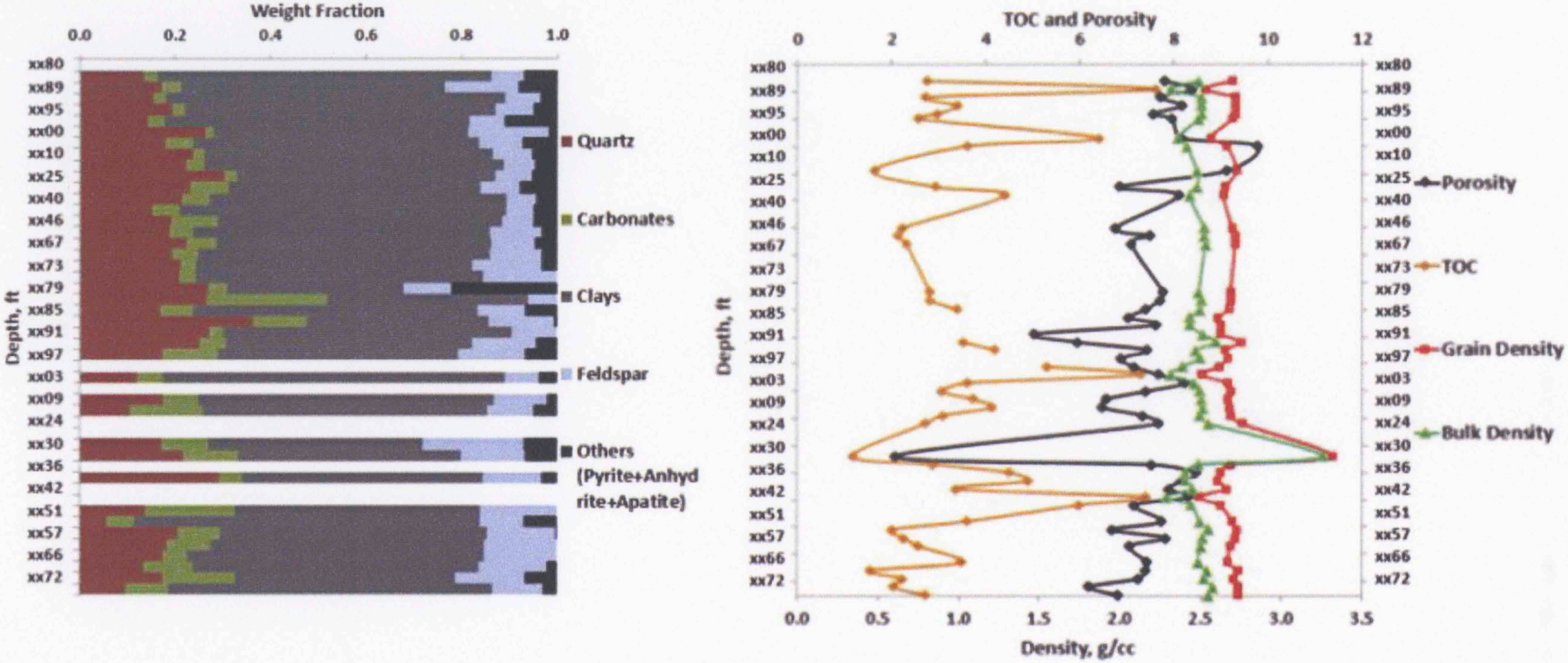

Figure 60: Plots for Well#2; (Left) Mineralogy versus depth. (Right) Porosity, TOC and density versus depth. Changes in mineralogy are related to changes in TOC, porosity, bulk density and grain density. Increase in TOC is related to increase in porosity and vice versa.

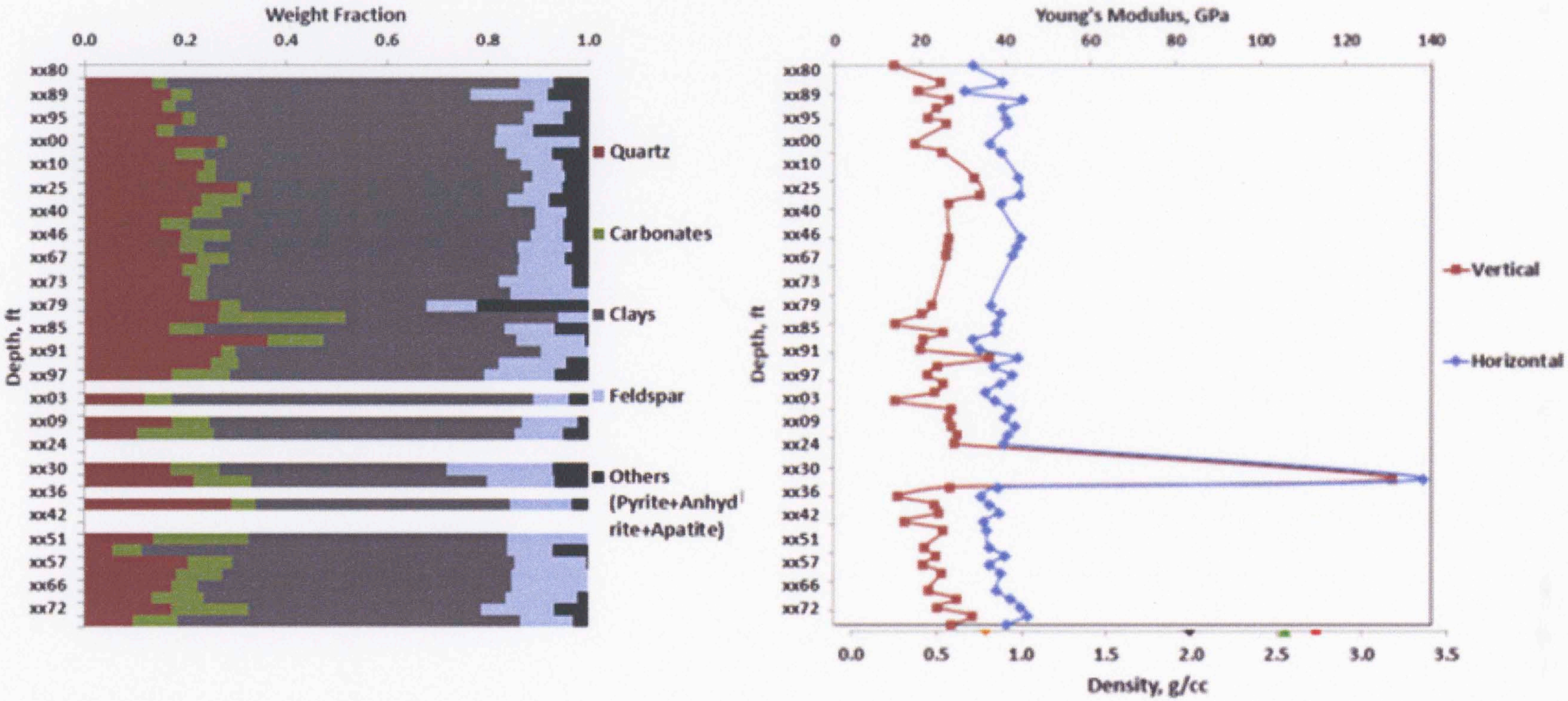

Figure 61: Plots for Well#1; (Left) Mineralogy versus depth. (Right) Vertical and horizontal Young's modulus versus depth. Good dependence of Young's modulus on mineralogy is observed. Note the strong anisotropy in Young's modulus; the average E_H/E_V=1.65. Peak in Young's modulus was due to high concentration of pyrites in the sample.

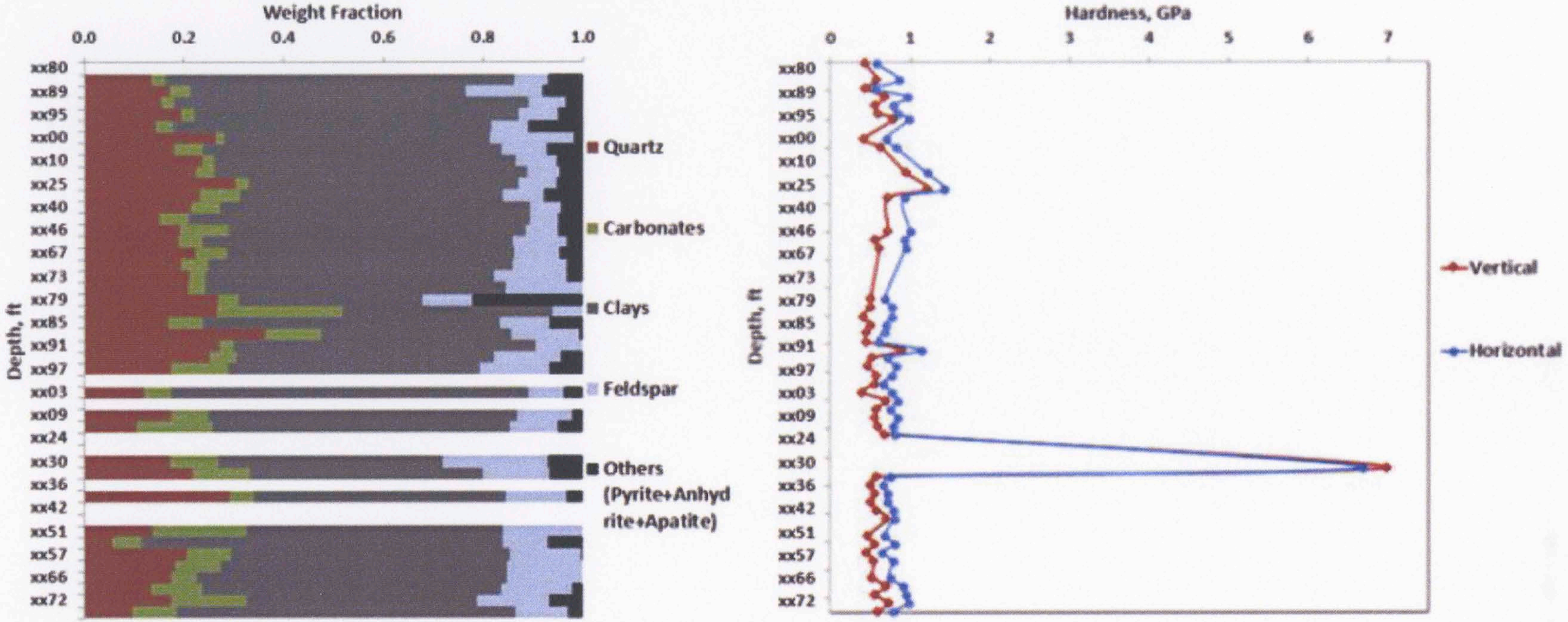

Figure 62: Plots for Well#1; (Left) Mineralogy versus depth. (Right) Vertical and horizontal indentation hardness versus depth. Good dependence of hardness on mineralogy is observed. Peak in indentation hardness was due to high concentration of pyrites in the sample.

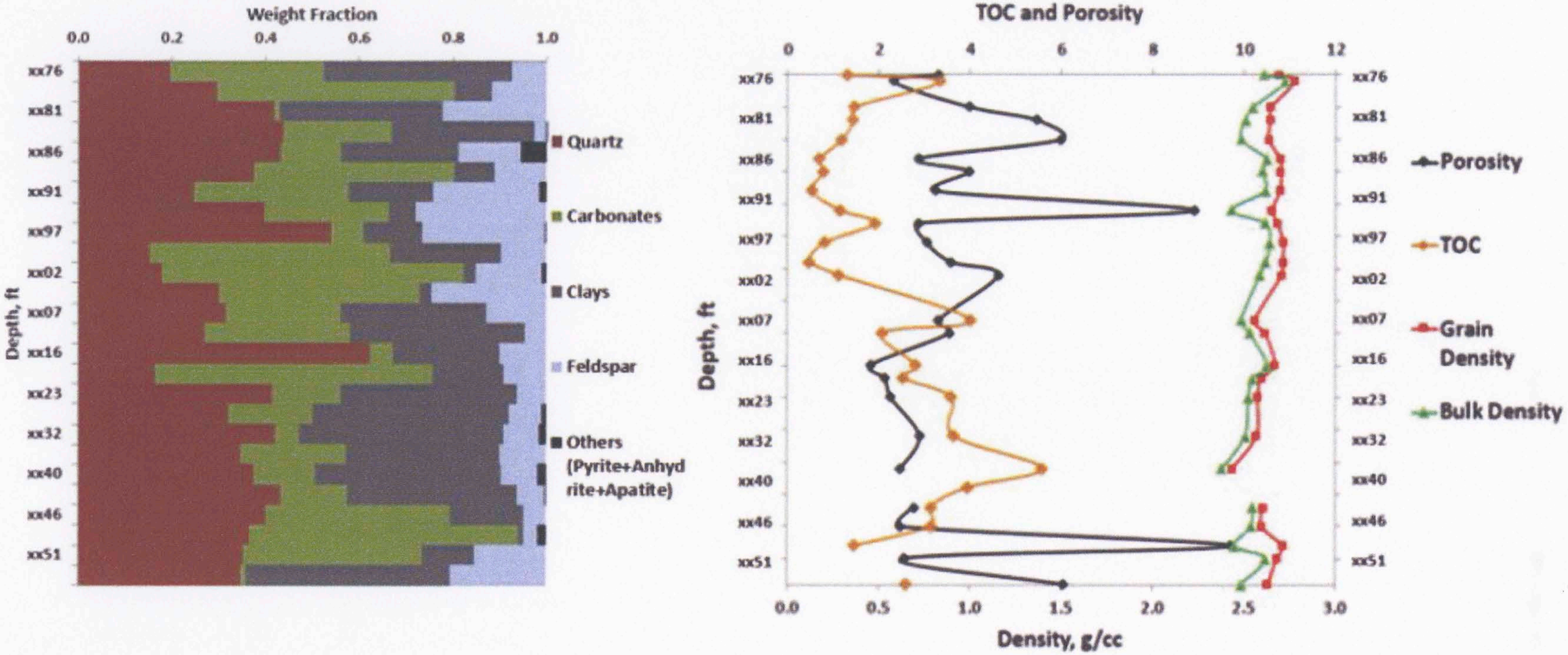

Figure 63: Plots for Well#3; (Left) Mineralogy versus depth. (Right) Porosity, TOC and density versus depth. Changes in mineralogy are related to changes in TOC, porosity, bulk density and grain density. Increase in TOC is related to increase in porosity and vice versa.

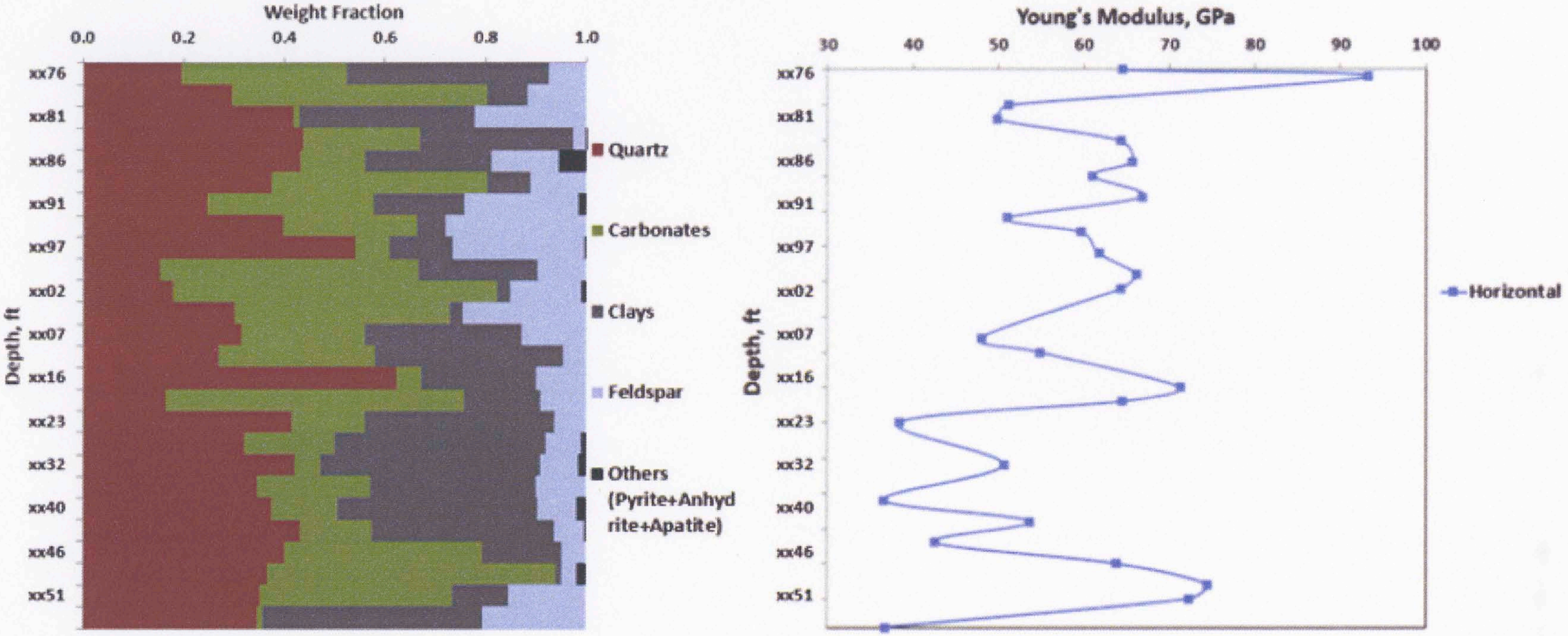

Figure 64: Plots for Well#3; (Left) Mineralogy versus depth. (Right) Horizontal Young's modulus versus depth. Good dependence of Young's modulus on mineralogy is observed. Young's modulus was found to be larger in Well#3 due to larger concentration of harder components: quartz and carbonates.

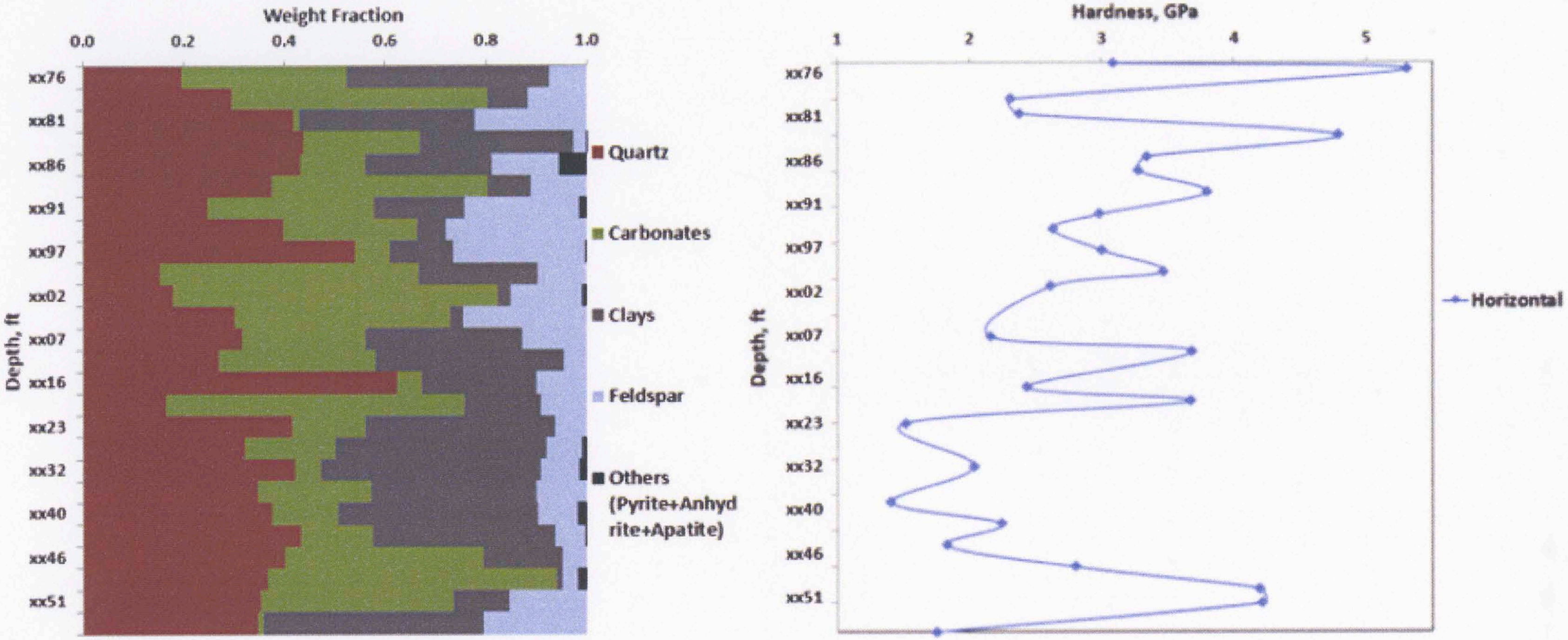

Figure 65: Plots for Well#3; (Left) Mineralogy versus depth. (Right) Horizontal indentation hardness versus depth. Good dependence of hardness on mineralogy is observed. Hardness was found to be larger in Well#3 due to larger concentration of harder components: quartz and carbonates.

Kumar, (2012a) classified shales in two groups based on mineralogy; quartz rich samples from Woodford and Barnett shales were treated as one group while carbonate rich samples from Haynesville, Eagle Ford and Collingwood shales were treated as second group. A combined analysis of all shales was performed to understand the relationship between mechanical properties and measured petrophysical parameters. This study combines data from Wolfcamp shale for the three wells to the previous work by Kumar, (2012a). In the first part, data from all the shale plays is analyzed. In the second part, Wolfcamp shale is studied separately. This will help to understand whether the general trends obtained for shales are same as trends for a single shale or does each shale needs to be treated separately. Finally shales were grouped in terms or clay, quartz and carbonate richness. Results from second and third part are presented in Appendix A.

First part: For this analysis, plots of Young's modulus were prepared versus porosity, TOC, and mineral compositions. These plots include some sample points from Well#1 which come from a limestone section below the shale. Although they are shown in the plot, but they do not form a part of the analysis and were ignored for making the trendlines in Figures 66 to 69 and 71 to 74. Figure 66 shows a plot of Young's modulus versus porosity. It was observed that samples rich in clay also had higher porosity. Increase in porosity results in a weaker rock, hence a reduced Young's modulus decreases. Throughout all shales, there is a negative trend in the plot of Young's modulus versus porosity. As reported by Kumar, (2012a), the size of indentations (>30µm) is larger than the pore size (2-8 nm) as confirmed by mercury injection and SEM studies by Sondergeld and Rai, (2011), and Curtis et al., (2010).

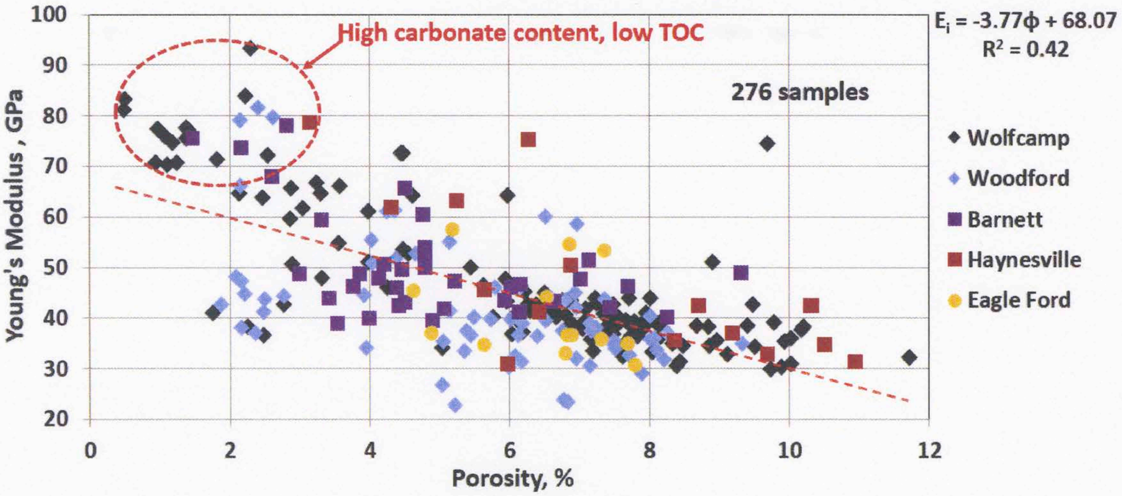

Figure 66: Horizontal Young's modulus versus porosity for different shale plays. There is a decreasing trend in Young's modulus with increase in porosity described by the linear equation Ei = 68.07 – 3.77φ. Points encircled in red are from sections rich in carbonates and low in TOC. Data from carbonate section in Well#1 was ignored. Scatter is observed to decrease at high porosity.

Figure 67 shows a plot of Young's modulus versus clay content for all the shales. Clays are believed to be softer material (Katahara, 1996), hence an increase in clay content is expected to decrease Young's modulus. Clays are ductile and have the tendency to creep (Sone and Zoback, 2010). Zargari et al., (2011), have also made similar findings about decreasing Young's modulus with increasing clay content. Young's modulus show better correlation with clays as compared to porosity.

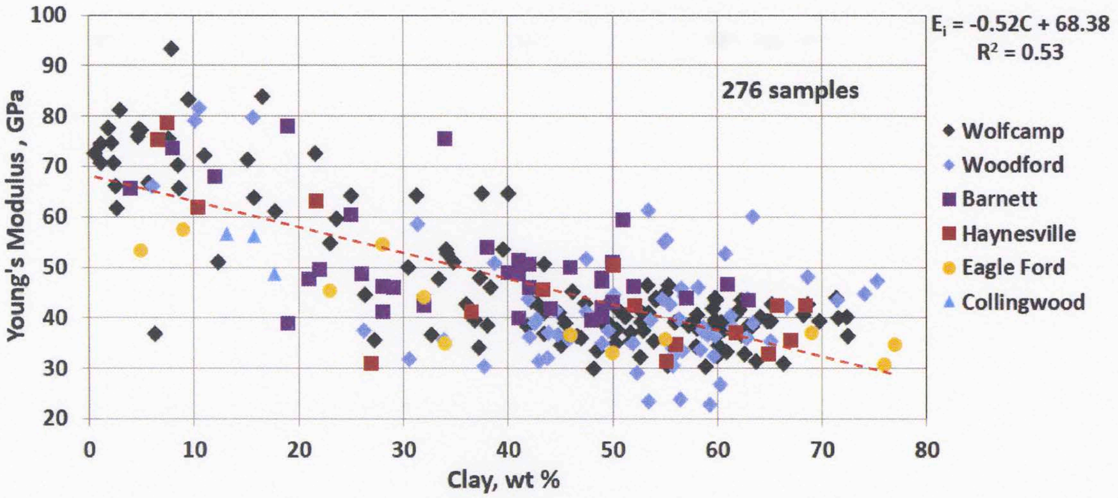

Figure 67: Young's modulus versus clay content for all the shales studied. There is a decreasing trend in Young's modulus with increase in clay content described by the equation Ei = 68.38 – 0.52Clay. Clay content here is the summation of illite, kaolinite, smectite, chlorite and mixed clays.

Figure 68 shows a plot of Young's modulus versus TOC which shows decrease in Young's modulus as TOC increases. The linear trendline for TOC ignores points which had TOC less than 2 wt% and Young's modulus greater than 60 GPa. This was done because rocks having low TOC do not produce commercial hydrocarbons. We have also found that rocks having large Young's modulus were mostly rich in carbonates and contained low TOC.

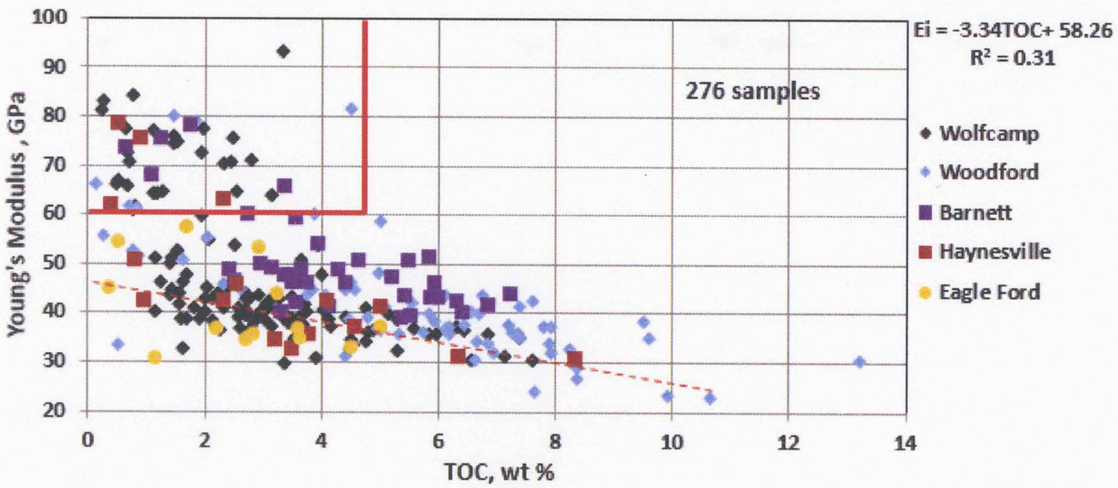

Figure 68: Young's modulus versus TOC for all shales studied. There is a decreasing trend in Young's modulus with increase in TOC described by the equation Ei = 58.26 – 3.34TOC. Trendline ignores points with TOC < 2 wt% and Ei > 60 GPa. Low value of R^2 indicates a weak correlation. There is lesser scatter in the data at higher TOC values.

Organic matter in a rock contains pores (Sondergeld et al., 2010). Some less matured organics may lack such pores (Curtis et al., 2012). Hence increase in organic content should make the rock weaker. Marz et al., (1983) have studied the effect of changes in organic content in shales on the compressional and shear wave velocities. They observed that with increase in organic content both V_P and V_S decrease but the sensitivity of V_P was much greater than V_S. Eseme et al., (2007) in their paper on review of mechanical properties of oil shales have presented the change in Young's modulus of shale with change in organic content and have found it to decrease as organic content increases.

Quartz, carbonate, pyrites, anhydrite and feldspars are hard components in the shales. Since concentration of the latter three was very low, they were ignored from the analysis. Figure 69 shows a plot of Young's modulus versus quartz+carbonate (QC).

There is an overall positive trend showing increase in Young's modulus as quartz and carbonate content in the shale increases.

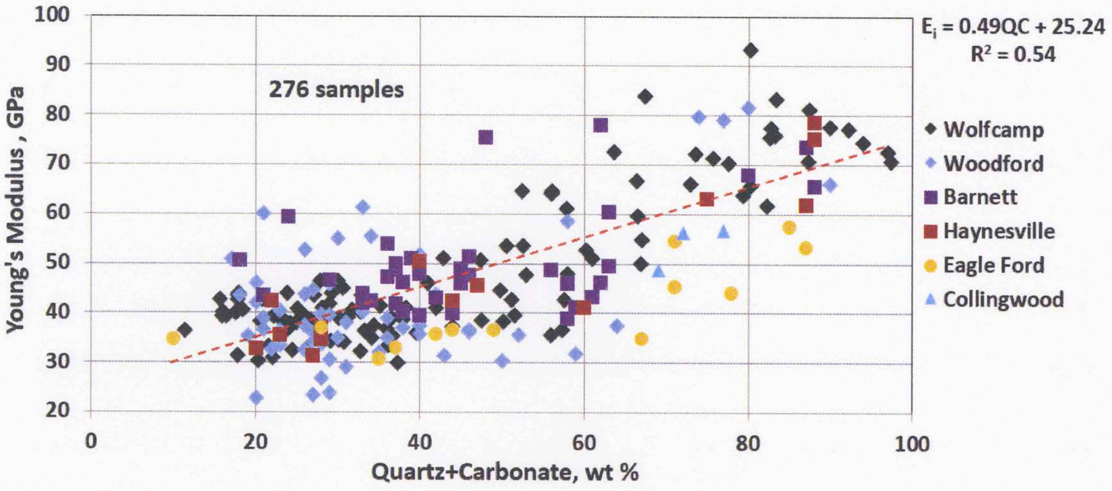

Figure 69: Young's modulus versus quartz+carbonate (QC) for all shales studied. There is an increasing trend in Young's modulus with increase in quartz+carbonate described by the equation Ei = 25.25 – 0.49QC.

Based on the data for compositional dependence of Young's modulus, it can be seen that even though a linear trendline is used for describing the behavior for all points, it is clear that for quartz+carbonate less than 40 wt%, Young's modulus varies within the range of 30 to 45 GPa, beyond which it starts to increase. A similar observation was made for clays where it can be seen that for clay concentration more than 40 wt% the Young's modulus lies between 30 and 45 GPa. It was also observed that the scatter in Young's modulus was less for porosity more than 6% and TOC more than 4 wt%. Plots presented in Appendix A are presented to separately view sample points more than 45 GPa and less than 45 GPa. It was observed that good agreement was found between measured petrophysical parameters and Young's modulus for Ei > 45 GPa. While hardly any correlation was observed for points where Ei < 45 GPa. These were also the samples where the clay content was more than 40 wt%.

All shales require hydraulic fracturing during which proppants are pumped in the fractures to keep the fracture open and maintain permeability. But under the influence of closure pressure these proppants can get embedded in the shale leading to a reduction in permeability. Experimental studies by Rongzun et al. (1987), and Sone and Zoback, (2010), have concluded that clay rich shales show creep deformation. Long soaking times during hydraulic fracturing make the rock even weaker and increase the chances of proppant embedment (Guo and Liu, 2012 and Akrad et al., 2011). Proppant embedment models by Guo and Liu, (2012) indicate that embedment also depends on Young's modulus. They have also studied embedment characteristics in various shales which indicates that more siliceous shales like Barnett which are characterized by higher Young's modulus and low in-situ stress show gradual embedment. Akrad et al, (2011), studied Bakken, Barnett, Eagle Ford and Haynesville shales using nanoindentation after exposing them to fracturing fluids at 300°F for 48 hours and recorded significant drop in Young's modulus.

Measurement of sample hardness is another way to determine embedment characteristics of a shale. Figure 70 shows a plot of horizontal indentation hardness (H_i) versus horizontal Young's modulus (E_i) for all the shales studied. This plot shows that hardness and Young's modulus are directly proportional.

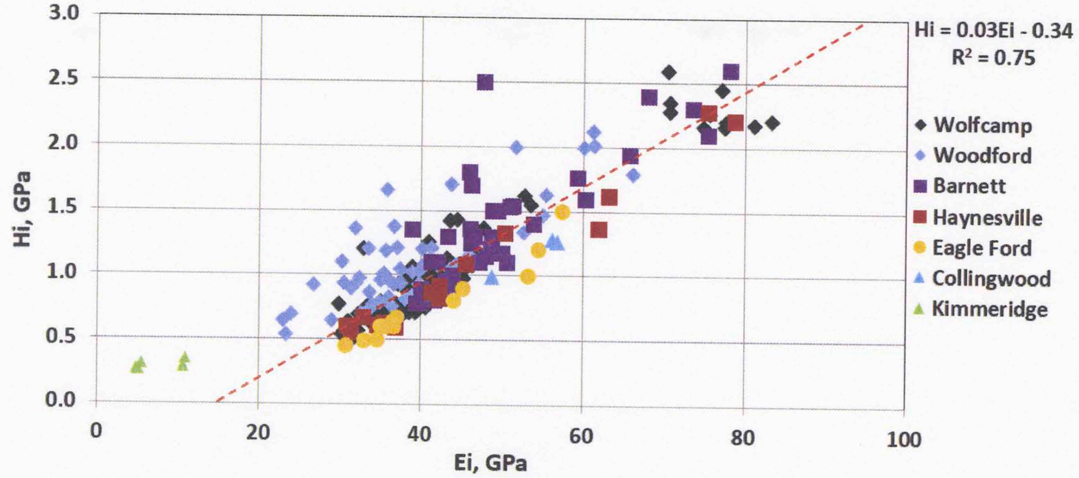

Figure 70: Horizontal Young's modulus, E_i, versus horizontal indentation hardness, H_i, for all shale samples tested except Kimmeridge. High carbonate points from Wolfcamp shale were outliers and were ignored. Plot shows a direct relationship between E_i and H_i described by the equation $H_i = 0.03E_i - 0.34$.

Porosity, TOC and mineralogy are also related to hardness. Plot of H_i versus porosity shows a negative trend similar to E_i versus porosity (Figure 71). Plot of H_i versus clay content also showed a negative trend (Figure 72). Correlation between TOC and hardness was negative (Figure 73). Plot of H_i versus quartz+carbonate showed and increasing trend (Figure 74).

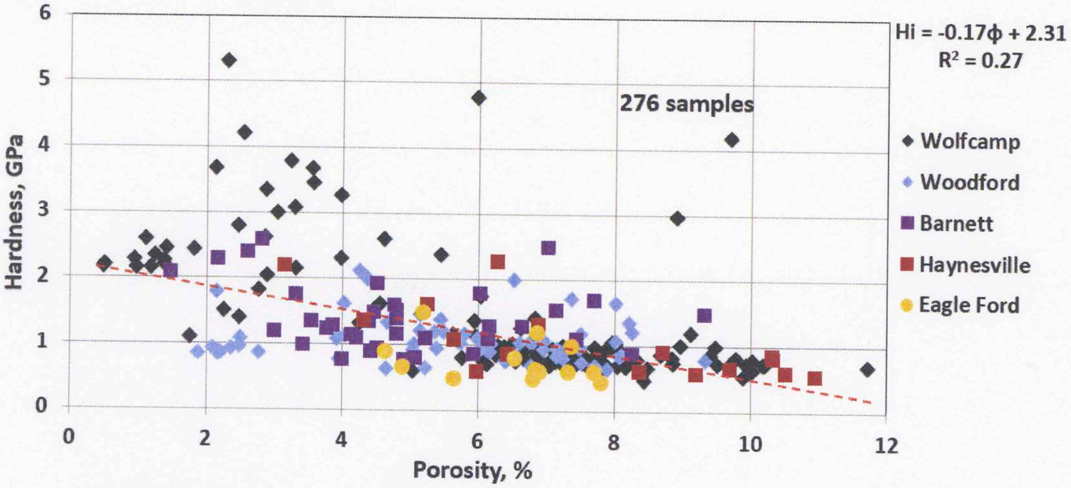

Figure 71: Horizontal indentation hardness versus porosity for different shales. There is a decreasing trend in hardness with increase in porosity described by the linear equation $Hi = 2.31 - 0.17\varphi$. Less scatter in the data is observed at higher porosity.

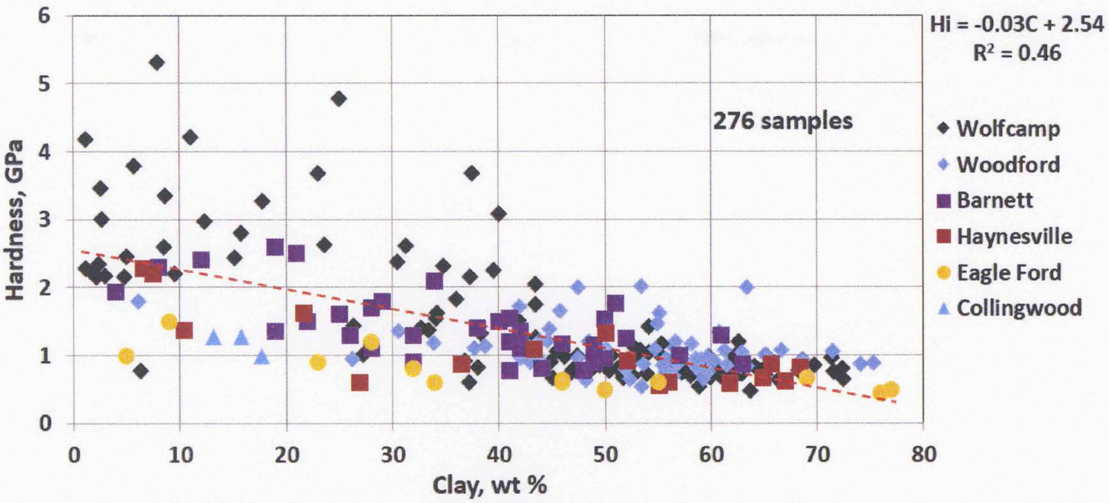

Figure 72: Horizontal indentation hardness versus clay content for all the shales studied. There is a decreasing trend in Young's modulus with increase in clay content described by the equation Hi = 2.54 – 0.03Clay. Clay content here is the summation of illite, kaolinite, smectite, chlorite and mixed clays.

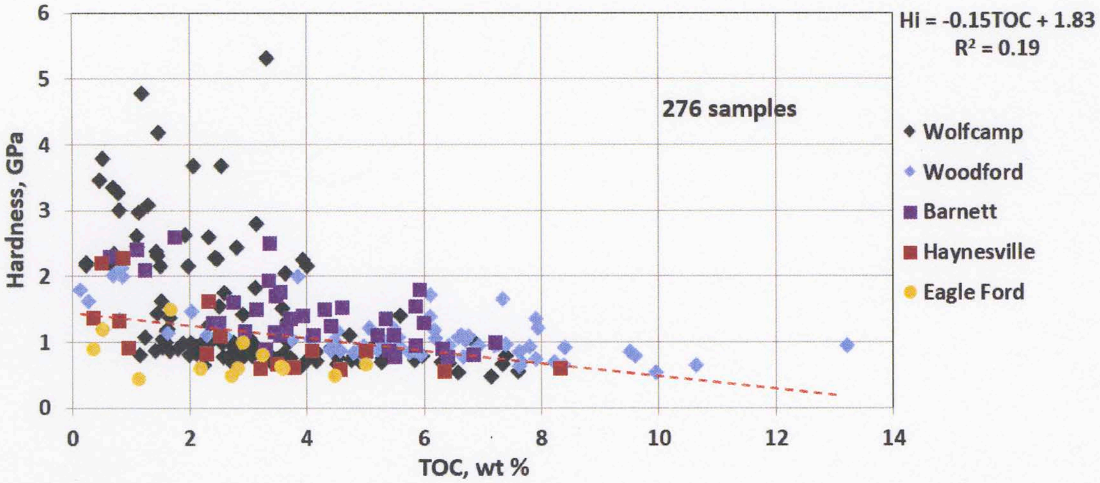

Figure 73: Horizontal indentation hardness versus TOC for all shales studied. There is a decreasing trend in Young's modulus with increase in TOC described by the equation Hi = 1.83 – 0.15TOC. Trendline ignores points with TOC < 2 wt% and H_i > 2 GPa. Low value of R^2 indicates a weak correlation. There is less scatter in the data at higher TOC values.

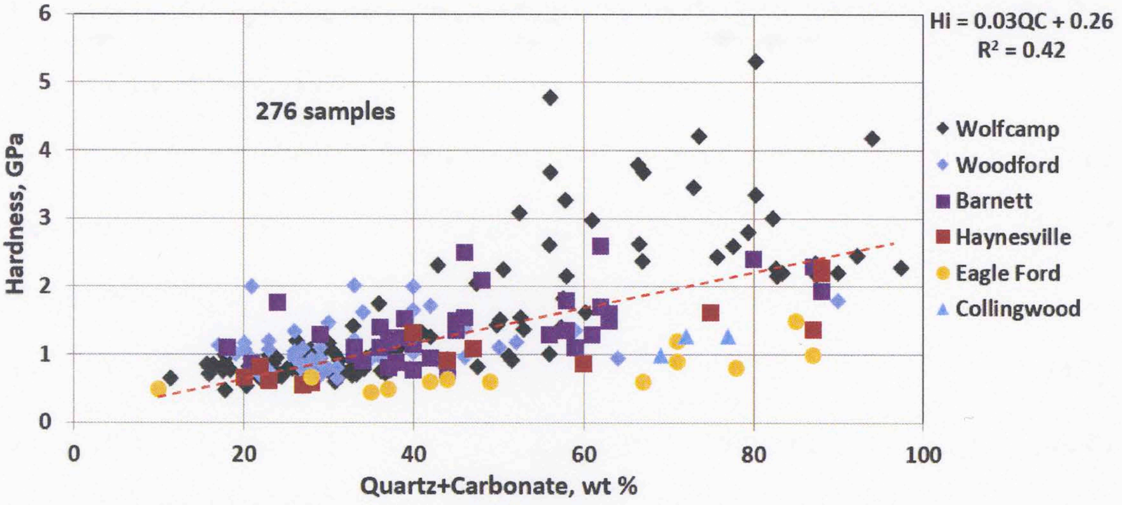

Figure 74: Horizontal indentation hardness versus quartz+carbonate (QC) for all shales studied. There is an increasing trend in Young's modulus with increase in quartz+carbonate described by the equation $H_i = 0.26 - 0.03QC$. Less scatter in the data was observed at low QC concentration.

Dependence of Young's modulus and hardness on petrophysical parameters was presented in the figures above. This study indicates that porosity, TOC, clay content and quartz+carbonate are the primary parameters controlling the variation in Young's modulus and hardness. These parameters were used for a multivariate regression analysis to predict Young's modulus and hardness. Other minerals were present in trace amounts but are ignored in this analysis. One sample point from Well#2 having high concentration of pyrites was ignored. Carbonate rich sections at the base of Well#1 were also ignored. Based on the measured parameters, regression equations were generated (based on data for 248 samples) for calculating E_i and H_i from the knowledge of TOC, porosity and mineralogy.

$$E_i = 71 - 2.14 * \varphi - 1.18 * TOC - 0.24 * Clay + 0.05 * QC \quad \ldots\ldots\ldots\ldots\ldots\ldots\ldots\ldots \text{(4.1)}$$

$$H_i = 3.34 - 0.08 * \varphi - 0.04 * TOC - 0.03 * Clay + 0.005 * QC \quad \ldots\ldots\ldots\ldots\ldots\ldots \text{(4.2)}$$

where, porosity is in vol% and TOC, clay and QC are in wt%, and E_i and H_i are in GPa.

Low values of F-significance were observed for both the equations which indicates that regression analysis is good.

Multivariate regression analysis was also carried out for Wolfcamp shale since adequate data was available from the study of three wells. The corresponding equations generated are presented below

$$E_i = 69 - 1.60 * \varphi - 2.13 * TOC - 0.24 * Clay + 0.11 * QC \ldots\ldots\ldots\ldots (4.3)$$

$$H_i = 3.53 - 0.04 * \varphi - 0.13 * TOC - 0.03 * Clay + 0.002 * QC \ldots\ldots\ldots\ldots (4.4)$$

Low values of F-significance was observed for these equations as well.

All trend lines and corresponding regression equations presented in this section for all the shales were also generated for individual shales for which sufficient data was available. While the nature of trends remained the same, the resultant regression equations were different. The resulting correlation matrix between the various parameters measured for all shales combined is presented in Table 8.

Table 8: Correlation matrix for parameters measured on all shales.

	Porosity	Clay	QC	TOC	Ei	Hi
Porosity	1					
Clay	0.39	1				
QC	-0.42	-0.94	1			
TOC	0.22	0.08	-0.22	1		
Ei	-0.66	-0.60	0.66	-0.55	1	
Hi	-0.51	-0.65	0.65	-0.33	0.79	1

4.7 Voigt-Reuss-Hill Averaging

Voigt-Reuss-Hill (VRH) averaging was used to calculate the theoretical Young's modulus. Knowing the rock composition from the petrophysical measurements and the theoretical Young's modulus and densities of each mineral (Mavko et al., 2003), VRH averaged Young's modulus was calculated. Young's modulus for each mineral was calculated based measured velocities. Density of organics was taken as 1.3 g/cc (Mavko et al., 2003) and the Young's modulus was taken as 7.8 GPa, which is the average of measured Ei of organics in this study. Porosity was accounted using the expression in equation 4.5 (Luo and Stevens, 1998).

$$\mathrm{E} = \mathrm{E_o}(1 - 3.3\varphi + 3.54\varphi^2) \quad (4.5)$$

where, E and E_o are the VRH averaged Young's modulus with and without porosity respectively.

The methodology for calculating the VRH averages is discussed by Mavko et al., (2003).

Voigt upper bound of the effective elastic modulus and n phases is given by

$$E_V = \sum_i^n \mathrm{f_i E_i} \quad (4.6)$$

where, f_i is the volume fraction.

Reuss lower bound of the effective elastic modulus and n phases is given by

$$E_R = \sum_i^n \mathrm{f_i / E_i} \quad (4.7)$$

E_{VRH} is given as the arithmetic average of lower and upper bounds

$$E_{VRH} = {}^{(\mathrm{E_V} + \mathrm{E_R})}/_{2} \quad (4.8)$$

Figure 75 presents a crossplot of the calculated E_{VRH} and horizontal E_i for 180 samples from all the shales studied. VRH averages are applicable to anisotropic samples which are randomly oriented. But minerals in shales are preferentially oriented. It is seen that most of the E_{VRH} calculated lie above the 1:1 (shown in black) indicating that E_{VRH} is more than measured horizontal E_i. There is a wide variability in the Young's modulus of organics, clays and other minerals like apatite and pyrites which affect the calculated VRH averages. Katahara et al., (1996) have reported different V_P and V_S for illite and kaolinite than Mavko et al., (2003). Prasad et al, (2005) (from Wang et al., 2001; and Katahara, 1996) reported Young's modulus of kaolinite to vary between 13 to 80 GPa. When Young's modulus of clays was decreased by a factor of 20% it was observed that the data points approach closer to the 1:1 line. Given the current understanding about the elastic modulus of clays and other lesser studied minerals, VRH technique does not seem to work for this dataset.

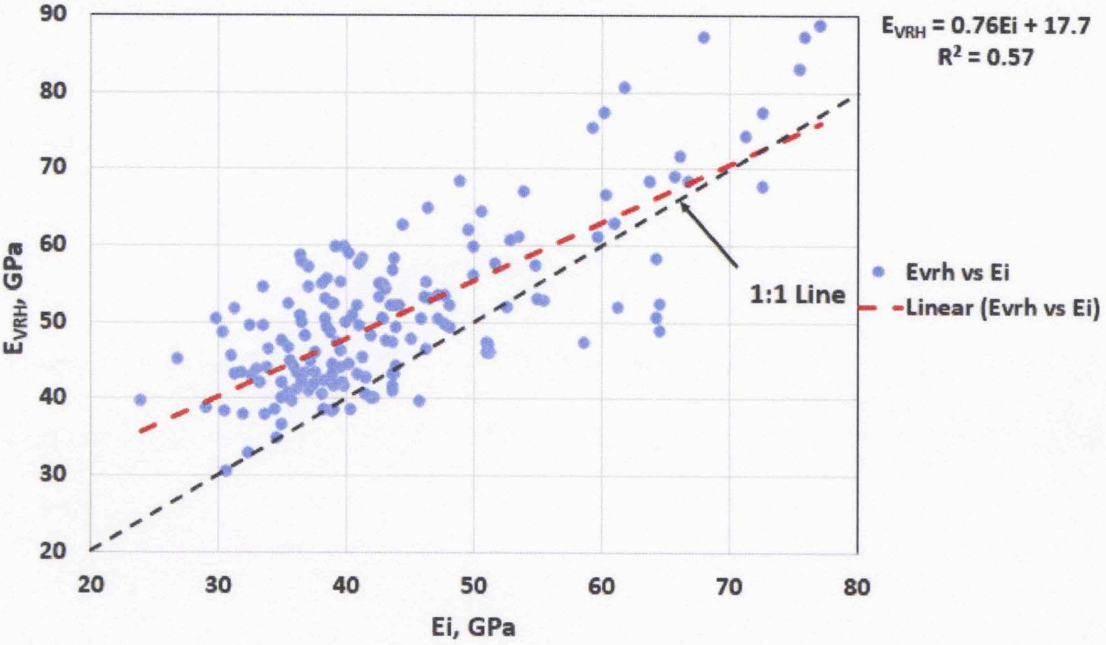

Figure 75: Plot of VRH averaged and horizontal indentation Young's modulus. The linear trendline equation for this dataset is given by E_{VRH}=0.76E_i+17.7. Black line is the 1:1 line. Most of the point lie above this line indicating that E_{VRH} is greater than horizontal E_i.

4.8 Young's Modulus Anisotropy

"Understanding the anisotropy of the Young's modulus and Poisson's ratio of shales is important for determining the variation in minimum horizontal stress with depth and for designing hydraulic fractures required for economic production from low-permeability gas shale reservoirs", Sayers (2010). Elastic anisotropy of shales is due to many factors. Presence of clays with preferred orientation makes shales anisotropic (Jones and Wang, 1981; Hornby, 1998). Presence of organic content also imparts anisotropy to shales (Vernik and Landis, 1996). Results from this study also indicate that samples which have higher clay and organic contents tend to be more anisotropic. This was also indicated by the data from the shale section in Well#1 and Well#2 which are clay rich. We found a larger Young's modulus anisotropy factor (E_H/E_V) of 1.64 in Well#1 and 1.65 in Well#2. Samples rich in quartz and carbonate tend to show lesser anisotropy. Assumption of anisotropy can lead to serious errors in time to depth conversion (Banik, 1984) which could lead to drilling dry holes (Sondergeld et al., 2000). Velocity anisotropy could lead to errors in estimating fracture height and underestimation of fracture lengths during microseismic mapping of hydraulic fractures (Castano et al., 2010).

Young's modulus was measured both parallel and perpendicular to the bedding in samples from Well#1 and Well#2. Anisotropy was calculated using the following expression

$$\varepsilon = \frac{E_{iH}-E_{iV}}{2E_{iV}} \quad \text{..........} \quad (4.9)$$

Sondergeld et al., (2000), and Kumar, (2012a) have also measured Young's modulus anisotropy on core plugs and plotted it against TOC (Figure 76). In the study by Sondergeld et al., (2000), on Kimmeridge shale, the value of ε was between 0 to 0.8 with majority of the points lying in between 0.2 and 0.4. They found an increasing trend between ε and TOC. Due to high organic content in Kimmeridge shale (~28 wt%), organics are present as a continuous phase and contribute towards anisotropy. Results by Kumar, (2012a) on Barnett shale indicate no relation between ε and TOC but there was an increasing trend when plotted against clay content. This may be because organics are randomly distributed in shales and are isolated from each other. Whereas in the study by Sondergeld et al, (2000), studies were performed using dynamic data on core plugs which capture of the composite effect for the sample. Clays have preferred orientation and are present as a continuous phase making the shale anisotropic.

Results from this study indicate that ε lies in the range from 0 to 1.4 (Figure 77) with most of the measurements lying between 0.1 and 0.5; average value of ε was 0.32. Results from this study do not indicate any relationship between ε and TOC.

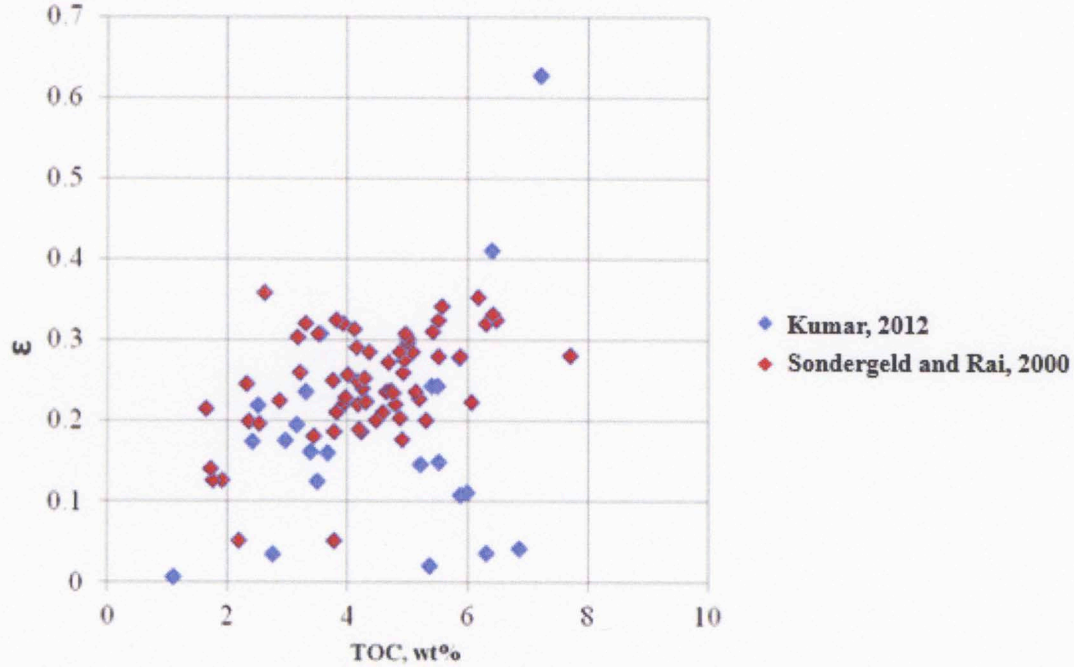

Figure 76: Anisotropy parameter versus TOC by Sondergeld et al., 2000, for Kimmeridge shale (red); and by Kumar, (2012a), for Barnett shale (blue). Increasing trend in ε was observed with increase in TOC for Kimmeridge shale while results on Barnett shale do not show any dependence.

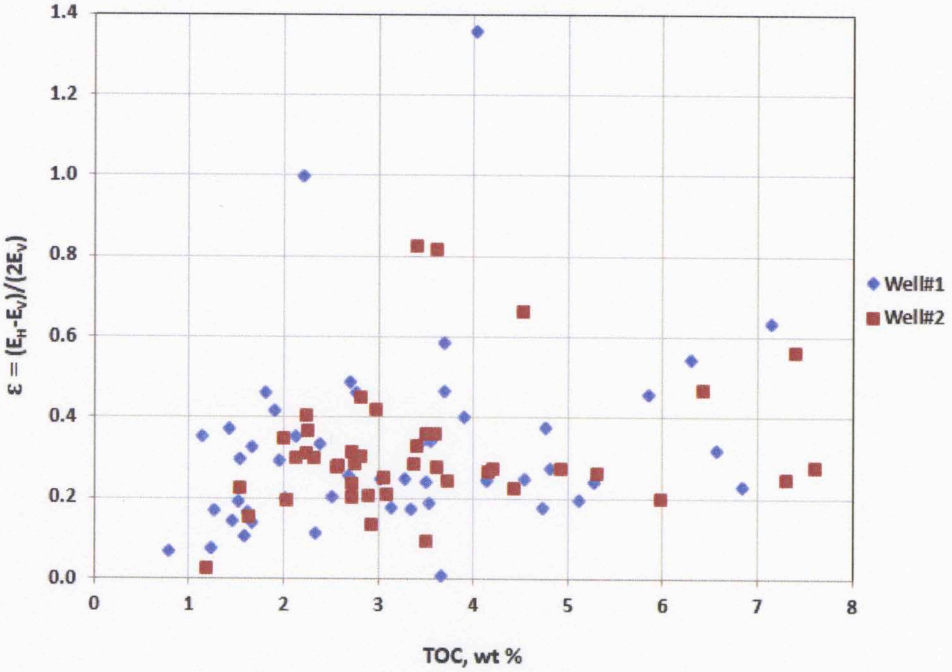

Figure 77: Anisotropy parameter versus TOC for Well#1 and Well#2 in Wolfcamp shale. Both sets of samples were clay rich. No specific trend is noticed between ε and TOC. The average value of ε was found to be 0.32.

4.9 Static and Dynamic Young's Modulus

Dynamic moduli can be calculated from measured compressional and shear wave velocities and density. Owing to the heterogeneous nature of shales, the properties can change within a few inches. Therefore, core plugs were taken from the same depths and adjacent to pieces used for nanoindentation, porosity, TOC and mineralogy. Acoustic P and S wave velocities were measured for Woodford, Haynesville (Gupta, 2012), Kimmeridge (Sarkar, 2008) and Wolfcamp shales. One P-wave and two shear wave (S1 and S2) velocities were measured. The faster of the two shear wave velocities was used since it represents the earliest arrival and should reflect mineralogy. Measurements were done at a range of confining pressures from 250 to 5000 psi. Dynamic Young's modulus, E_d was calculated using densities and velocities. As previously discussed, nanoindentation data was generated for all the shales. Table 9 lists the number of samples from each shale for which nanoindentation and dynamic data were available. Gupta, (2012) has shown that pressure dependence of velocities in Woodford shale was minimal between 250 and 5000 psi. Kumar, (2012a) extended this result to compare nanoindentation results with dynamic Young's modulus at 250 psi, assuming no significant change in Young's modulus from 250 psi to atmospheric pressure. For this study, results from nanoindentation and on native state core plugs were compared at 250 and 5000 psi. It was observed that match between the two datasets was much better at 5000 psi. This could be explained by the fact that at 250 psi confining pressure all the cracks inside the sample do not close while at 5000 psi we can expect most of the cracks to be closed. In the same way, due to its small depth of investigation is not sensitive to all the cracks that may be present inside the sample. Figure 78 presents the cross plot of 149 shale samples from Wolfcamp, Woodford, Haynesville and Kimmeridge shales. We see an almost 1:1 match between the two datasets with an R^2 value of 0.94.

Table 9: List of number of samples from all shales on which nanoindentation and dynamic data were measured.

Shale	Nanoindentation Data	Dynamic Data
Wolfcamp	134	77
Woodford	69	53
Kimmeridge	5	5
Haynesville	16	14
Total	276	149

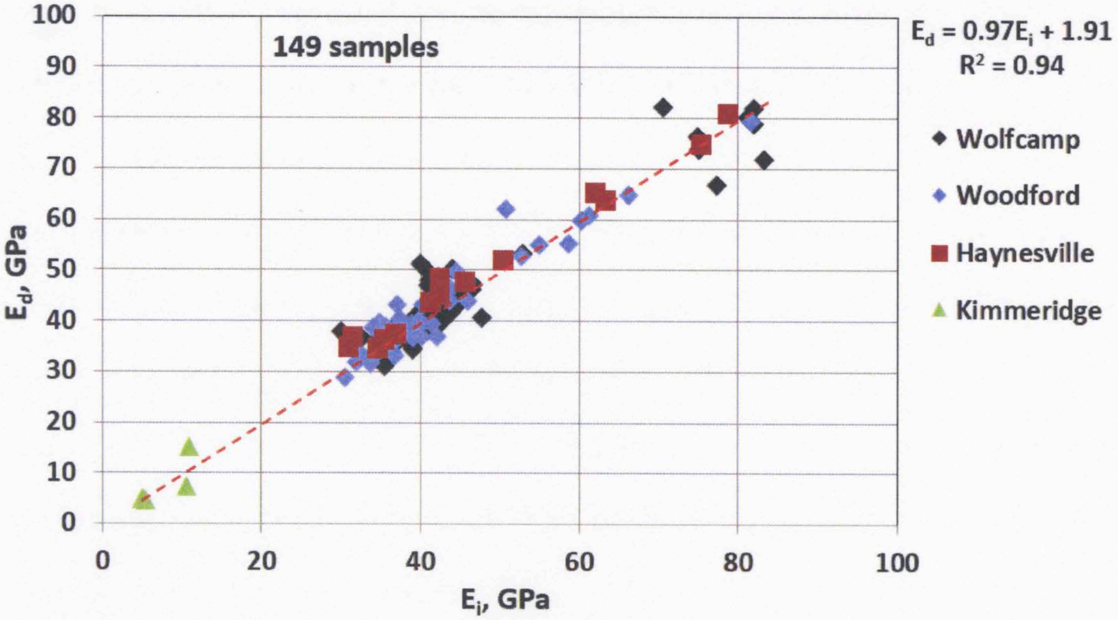

Figure 78: Comparison of nanoindentation (E_i) and dynamic (E_d) Young's modulus for 149 samples from Wolfcamp, Woodford, Haynesville and Kimmeridge shales. Good agreement was observed between the two datasets.

4.10 Nanoindentation on Shales at Elevated Temperatures

Reservoir rocks are present several thousand feet below the surface where temperatures are elevated; this affects the mechanical properties of rocks. Moreover, tertiary recovery methods like steam flooding and in-situ combustion also heat the rock to high temperatures. Knowledge of the mechanical properties under the influence of temperature is therefore useful. Most substances tend to become weaker under the influence of temperature. Moustafa et al, (2008) have presented results of triaxial testing on Tournemire shale (~50% clays, 11% pyrite) in France, at temperatures ranging from 20 to 250°C. They found Young's modulus to decrease in both vertical and horizontal directions with increase in temperature. Lempp et al., (1994) studied behavior of Posidonia shales from Germany for the effect of temperature on mechanical properties using triaxial compression tests. They used temperatures from room temperature to 300 °C. They observed very strong temperature dependence of shale mechanical properties.

Marz et al., (1983) measured V_P and V_S through shale core plugs as a function of temperature from room temperature to 480°C and found both V_P and V_S to be decreasing with increasing temperature.

Nanoindentation at elevated temperatures was performed in the same manner as explained in Chapter 3. Additionally tip calibrations were performed for all the temperatures at which measurements are to be made. This is done to capture changes in frame stiffness that happen at a result of change in temperature. Schuh et al., (2006) have discussed the technical issues with nanoindentation at elevated temperatures. They have discussed their nanoindentation results on fused silica performed between 23 and 405°C. These measurements were verified with other independent mechanical test data. They have demonstrated that the effect of temperature on the indenter tip area function is negligible. In this study, 20 horizontal samples from Well#1 were tested at 100°C. This temperature was selected based on the bottomhole temperature in Well#1. Dilation of 20 to 40 μm was observed as an increase in the height of sample using the nanoindenter optical microscope. This proved that the sample underwent expansion due to heating. Figure 79 shows a plot of vertical modulus, horizontal modulus at room temperature, and horizontal modulus at 100°C. According to these results, there is not a significant change in horizontal Young's modulus at different temperatures. It was found to be slightly lower or higher than the previous measurements at room temperature. For these measurements, it was observed that there was an average increase in Young's modulus by 0.1%. This contradicts the results from previous researchers who found Young's modulus to be decreasing with increase in temperature.

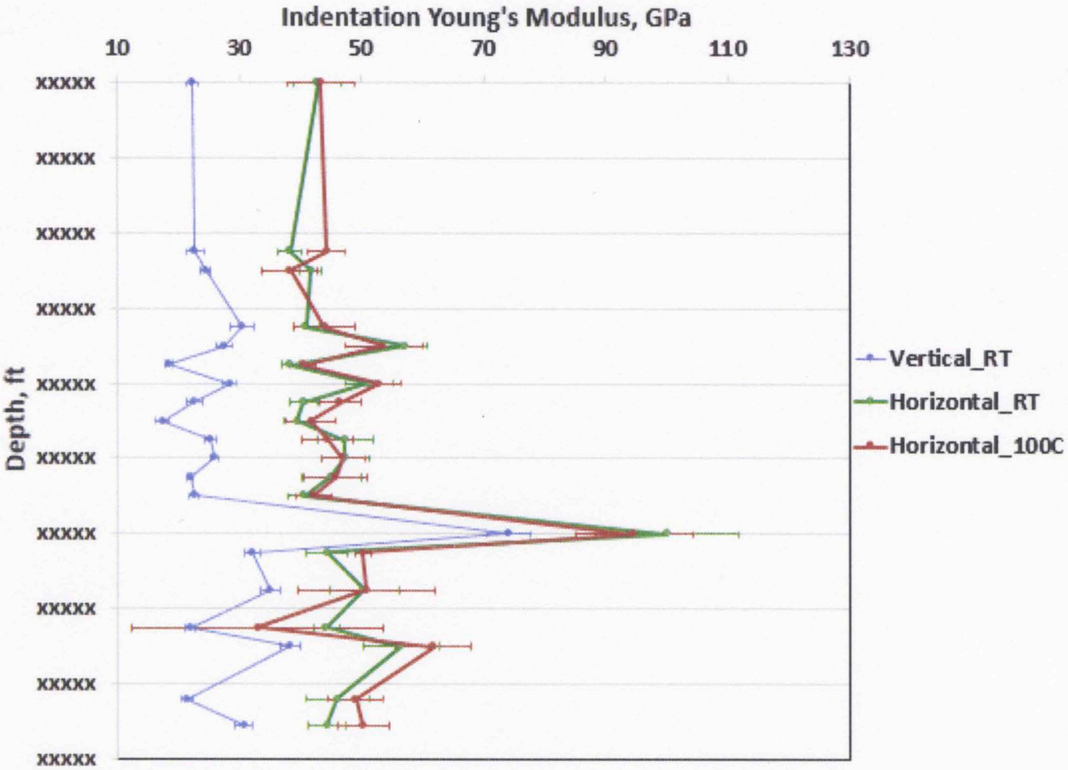

Figure 79: Comparison of nanoindentation Young's modulus for vertical and horizontal samples from Well#1 with horizontal Young's modulus at 100°C. We observe both increase as well as decrease in the Young's modulus.

An experiment was designed in which nanoindentation was performed at room temperature as well as 100°C on the same sample and this was followed by and SEM imaging/EDS study to confirm the density contrast and elemental concentration in the sample. Two samples from Well#1 were selected for this analysis: sample 1 (53 wt% clays, 7 wt% carbonates, and 31 wt% quartz) and sample 2 (47 wt% clays, 13 wt% carbonates, and 22 wt% quartz). Following figures present the SEM and EDS images for these samples and present the measured Young's modulus for each indentation. Results of only a single array of 25 indentations are presented to explain the temperature dependence of Young's modulus.

Sample 1

Mineralogy data from sample 1 shows that it is rich in clay. The only clay minerals found in the sample were illite (33 wt%) and mixed clays (20 wt%). Carbonates were present primarily in the form of siderite (6 wt%). Sample porosity, TOC and grain density were 4.4 %, 4.7 wt% and 2.52 g/cc, respectively. Figure 80 presents the BSE image of 25 indentations on sample 1 and the corresponding Young's moduli at room temperature. We observe that the average Young's modulus for this sample is 51±4 GPa. Figure 81 presents the EDS map for the same array. Bright crystals shown in the image were found to be iron pyrite using EDS. This was confirmed by the presence of iron and sulfur at those spots.

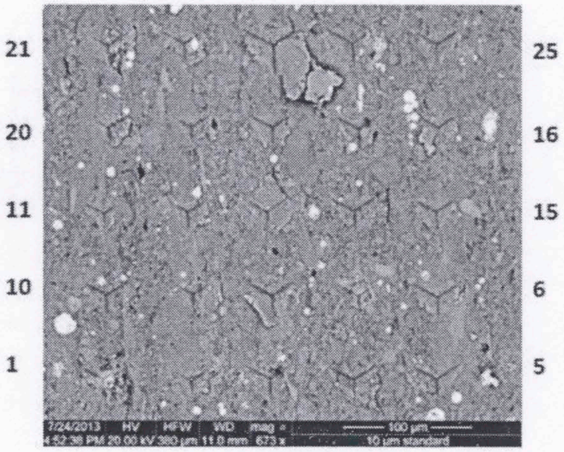

No.	Young's Moduli					No.
21	53	48	45	44	49	25
20	53	57	54	49	52	16
11	59	50	42	50	51	15
10	54	58	52	38	50	6
1	48	63	52	52	50	5

Figure 80: BSE image of sample 1 showing an array of 25 indentations numbered from 1 to 25. Array begins from the bottom left. Average indentation Young's modulus was found to be 51±4 GPa at room temperature.

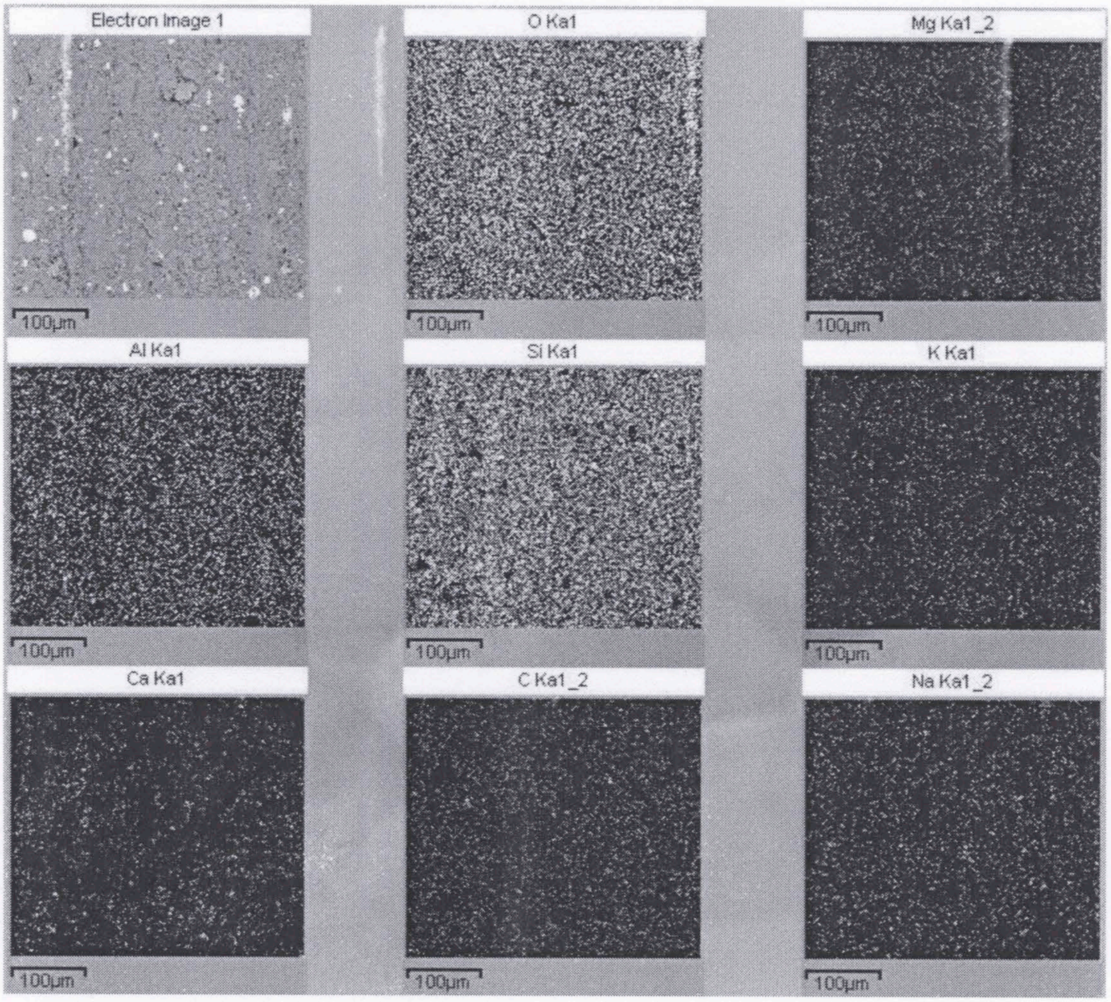

Figure 81: EDS image for the array of 25 indentations at room temperature showing elemental compositions for the commonly found elements. All elements appear to be uniformly distributed in the sample.

Figure 82 presents the BSE image of 25 indentations on sample 1 and the corresponding Young's moduli at 100^{o}C. We observe that the average Young's modulus for this sample is 43±3 GPa. This is a 16% decrease from the Young's modulus measured at room temperature. Figure 83 presents the EDS map for the same array showing elemental compositions. Most elements were uniformly present except for a few points where calcium was present instead of silicon.

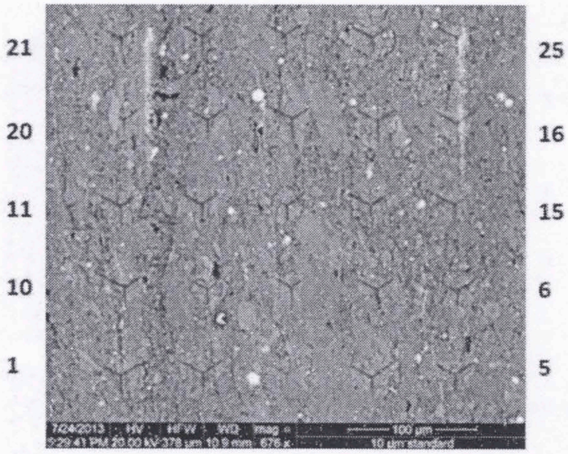

21	48	45	42	46	45	25
20	42	45	42	46	48	16
11	46	45	38	39	42	15
10	45	36	50	47	43	6
1	42	40	33	40	46	5
No.	Young's Moduli					No.

Figure 82: BSE image of sample 1 showing an array of 25 indentations numbered from 1 to 25. Array begins from the bottom left. Average indentation Young's modulus was found to be 43±3 GPa at 100 °C.

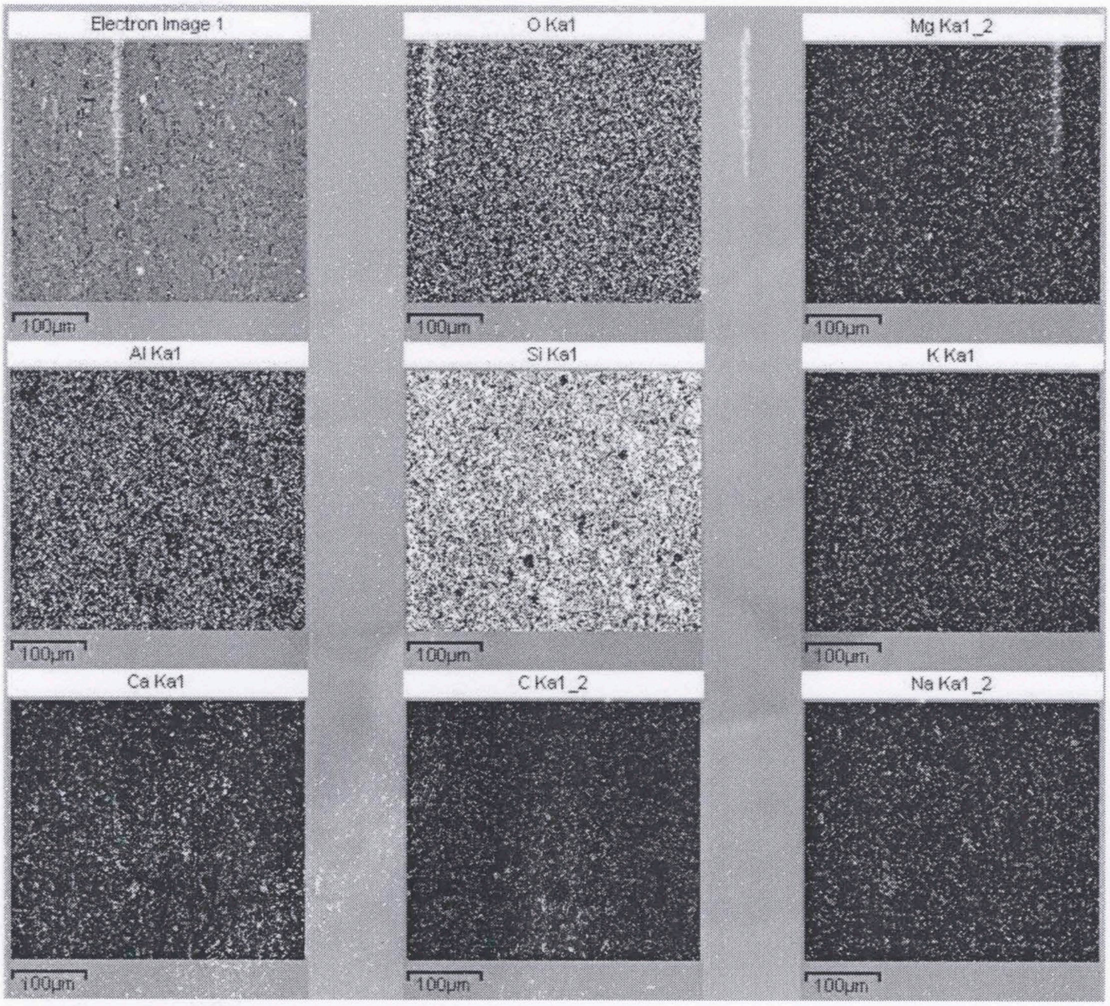

Figure 83: EDS image for the array of 25 indentations at 100 °C showing elemental compositions for the commonly found elements. All elements appear to be uniformly distributed in the sample except for a few points where slight dominance of calcium was observed.

Sample 2

Mineralogy for sample 2 resembles that of sample 1 as mentioned above. Only clay minerals found in the sample were illite (39 wt%) and mixed clays (8 wt%). Carbonates present are mainly calcite (11 wt%). Sample porosity, TOC and grain density were 7.2 %, 2.7 wt% and 2.54 g/cc, respectively. Figure 84 presents the BSE image of 25 indentations on sample 1 and the corresponding Young's moduli at room temperature. We observe that the average Young's modulus for this sample is 50±4 GPa. Figure 85 presents the EDS map for the same array showing elemental compositions. We observe that the presence of Calcium (Ca) which indicates carbonates is marked by absence of Aluminum (Al) which denotes clays and Silicon (Si) which denotes quartz. Oxygen was also observed to be present at the same spots as Ca since is calcite is calcium carbonate ($CaCO_3$).

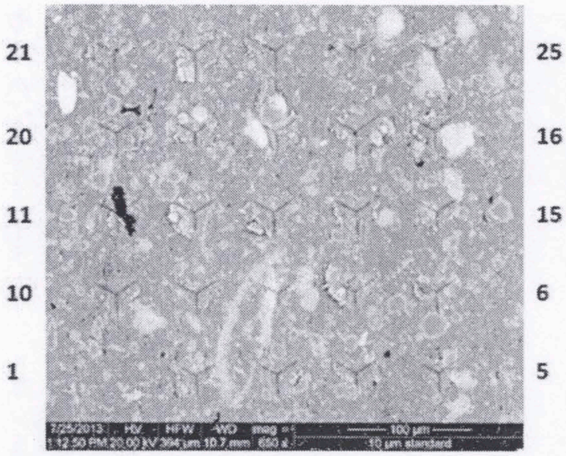

21	46	50	48	46	50	25
20	49	52	45	51	51	16
11	48	55	54	52	51	15
10	51	47	56	53	47	6
1	-	47	53	50	48	5
No.	Young's Moduli					No.

Figure 84: BSE image of sample 1 showing an array of 25 indentations numbered from 1 to 25. Array begins from the bottom left. Average indentation Young's modulus was found to be 50±4 GPa at room temperature.

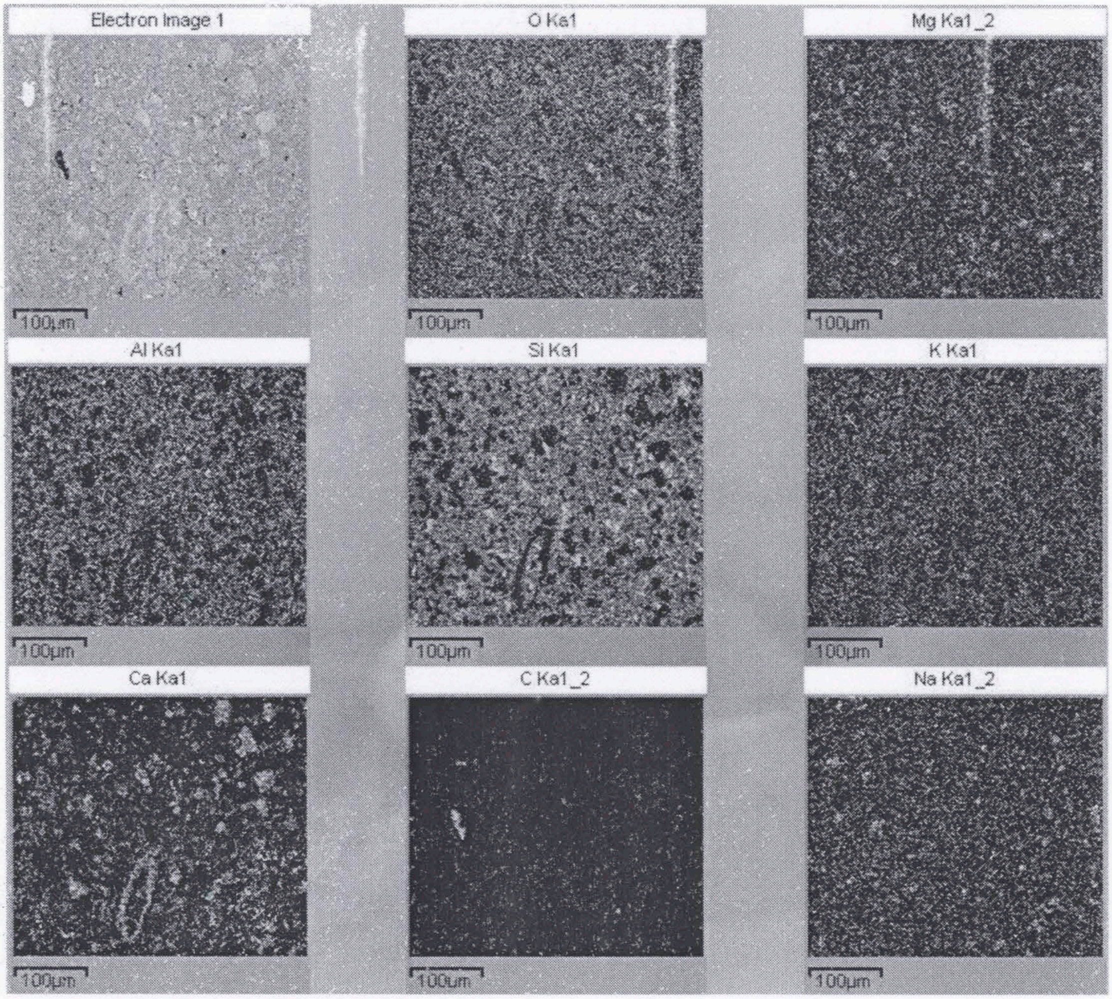

Figure 85: EDS image for the array of 25 indentations at room temperature showing elemental compositions for the commonly found elements. Calcite was present at many places in the sample.

Figure 86 presents the BSE image of 25 indentations on sample 1 and the corresponding Young's moduli at 100°C. We observe that the average Young's modulus for this sample is 52±4 GPa. This is a 4% increase from the Young's modulus measured at room temperature. Figure 87 presents the EDS map for the same array showing elemental compositions. Most elements were uniformly distributed except for a few points where calcium was present instead of silicon.

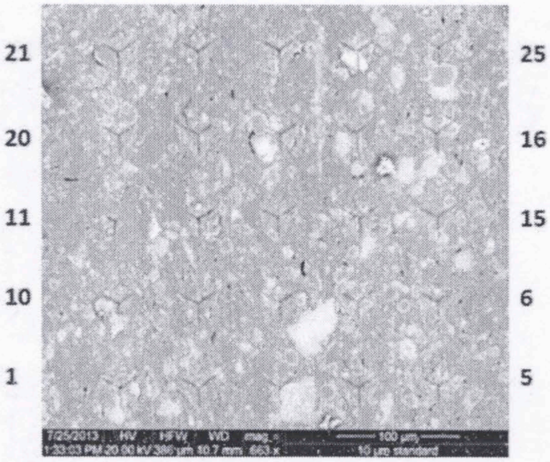

21	53	49	54	46	53	25
20	53	54	50	56	54	16
11	50	51	52	48	56	15
10	51	51	52	51	50	6
1	48	40	57	56	55	5
No.	Young's Moduli					No.

Figure 86: BSE image of sample 1 showing an array of 25 indentations numbered from 1 to 25. Array begins from the bottom left. Average indentation Young's modulus was found to be 52±4 GPa at 100 °C.

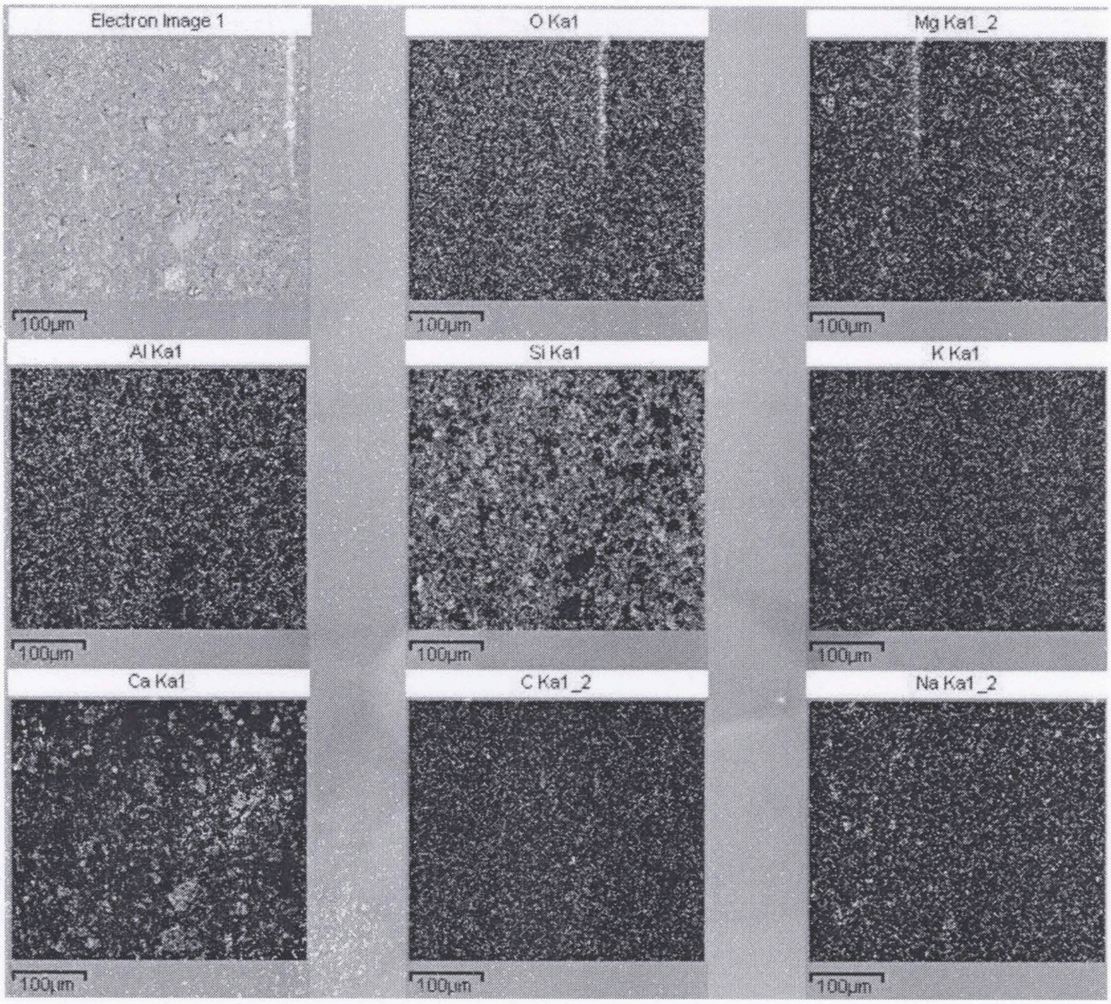

Figure 87: EDS image for the array of 25 indentations showing elemental compositions for the commonly found elements. Calcite was present at many places in the sample as clusters.

Based on the results for the two samples at room temperature and 100°C, it was observed that even though both the samples had similar mineralogy, their temperature response were different. There was drop in Young's modulus in one and a slight rise in the other. In case of sample 1, uniform distribution of minerals was observed throughout the sample and there was very little carbonate presence on the surface of the sample; 16% drop in Young's modulus was observed at 100°C. In case of sample 2 there was variable presence of minerals on the shale surface but many indentations landed in carbonate rich areas. The slight increase in Young's modulus could be due to this. Carbonates have a high Young's modulus and do not seem to be affected by such low temperatures as used in this study. Since temperature affects the Young's modulus of clays at reservoir temperatures, it also becomes clear that for formations rich in clay the problem of proppant embedment will be significant compared to the formations rich in carbonates.

4.11 Nanoindentation on Simulated Drill Cuttings

Coring is an expensive procedure and recovering full sized cores on shales is challenging. Cores are important as they are required for a host of measurements of petrophysical and mechanical properties. Chemical and mechanical instability of some shales makes them hard to recover and measure. On the other hand drill cuttings are generated as a natural byproduct of drilling activity. Encouraging results of nanoindentation on drill cuttings can minimize the dependence of cores and sonic logs for getting Young's modulus. It can also be used as a surrogate for mechanical properties of the rock when no other means is available.

Kumar, (2012a) performed measurements on simulated drilling cuttings for two samples from Barnett shale core samples from 13000 ft depth, and found Young's modulus from cuttings to lie between or very close to vertical and horizontal Young's modulus. Abousleiman et al., (2009) have also carried out measurements on drill cuttings from Woodford shale outcrop (at a depth of 144 ft) and found the Young's modulus for drill cuttings to be 19.5 GPa and that of original sample to be 9.5 GPa. This magnitude of difference is of concern. This could be due to intrusion of epoxy in the samples during sample preparation owing to 15 to 21% porosity in those samples.

Measurement on drill cuttings were performed in two stages during this study. In the first stage measurements were performed at room temperature for simulated drill cuttings from Well#1 (Wolfcamp shale). In the second stage simulated drill cutting samples from Woodford shale were tested at room temperature followed by measurement on the same samples at reservoir temperature (110 ^{o}C).

Sample preparation for both kinds of samples involved crushing a large piece of rock and sieving to obtain smaller pieces of 3 to 5 mm size, which is close to the usual size of drill cuttings. These pieces were subsequently washed in acetone to remove dust and dried. These cuttings were then cast in epoxy and allowed to dry for 24 hours to obtain 1 inch disks. Epoxy used had enough viscosity so it can be used for casting but at the same time not intrude the shale cuttings. Care was taken while mixing epoxy to avoid formation of air bubbles. Sample for room temperature were separately prepared using HFT epoxy (two part epoxy), while samples for high temperature testing were prepared by using a two part epoxy by Master Bond (commercial name: EP42HT-2MED). Each cast contained 12 to 15 pieces of simulated drill cuttings (Figure 88). These samples were subsequently polished using sand papers and ion milled. Following this, the samples were mounted for nanoindentation and 5 to 6 randomly oriented pieces were indented in a 5x5 matrix each. Average of these 125 to 150 measurements was taken as the final Young's modulus for each drill cutting sample.

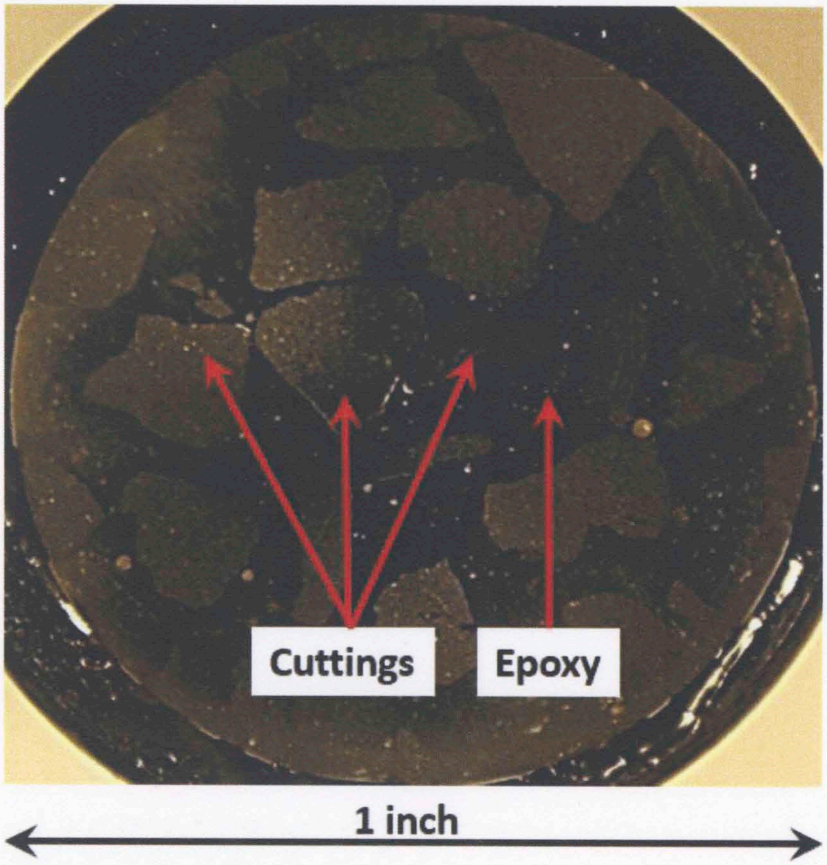

Figure 88: Image of a 1 inch disk of simulated drill cuttings from Well#1 embedded in epoxy and mounted for nanoindentation.

Figure 89 and 90 show a comparison of the results for Young's modulus for whole samples and simulated drill cuttings from Well#1. Error bars are placed for each measurement which indicate 99.999% probability that the average Young's modulus for the sample lies in the range defined by the error bar. Results on Well#1 as shown in Figure 89 indicate that the Young's modulus for simulated drill cuttings lies in between the vertical and horizontal moduli. Results on Woodford shale (Figure 90) show a comparison of horizontal Young's modulus on whole samples at room temperature (red), cuttings at room temperature (blue) and cuttings at high temperature (110 °C) (green).

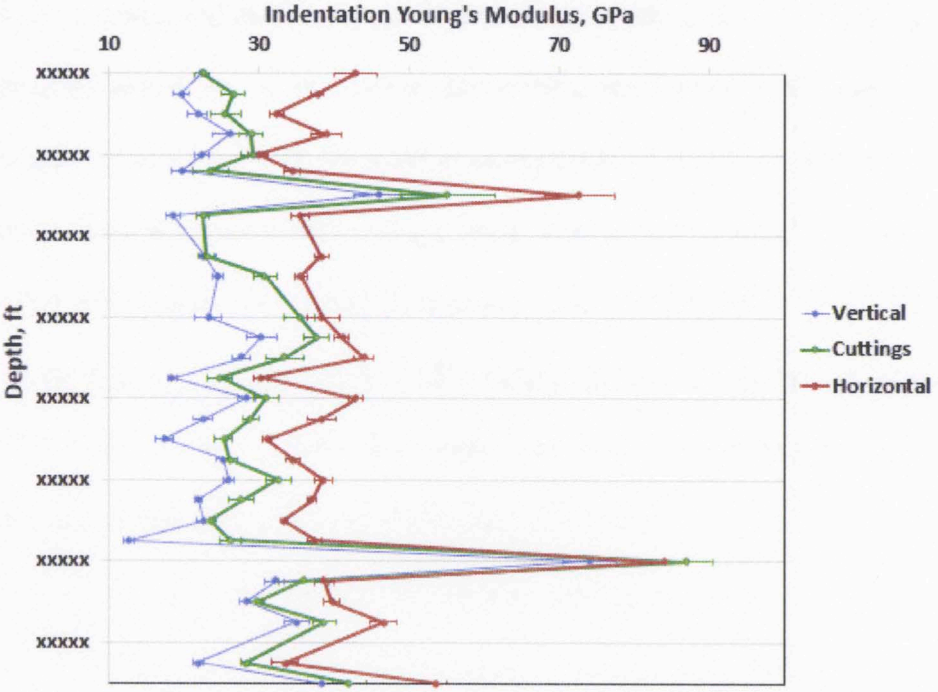

Figure 89: Comparison of vertical and horizontal Young's modulus with measurements on simulated drill cuttings for samples from Well#1 in Wolfcamp shale. Error bars indicate 99.999% confidence intervals.

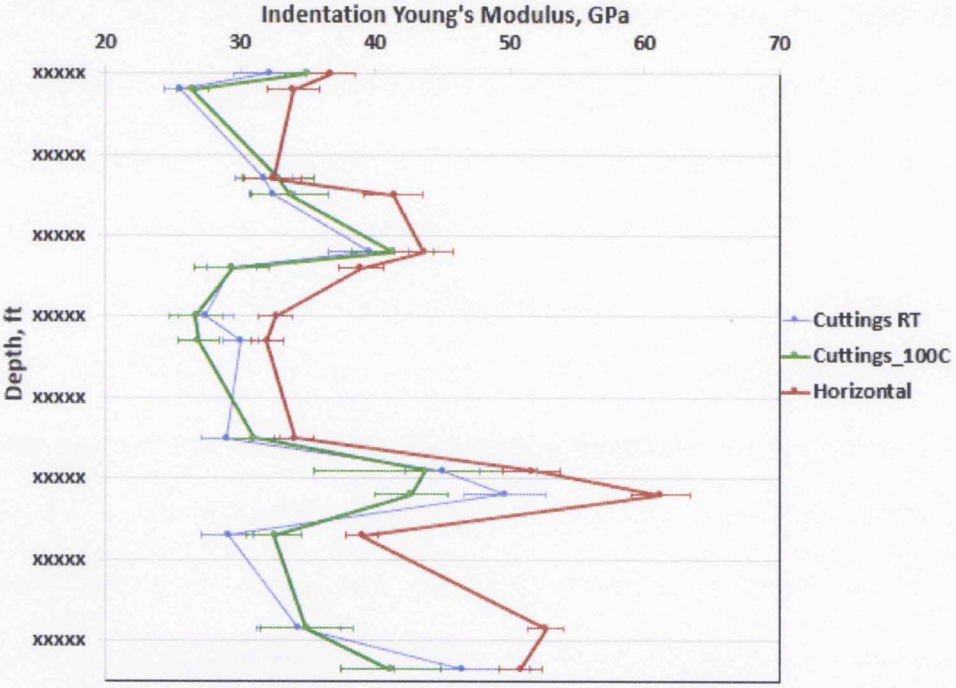

Figure 90: Comparison of results from simulated drill cuttings from a Woodford well at room temperature and 110 °C with horizontal samples. Error bars indicate 99.999% confidence intervals.

Results from simulated drill cuttings at room temperature are encouraging. These measurements were found to lie between the vertical and horizontal Young's modulus. These results suggests that nanoindentation can be a viable technique to obtain Young's modulus of shales when only drill cuttings are available. For drill cutting measurements at elevated temperature and room temperature, an average decrease of 0.3% was observed for Young's modulus while 0.01% drop in indentation hardness was observed at 110 °C. These values indicate that there is no effect of temperature on Young's modulus and hardness at nanoindentation scale.

4.12 Elastic Properties of Organics

Organics are present in varying amounts in shales and affect the mechanical properties at a macroscopic level. Organics can differently affect elastic properties of shales depending on their discrete or continuous distribution in a shale (Sayers, 2013). Small areas of shale surface investigated using nanoindentation often miss the organics which may be randomly scattered. But identification of these organics using SEM can help to study the properties of these organics through nanoindentation. Many previous studies on mechanical properties of organics rely on extraction of organics from rock using acids and solvents. In this process, rock matrix gets dissolved and organics are recovered. Our study also involves use of this method for some specific applications discussed later in this section. But such measurements are affected by changes in organics due to reaction with solvents. This process also removes the organics from their in-situ state in the rock matrix which may affect their properties. Finally casting the recovered organics in the form of a disc destroys organic porosity and may also affect their properties depending on the force used to cast the disc. Nonetheless, there is no other method to get large chunks of organics unless they are recovered in this manner. Subjecting all organics of different maturities to same compaction force could provide a relative idea of their strengths. In-situ organic identified in this study range in size from 10 to 80 μm. In this section we first discuss the results on mechanical properties of organics without dissolving the surrounding matrix, followed by discussions on organics extracted using solvents.

4.12.1 Nanoindentation Results on Undissolved Samples

Nanoindentation and Atomic Force Microscopy (AFM) are the two most widely used techniques to investigate mechanical properties of small organic macerals scattered in the rock. Zeszotarski et al., (2004) and Ahmadov, (2011) have used AFM while Abousleiman et al., (2009) and Kumar et al., (2012c) used nanoindentation for studying organics.

Tests were performed on organic rich samples; 7 samples from Wolfcamp shale and 2 samples from Barnett shale. The procedure followed for identifying organics and for nanoindentation is explained below.

- A hand polished and ion-milled sample is analyzed under SEM in BSE mode to look for low density materials on the rock surface. Figure 91 (a) shows an image of an organic maceral identified in the Woodford shale sample. Here, dark color represents organic while lighter color represents inorganic rock matrix.
- Further confirmation for the presence of organics is done through EDS which identifies organics as portions rich in carbon.
- For easy identification of organics on the optical microscope of the nanoindenter, grooves are created on the sides of organic maceral using focused

ion beam milling in SEM using an FEI 600 Helios instrument. Figure 91 (b) shows 3 grooves created around the organic maceral.

- Indentations are performed in the depth control mode keeping the maximum penetration depth as 500 nm. Organics are very thin and a deep indentation may penetrate through the organics to the underlying rock matrix and affect the measurement. Spacing between indentations was kept as 15-20 μm to avoid interference.
- Samples were imaged under SEM post indentation to confirm indentations whether indentations were in the organic (Figure 92).

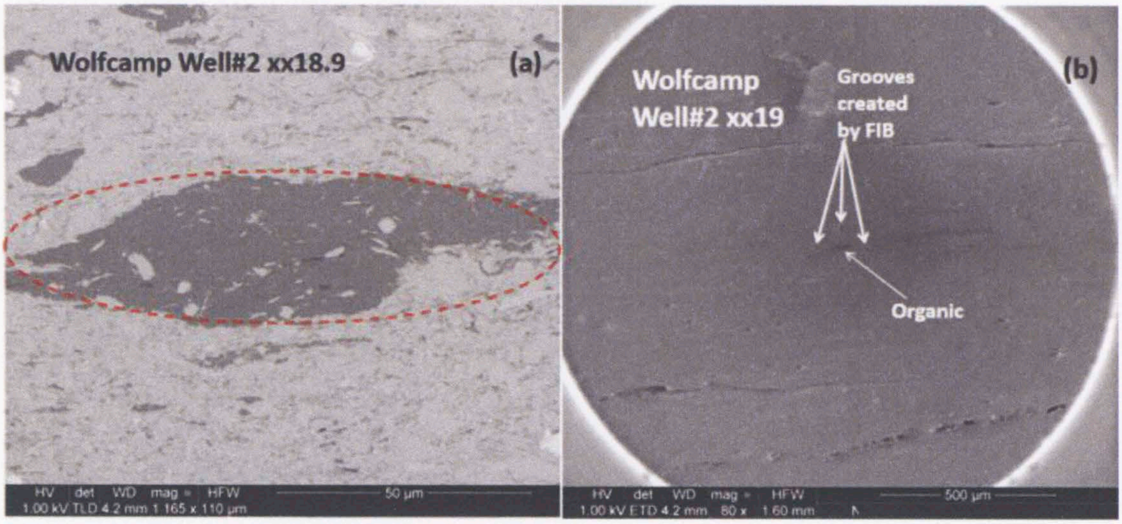

Figure 91: (a) BSE image of Wolfcamp shale sample. Dark portion shows 50 μm wide by 20 μm organic maceral encircled in red. (b) BSE image of shale sample; grooves are created around organic using FIB/SEM for easy identification on nanoindenter microscope.

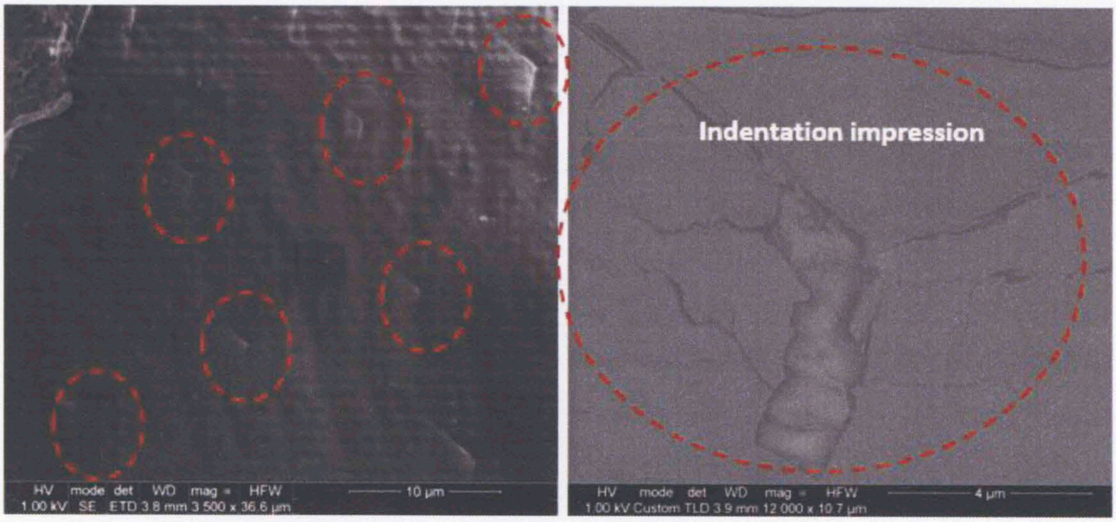

Figure 92: (Left) BSE image of organic showing residual indentations encircled in red (Right) Magnified BSE image of a single indentation impression 10 µm across.

Following is a discussion of results obtained on each sample studied. Some organics were found to contain porosity of their own. Curtis et al., (2011) and Curtis et al., (2012) have studied organics using SEM and dependence of organic porosity on thermal maturity in Woodford and Marcellus shales. Their findings do not indicate a direct relationship between organic porosity and thermal maturity. But they found extensive porosity development in more mature samples. Pre-indentation BSE images of each sample were processed using ImageJ software and porosity was calculated using opacity control.

Wolfcamp Well#1 xxx07

One organic element was located in this sample. SEM images for this organic are shown in Figure 93 along with a magnified image. Vitrinite reflectance for this sample was 1.82% calculated from T_{max} = 499 °C using the expression proposed by Espitalie, (1985). TOC was measured to be 5.3 wt%. Almost no porosity (0.2%) was found in the organic. Indentation Young's modulus in organics was found to be 8.8±2 GPa and in the adjoining matrix was 28±3 GPa. Hardness in organics was found to be 0.42±0.1 GPa and in the adjoining matrix was found to be 1.02 GPa.

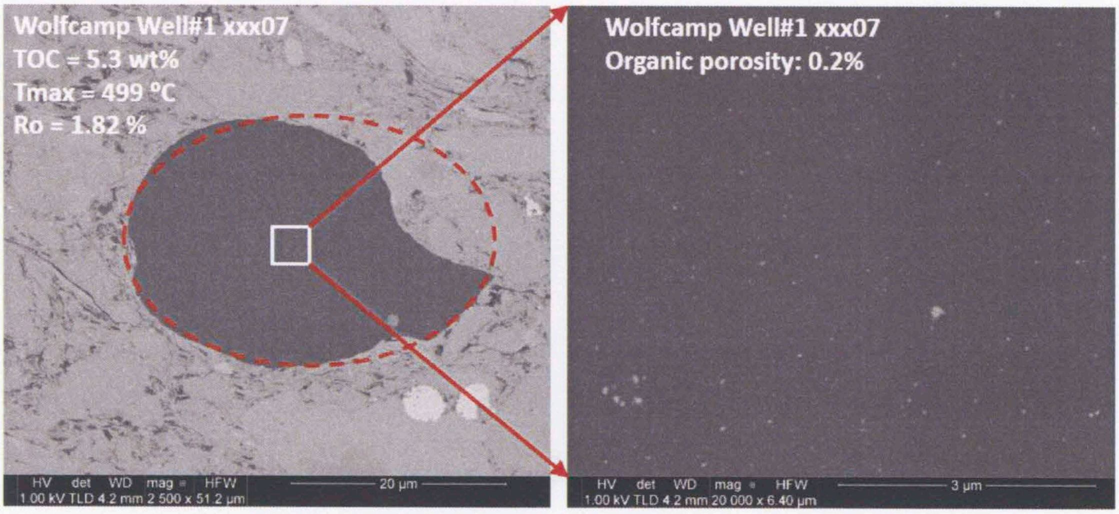

Figure 93: (Left) BSE image of organic in Wolfcamp shale sample Well#1 xxx07 encircled in red. (Right) Magnified image of organic site showing almost no porosity at 20000x magnification.

Wolfcamp Well#1 xxx37

One organic element was located in this sample. SEM images for this organic are shown in Figure 94 show the organic and its magnified image. Vitrinite reflectance for this sample was 1.86% calculated from T_{max} = 501 °C. TOC was measured to be 3.1 wt%. Porosity in the organic was found to be 0.1%. Indentation Young's modulus in organic was found to be 14.7±1.5 GPa and in the adjoining matrix was 37±2 GPa. Hardness in organics was found to be 1.2±0.6 GPa and in the adjoining matrix was found to be 0.71±0.1 GPa.

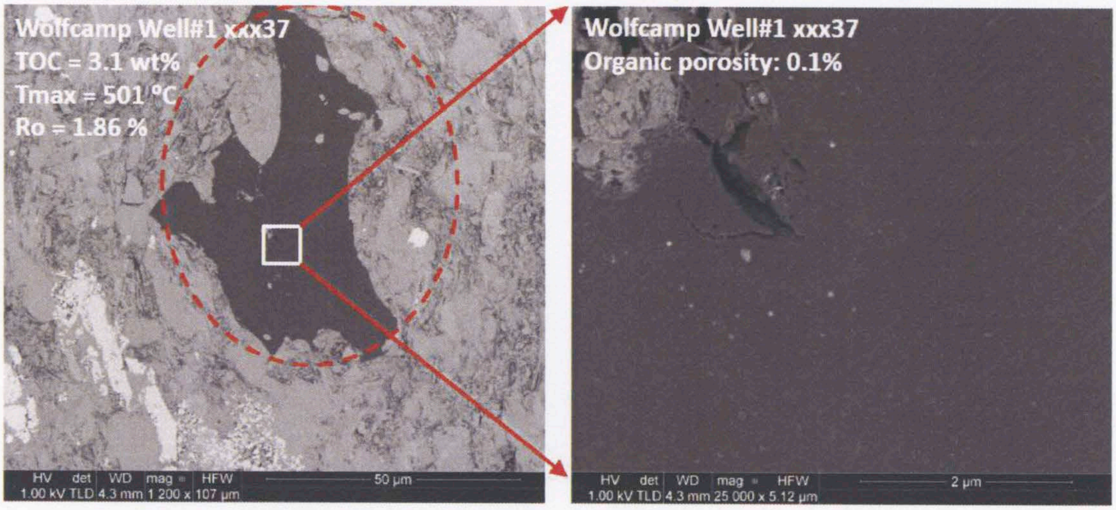

Figure 94: (Left) BSE image of organic in Wolfcamp shale sample Well#1 xxx37 encircled in red. (Right) Magnified image of organic site showing almost no porosity at 25000x magnification.

Wolfcamp Well#2 xx18.9

One organic element was located in this sample. SEM images for this organic are shown in Figure 95 show the organic and its magnified image. Vitrinite reflectance for this sample was 0.42% calculated from T_{max} = 421 °C. TOC was measured to be 2.8 wt%. Porosity in the organic was found to be 9%. Indentation Young's modulus in organics was found to be 8.5 GPa and in the adjoining matrix was 37±2 GPa. Hardness in organics was found to be 0.35 GPa and in the adjoining matrix was found to be 0.96±0.1 GPa.

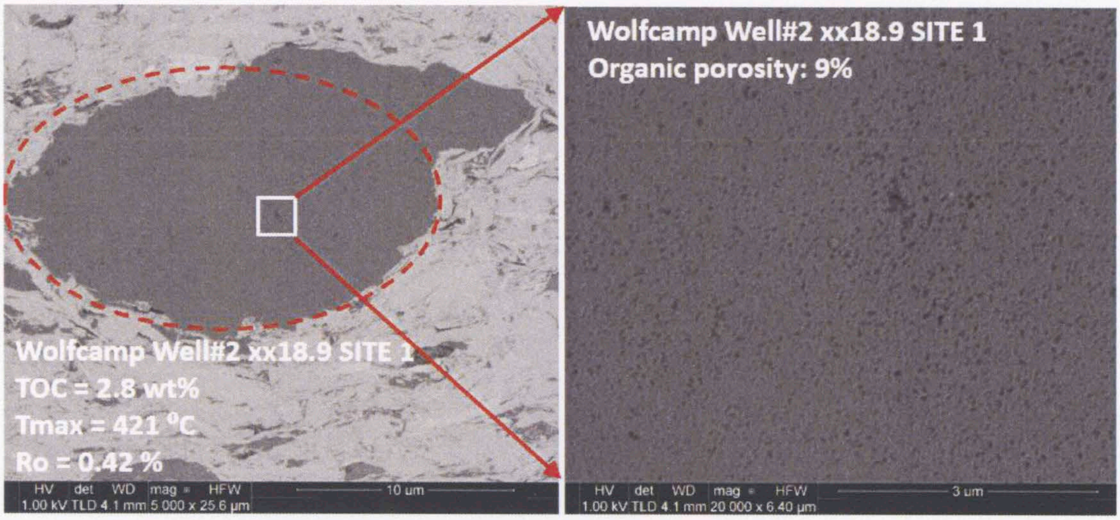

Figure 95: (Left) BSE image of organic in Wolfcamp shale sample Well#2 xx18.9 encircled in red. (Right) Magnified image of organic site showing 9% porosity at 20000x magnification.

Wolfcamp Well#2 xx19.9

Two organic elements were located in this sample. SEM images for both along with magnified images are shown in Figure 96 and 97. Vitrinite reflectance for this sample was 0.42% calculated from T_{max} = 421 °C. TOC was measured to be 2.8 wt%. No organic porosity was found in the first maceral. Indentation Young's modulus in was measured to be 8.5±1.2 GPa and in the adjoining matrix was 34±2 GPa. Hardness in organics was found to be 0.33±0.02 GPa and in the adjoining matrix was found to be 1.42±0.2 GPa. The second maceral showed a porosity of 5%. Indentation Young's modulus in was measured to be 6.7 GPa and in the adjoining matrix was 34±2 GPa. Hardness in organics was found to be 0.32 GPa and in the adjoining matrix was found to be 1.42±0.2 GPa.

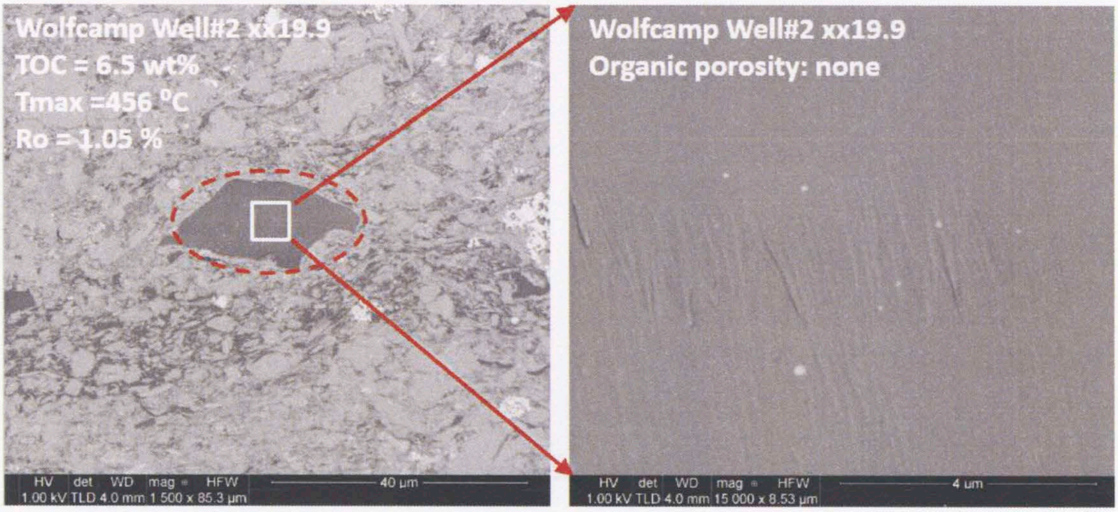

Figure 96: (Left) BSE image of organic in Wolfcamp shale sample Well#2 xx19.9 encircled in red. (Right) Magnified image of organic site showed no porosity at 15000x magnification.

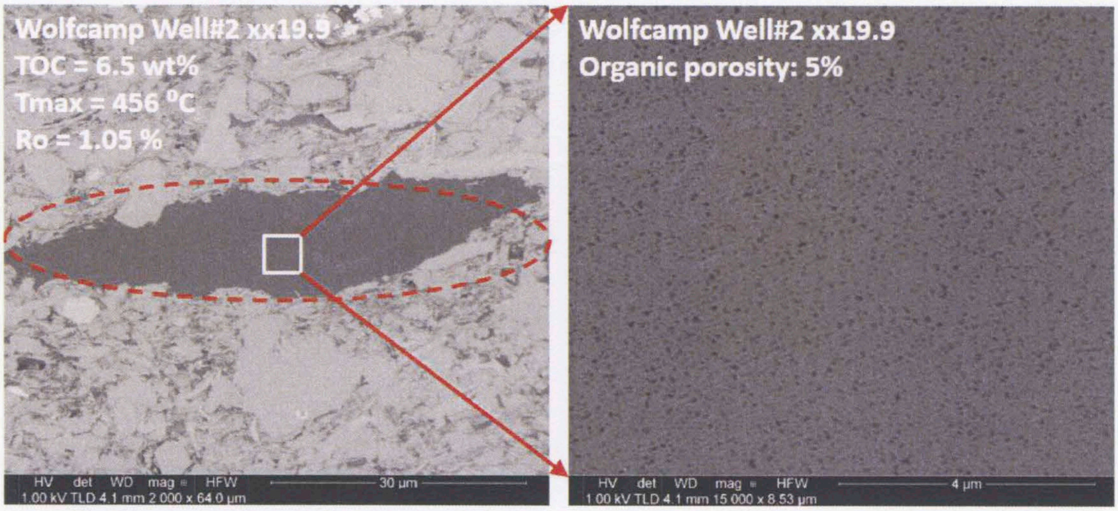

Figure 97: (Left) BSE image of organic in Wolfcamp shale sample Well#2 xx19.9 encircled in red. (Right) Magnified image of organic site showed 5% porosity at 15000x magnification.

Barnett ASW

Two organic constituents were located in this sample. SEM images for both along with magnified images are shown in Figure 98 (Site 1) and 99 (Site 2). Measurements of TOC, vitrinite reflectance and R_o were not taken up due to limited sample availability. Indentation Young's modulus of organic was measured to be 22±4 GPa and in the adjoining matrix to be 38±3 GPa. Hardness in organics was found to be 2.95±0.4 GPa and in the adjoining matrix was found to be 2.32±0.2 GPa. The second maceral showed organics present as framboids and a porosity of 17%. Indentation Young's modulus in organic was measured to be 3.1±0.6 GPa and in the adjoining matrix was 27±2 GPa. Hardness in organic was found to be 0.13±0.1 GPa and in the adjoining matrix was found to be 1.41±0.2 GPa.

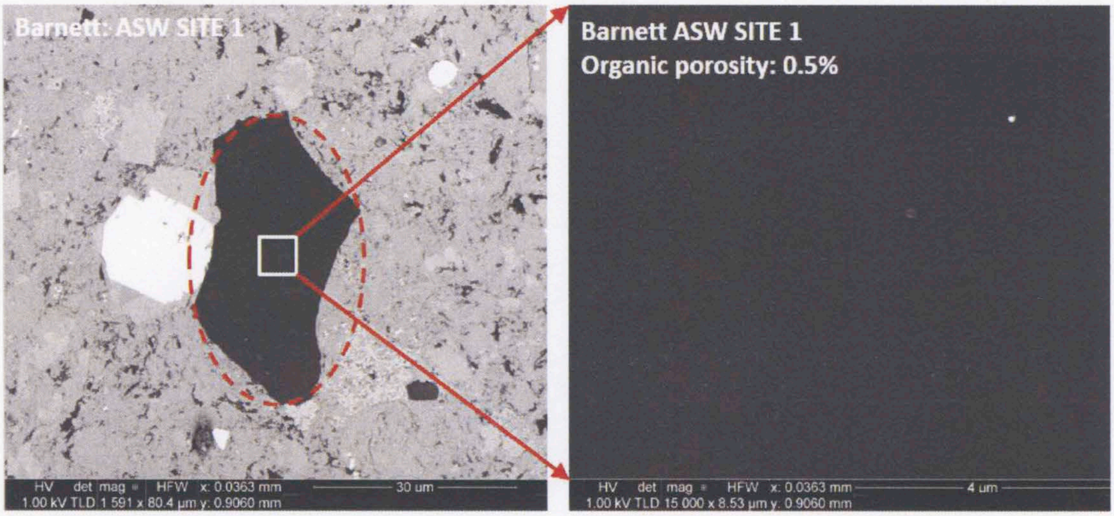

Figure 98: (Left) BSE image of organic in Barnett shale sample at ASW Site 1 encircled in red. (Right) Magnified image of organic site 1 showed no porosity at 15000x magnification.

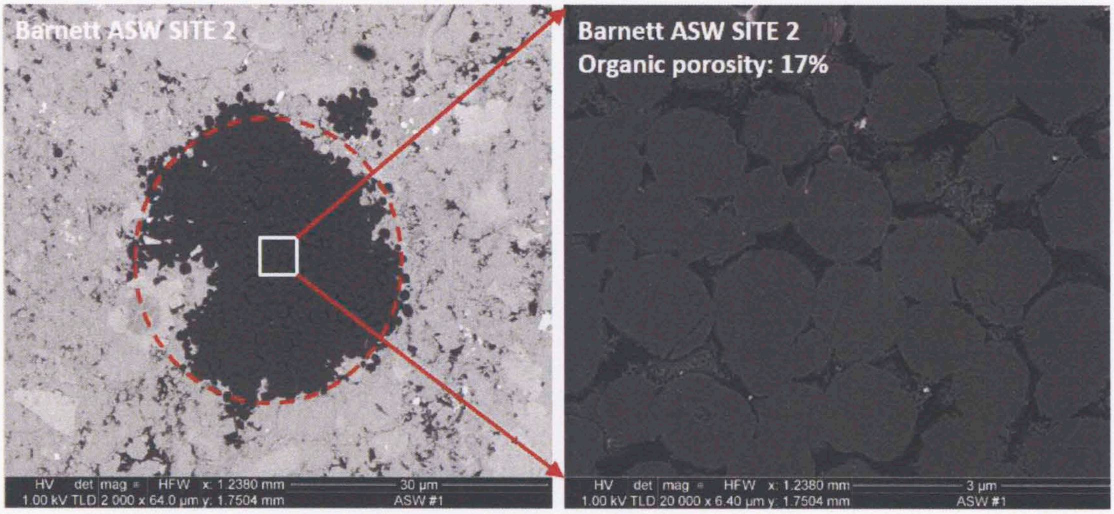

Figure 99: (Left) BSE image of organic in Barnett shale sample ASW Site 2 encircled in red. (Right) Magnified image of organic site 2 showed 17% porosity at 20000x magnification. Organics were present as framboids.

A summary of TOC, T_{max}, Ro, porosity and mechanical properties for all organics studied are presented in Table 10. Table also combines measurements by Kumar, (2012a) on Woodford shale. Samples are arranged in the increasing order of organic porosity. R_o values in blue were calculated based on T_{max} measurements. T_{max} values in red were calculated based on measured R_o values.

Table 10: Results on mechanical properties of organics tested in this study and by Kumar, (2012a). Samples are arranged in increasing order of organic porosity. Dependence of E_i on porosity is evident but no clear dependence of E_i on thermal maturity was observed. Values in blue are calculated R_o from T_{max} and those in red are calculated T_{max} from R_o.

Well	Formation	$\phi_{organic}$ %	TOC wt%	Ro %	T_{max} °C	E GPa	H GPa
MHTS xx56	Woodford	0	-	1.61	441	7.6	0.50
Newman xx19.9	Wolfcamp	0	6.5	1.05	456	8.5	0.33
Opal 960	Woodford	0	-	6.36	751	15.3	2.00
Opal 1549	Woodford	0	-	0.90	448	6.9	0.55
Hutt xxx07	Wolfcamp	0.2	5.3	1.82	499	8.8	0.42
Hutt xxx37	Wolfcamp	0.1	3.1	1.86	501	14.7	1.20
ASW	Barnett	0.5	-	-	-	22	2.95
URD xx95	Woodford	0.2	7.1	0.54	436	8.7	0.90
Newman xx19	Wolfcamp	0	7.3	1.03	455	2.5	0.15
Newman xx22	Wolfcamp	0	6.1	0.96	451	4.4	0.46
Newman xx19.9	Wolfcamp	5	6.5	1.05	456	6.7	0.57
Opal 900	Woodford	5.8	-	3.60	598	4.7	0.39
Newman xx18.9	Wolfcamp	9	2.8	0.42	421	8.5	0.35
URD xx95	Woodford	11	7.1	0.69	436	2	0.14
ASW	Barnett	17	-	-	-	3.1	0.13
SA xxx48	Woodford	-	13.2	1.32	471	6.2	0.20
K2	Kimmeridge	Low	49	0.37-0.53		5.6	0.20
Average						**8**	**0.67**

The samples with higher organic porosity show lower Young's modulus and vice versa. There were a few exceptions. Dependence of Young's modulus in organics on thermal maturity cannot be ruled out but data obtained so far does not support this thesis. Shale maturity affects its characteristics such as geomechanical properties, sonic velocities, bulk density, resistivity and porosity (Schmoker and Hester, 1983; Passey et al., 1990, 2010; Vernik and Liu, 1997; Prasad, 2001; from Zargari et al., 2011). Maturation of kerogen and resultant expulsion of hydrocabons with maturation makes it much stiffer which changes its physical properties (Prasad et al., 2009; Mba and Prasad, 2010; from Zargari et al., 2011). Curtis et al., (2011) have shown a dependence or organic porosity on thermal maturity, with more matured shales showing higher organic porosity. As a corollary, Young's modulus of organics must also depend on thermal maturity. Role of different organic matter also needs to be considered. Results from our study in Wolfcamp shale has shown multiple organic types in the same sample; one showing no porosity while other having considerable porosity as presented for the sample Barnett ASW. This suggests that thermal maturity alone does not affect development of porosity in organics. It is also possible that the two organic components are from two different sources and were geologically moved to the same depth and hence they are exhibiting different porosities. Bathija et al., (2009) have shown development of fractures/microcracks in shales with maturity and Curtis et al., (2012) have shown development of cracks in organics from the oil window in Woodford shale. Mba and Prasad, (2010) have studied Bakken shale samples to understand the effect of thermal maturity on elastic properties. They used a threshold on 33 GPa as a cut-off between clay and organics and other harder materials. Their observations suggest an increase in elastic modulus of clay and organics with increasing maturity. But the samples were not studied under SEM post indentation so it remains unconfirmed whether the indenter was hitting clay or organics.

Some other researchers have also studied the properties of organics as a function of maturity. Zeszotarski et al., (2004) studied Woodford shale sample with a R_o of 0.42% using AFM and found Young's modulus of 9.5 GPa. One of the samples from

Wolfcamp shale in this study having the same R_o of 0.42% showed indentation Young's modulus of 8.5±1.2 GPa. These moduli are comparable, however the Wolfcamp shale sample showed 9% organic porosity while no porosity information is available from the results by Zeszotarski et al., (2004). Ahmadov, (2011) have also used AFM technique to study one organic sample each from Lockatong formation in Pennsylvania and Bazhenov formation in West Siberia. They have found increase in Young's modulus with increase in maturity. However no information was available on the organic porosities in these samples. These results are presented in Table 11.

Table 11: Observations on elastic properties of organics as reported by Zeszotarski et al., (2004), Ahmadov et al., (2009) and Ahmadov, (2011).

Well	Formation	$\phi_{organic}$ %	TOC wt%	Ro %	T_{max} °C	E GPa	H GPa
Zeszotarski et al. (2004)	Woodford	-	22	0.42	421	9.5	0.57
Ahmadov et al. (2011)	Bazhenov	-	4.4	0.78	441	5.9	-
	Lockatong	-	4.1	2.58	541	11.9	-

Two samples in Well#2 showed large visible streaks/veins of organic/bituminous material within the matrix. Further confirmation for the presence of organics was done using EDS. TOC, Ro, T_{max} in sample 1 and sample 2 were 7.3 wt%, 1.03%, 455 ^{0}C and 6.1 wt%, 0.96% and 451^{0}C, respectively. No organic porosity was visible in these samples under SEM. These samples were studied using nanoindentation and the Young's modulus in sample 1 was found to be 2.5±0.3 GPa and 4.4±0.4 GPa in sample 2. Since the veins extended through the sample for 1.8 cm, another experiment was attempted to confirm the presence of organics. Samples were subjected to low temperature plasma ashing which removes the organic. Half of the sample was covered using a glass slide while the other half was exposed to ashing. After 6 hours of ashing, it was observed in both the samples that organics were removed from the half which was left exposed while organics under the glass slide were visibly unaltered. Nanoindentation was repeated on the remaining organics for both samples from the covered portion and it was found that Young's modulus in sample 1 increased to 3.3±0.2 GPa while that in sample 2 increased to 7.4±0.4 GPa. This increase in Young's modulus can be attributed to removal of volatile organics from the covered portion due to effect of ashing on covered sample. Figures 100 and 101 show EDS and BSE images for organics present in the two samples after ashing.

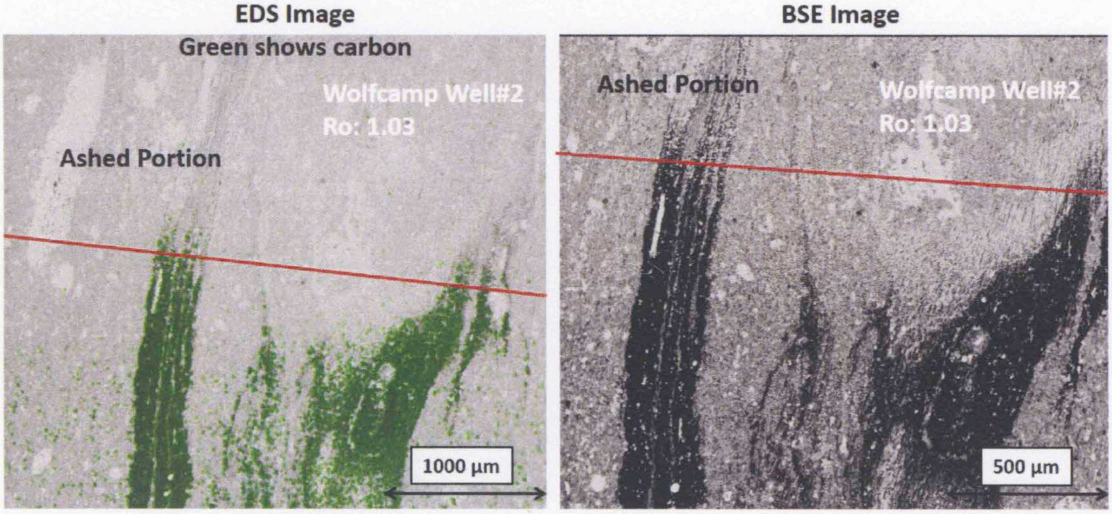

Figure 100: (Left) EDS image of sample 1 showing ashed and un-ashed portions. Organics are shown in green. (Right) BSE image of sample 1 showing ashed and un-ashed portions. Organics are shown in black. Red line shows the position of glass slide.

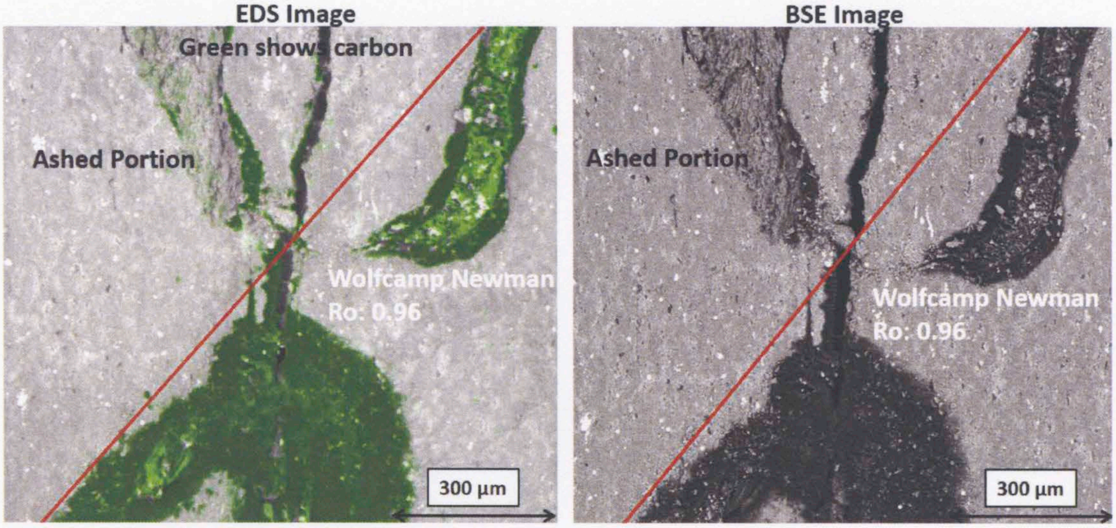

Figure 101: (Left) EDS image of sample 2 showing ashed and un-ashed portions. Organics are shown in green. (Right) BSE image of sample 2 showing ashed and un-ashed portions. Organics are shown in black. Red line shows the position of glass slide.

4.12.2 Nanoindentation Results on Dissolved Samples

Finding organics which are large enough to carry out multiple arrays of indentations for a more representative result is challenging. To meet this goal, organics were concentrated from a sample by dissolving the carbonates and silicates present in the rock using hydrochloric (HCl) and hydrofluoric (HF) acid. This technique is used for kerogen isolation for measuring vitrinite reflectance. The technique does not yield a true kerogen isolate rather a residue greatly reduced in mineral matter and dominated by organics. The organics thus recovered were converted into a thin disc of 1 cm diameter and 1 mm thickness by applying a load of 30 tons on 0.6 gram of sample. This process does not yield a perfectly smooth surface. The same disc was studied under the nanoindenter by looking for a relatively smooth region where an array of indentations can be created. Figure 102 shows image of the disc thus prepared from the organics. The disc was mounted on a glass slide using temperature resistant epoxy. This sample was then used for nanoindentation at room temperature. Two samples were studied in this manner for which the results are compiled in Table 12.

Table 12: Summary of results on organic palettes.

Shale	Sample	$\phi_{organic}$ %	Ro %	T_{max} °C	E GPa	H GPa
Kimmeridge	K2	Modified	0.4	420	1.03±0.29	0.08±0.04
Woodford	OPL	Modified	6.3	748	0.62±0.14	0.03±0.01

These results show that Young's modulus and hardness of organics decreased with increased maturity. This is contrary to the findings by Zargari et al, (2011). Kerogen expels hydrocarbons as it matures and tends to become stiffer with maturity. Also, these samples show results different from properties obtained on native state organics. More investigations need to confirm the effect of thermal maturity or solvent action on organics in altering mechanical properties of organics.

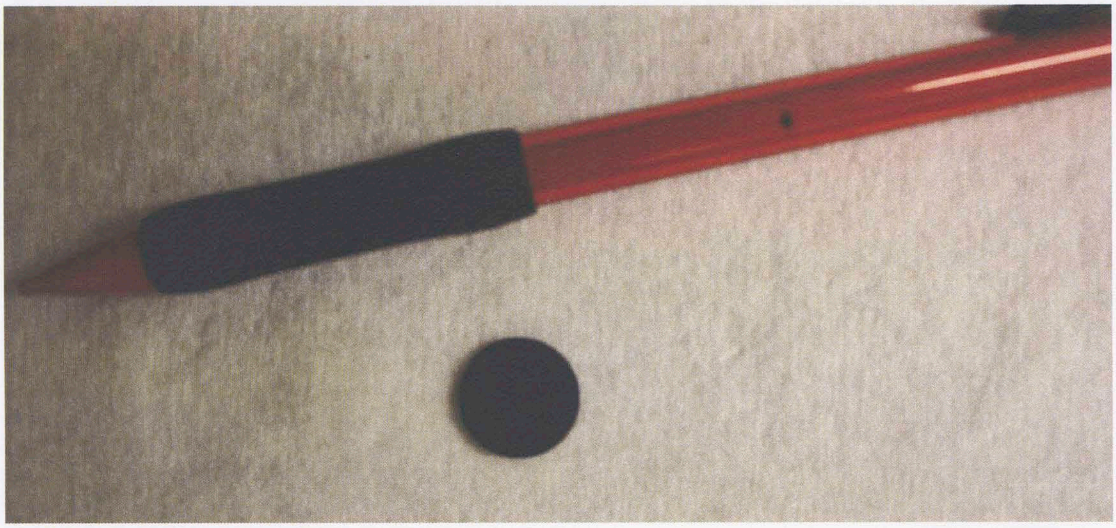

Figure 102: Disc of organics prepared by pressing the organic recovered from dissolving organic rick shale in HCl and HF. Diameter of the disc is 1 cm while thickness is 1 mm.

4.13 Investigations on Laboratory Scale Hydraulic Fracture

Brittleness and ductility of shales affects fracture morphology. Zones rich in harder minerals like quartz and carbonates have large Young's moduli and such rocks are considered more brittle. Similarly more presence of quartz also leads to lower Poisson's ratio and thus a more brittle rock. Presence of clays, feldspars and organics make the rock weaker, lowers its Young's modulus and hence such rocks are more ductile. Aoudia et al., (2010) have carried out statistical analysis to determine dependence of rock mechanical properties on mineralogy which have resulted in similar conclusions.

One sample from Barnett shale was fractured in a triaxial hydraulic fracturing experiment, Sharma, (2013). One of the sides from the resulting bi-wing hydraulic fracture was cored vertically and a disc (1 inch diameter) was recovered. Nanoindentation was performed on both the sides of this fracture to study the variation in Young's modulus along the path of the fracture. SEM mapping of fracture post nanoindentation indicated some complex development of fractures in the center of the disc. On the basis of this analysis the fracture was divided into 3 parts: left, center and right. Figure 103 presents SEM mapping images of the hydraulic fracture for the left, center and right parts.

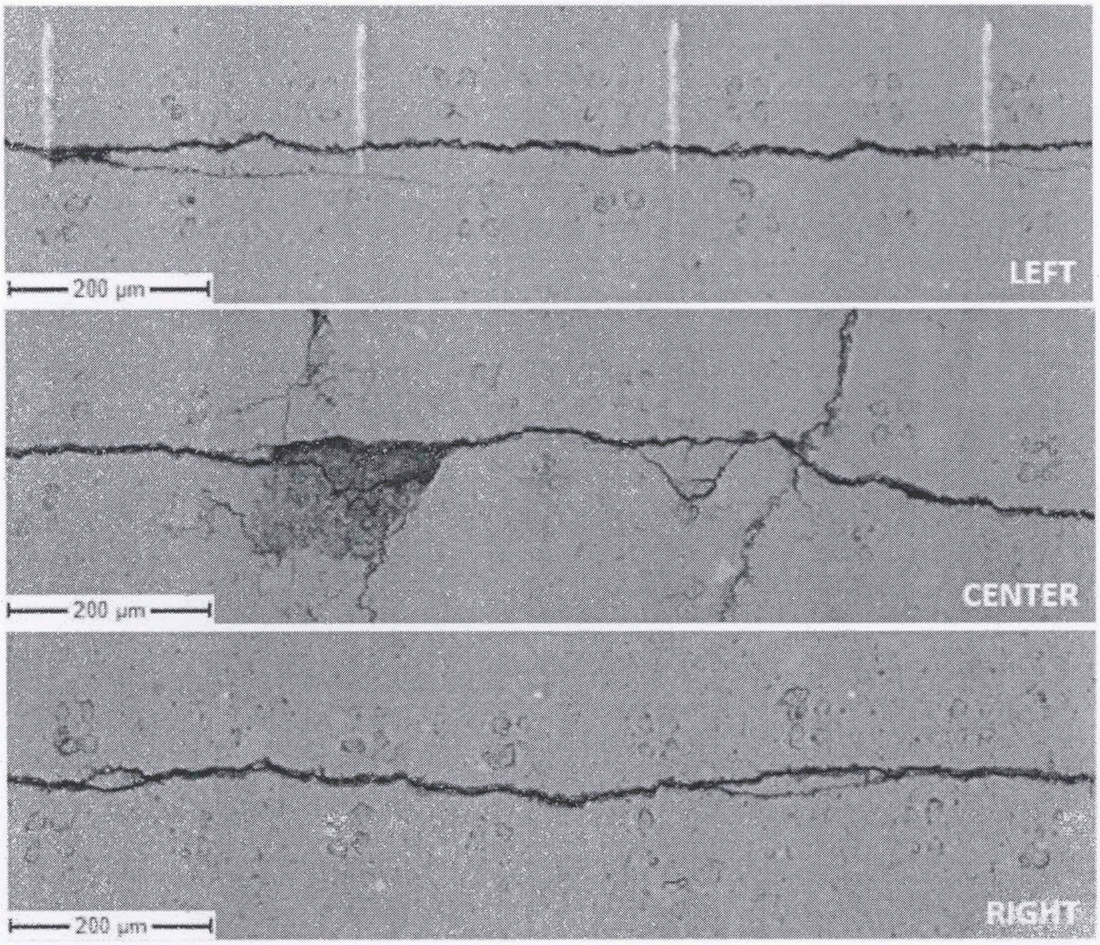

Figure 103: SEM images of hydraulic fracture for the Left, Center and Right portion along the hydraulic fracture. Lower Young's modulus was observed for the center part compared to the left and right parts. Indentation arrays in 2x2 patterns are also visible on both sides of the fracture.

The left part and right part show development of a smooth fracture with some small fractures running parallel to the main fracture. These small fractures could be the result of stress release. In the center part, more complex fracture is visible with two fractures emerging orthogonally from the main fracture. Some smaller fractures can be observed in the center part.

130 arrays of 2x2 indentations were created along the fracture; 65 arrays on either side, which makes a total of 260 indentations each on both sides of the fracture. Figure 104

presents the histogram of Young's modulus measured the three parts which provide a representative distribution of Young's modulus in the three regions.

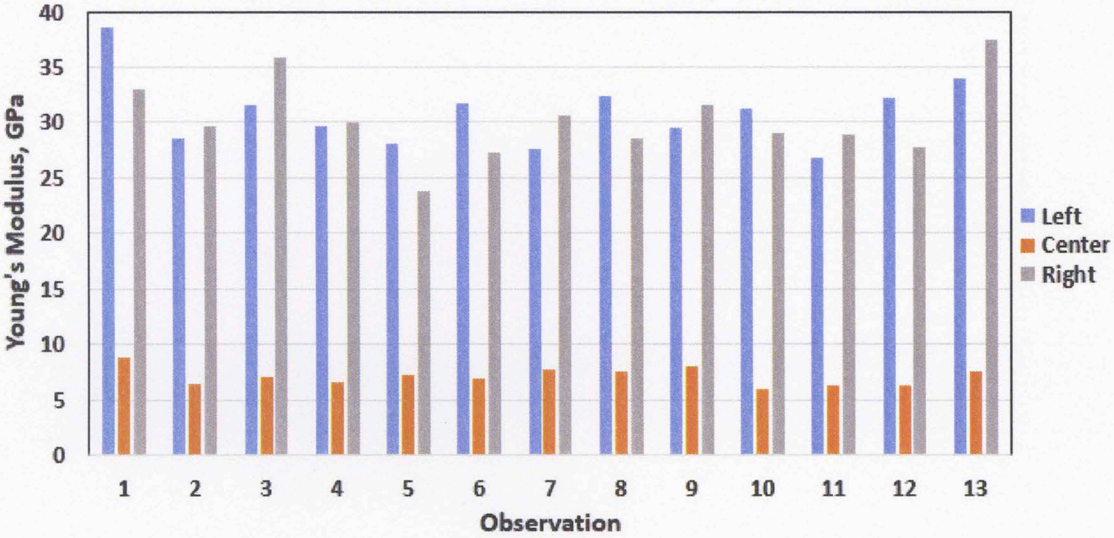

Figure 104: Average Young's modulus at 13 points each from the left, center and right parts of the hydraulic fracture. Average E_i in left, center and right parts was measured as 30, 7 and 31 GPa respectively.

We observe that while Young's modulus was very similar in the left and right part, considerably small Young's moduli were measured in the central part which showed more complex fracture behavior. Average Ei in the left, center and right parts were 30; 7 and 31 GPa respectively. This could be because weakness in the center due to complex development of fracture. This decrease in rock strength could lead to proppant embedment near the fracture surface.

4.14 Nanoindentation Studies on Other Rocks

In Chapter 3 we discussed the results from nanoindentation on metals and pure minerals while comparing them to the values available in literature. The match between Young's modulus from nanoindentation and acoustic velocities also proves the applicability of nanoindentation in fine grained rocks like shales. In this section we discuss nanoindentation results on some other rocks which are coarse grained to understand applicability of nanoindentation for such rocks. Nanoindentation experiments were carried out in the same manner as outlined for shales in Chapter 3. This study stems from the fact that the small area of investigation during a nanoindentation test contacts multiple grains of shale but for coarse grained rocks this is likely not the case. Four rocks: Lyons sandstone, Sioux quartzite, limestone, and pyrophyllite, were studied for this purpose. Table 13 provides a summary of measurements these on rocks. Figure 105 shows images of core plugs from all four non-shale rocks studied.

Table 13: Summary of measurements on Lyons sandstone, Sioux quartzite, limestone and pyrophyllite.

	Lyons Sandstone	**Sioux Quartzite**	**Limestone**	**Pyrophyllite**
Porosity (%)	5.7 - 8.9	2.5	15.6	4.3-5.9
Mineralogy (wt%)	80-85% quartz, 7-11% mixed clays	99% quartz	89% carbonates, 6% clays	pyrophyllite minerals
Grain Density (g/cc)	2.64-2.66	2.65	2.7	2.83-2.84
Grain Size	190 μm	fused grains	500 μm	very fine
Dynamic Young's Modulus (GPa)	57-60	71-82	36-41	30-34
Indentation Young's Modulus (GPa)	84-96	90-100	42-55	34-40

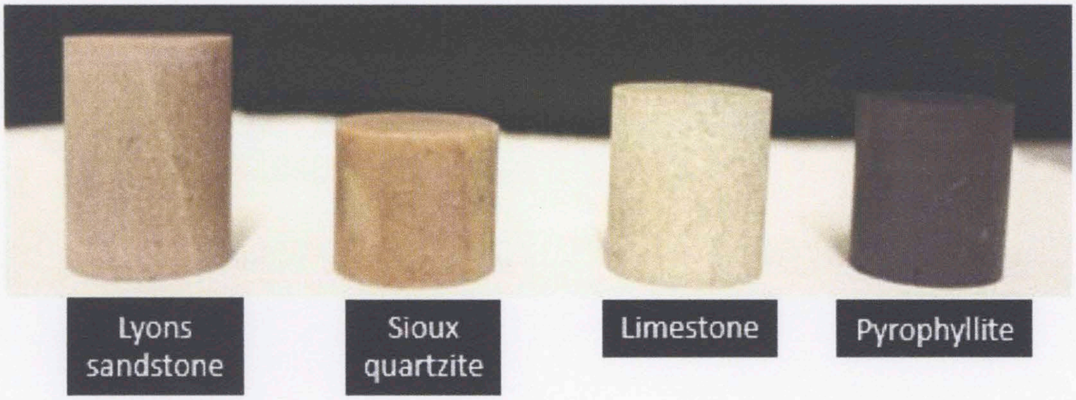

Figure 105: Core plug images for (left to right) Lyons sandstone, Sioux quartzite, limestone and pyrophyllite.

4.14.1 Lyons Sandstone

Lyons sandstone was formed out of compaction of sand dunes and is extensively used for construction applications. Data from Table 9 suggests an average grain density of 2.65 g/cc which is same as that of quartz. Also the Young's modulus from nanoindentation was between 84-96 GPa, which is comparable to the Young's modulus of quartz grains (Table 3). This is much greater than the Young's modulus calculated from acoustic velocities which was found to be between 57-60 GPa. Since the grain size is approximately 190 μm, all the indentations are essentially on a single grain which will be quartz based on rock mineralogy. A SEM image of Lyons sandstone is presented in Figure 106 (a). The reason for lower Young's modulus from acoustic measurements can be explained by looking at the pressure dependence of velocities. Figure 106 (b) shows a plot of P-wave and S-wave velocities as a function of pressure. It is evident that velocities are increasing as a function of pressure due to crack closure in the rock. This increasing trend is visible even at 3000 psi indicating that there are still some open cracks. Acoustic velocities also measure the effect of clays and other components present in the rock. Nanoindentation measurements due to their small depth of investigation are not sensitive to the presence of cracks and other minerals that may lie beneath or around and grains.

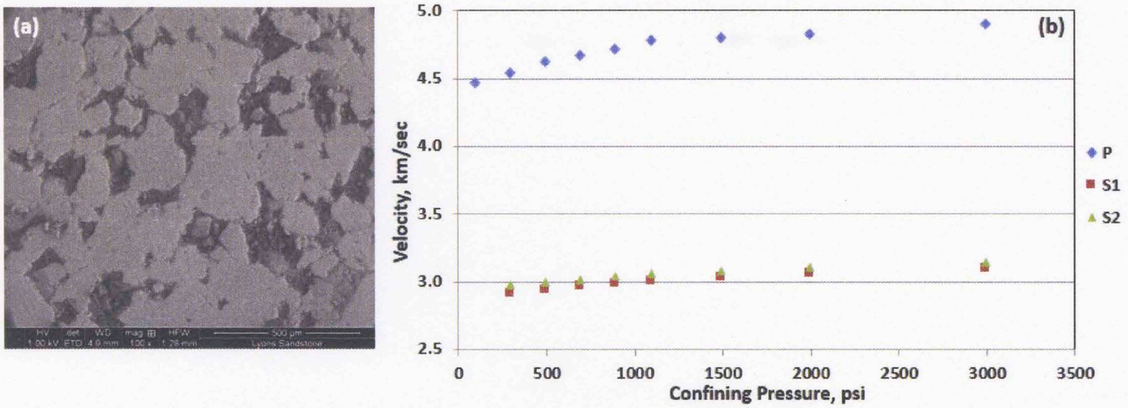

Figure 106: (a) SEM image of Lyons sandstone ~1200 μm across. Light grey portions indicate grains while dark grey portions are surface depressions. (b) Pressure dependence of P and S wave velocities in the dry sample showing increasing trend for velocity with increasing pressure.

4.14.2 Sioux Quartzite

Sioux quartzite is primarily quartz and is composed of rounded, fine to medium (0.125-0.5 mm) grains. Grain density measured was also 2.65 g/cc. Dynamic Young's modulus was measured to be 71-82 GPa, while nanoindentation Young's modulus was 90-100 GPa which is same as that for quartz grains. Figure 107 (a) shows a SEM image of Sioux quartzite with an array of 5x5 indentations. We observe that indentation and dynamic moduli are in close agreement. This can be understood with the help a plot on the pressure dependence of velocities. Figure 107 (b) shows a plot of P and S-wave velocities as a function of pressure. It is evident that velocities increase as a function of pressure. But the change in velocities is small after 3000 psi indicating that most of the cracks in the system are closed. Also, since Sioux quartzite is made up of almost pure quartz, the dynamic Young's modulus tends to the value for pure quartz. Indentation Young's modulus was measured to be between 90 and 100 GPa, which is similar to that for pure quartz.

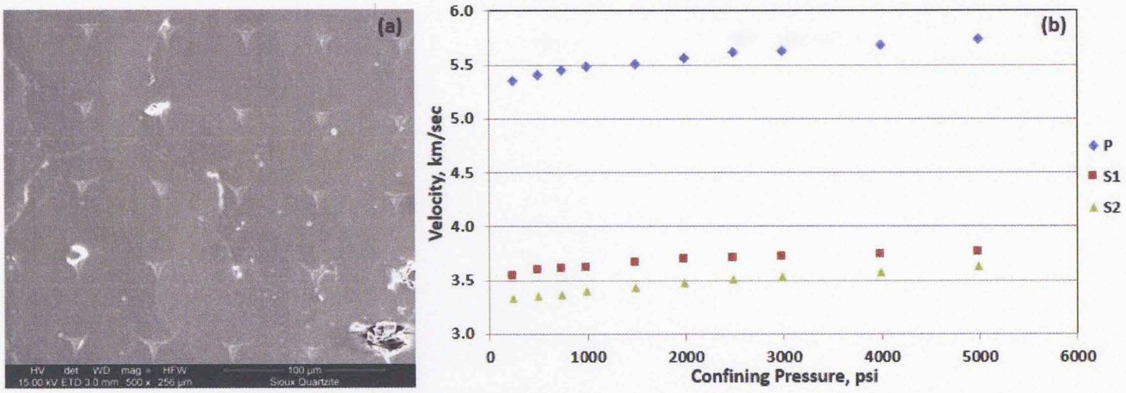

Figure 107: (a) SEM image of Sioux quartzite ~220 µm across. All grains appear to be fused (b) Pressure dependence of P and S wave velocities in a dry sample showing increasing trend for velocity with increasing pressure which becomes gradual at 3000 psi.

4.14.3 Limestone

Limestone sample from core plugs was extracted and a part of it was used for nanoindentation while other part was used for measuring velocities through the sample. Sample mineralogy showed 89% carbonates and 6% clays while the grain density was measured to be 2.70 g/cc. Grain size was measured using SEM to be 500 µm. Figure 108 (a) shows a SEM image of the limestone showing nanoindentation arrays. Dynamic Young's modulus was measured to be 36-41 GPa, while nanoindentation Young's modulus was 42-55 GPa; close agreement. This difference can be explained by plotting P and S-wave velocities as a function of confining pressure (Figure 108 (b)). It is evident that velocities become constant after 2000 psi which indicates that cracks are closed at this pressure. Hence the Young's modulus from both measurements is very similar.

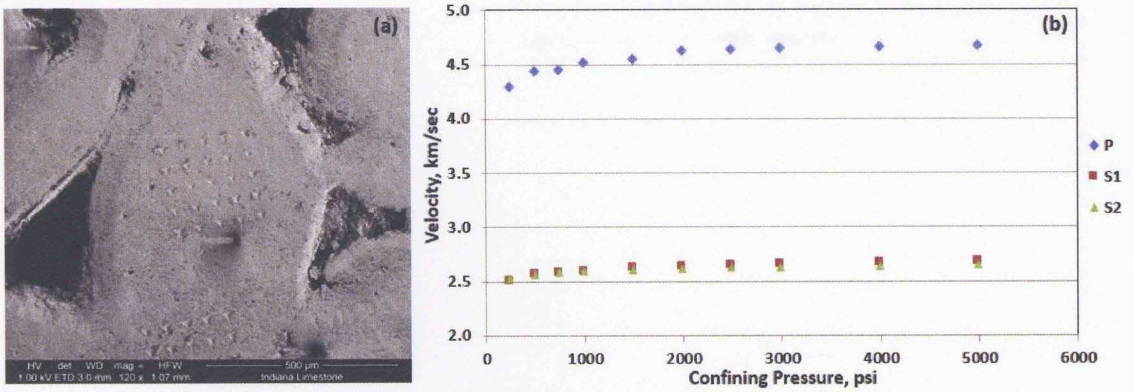

Figure 108: (a) SEM image of limestone ~1200 µm across. Light grey portions indicate grains while black portions are surface depressions between grains. (b) Pressure dependence of P and S-wave velocities in a dry sample showing increasing trend for velocity with increasing pressure which becomes constant at 2000 psi.

4.14.4 Pyrophyllite

Pyrophyllite sample possessed very fine grains (2-4 µm) and has a grain density of 2.83-2.84 g/cc. Figure 109 (a) shows an SEM image of pyrophyllite sample which shows very fine grains and no grain boundaries are visible. Dynamic Young's modulus was measured to be between 30-34 GPa, while nanoindentation Young's modulus was measured between 34-40 GPa. This result can be explained from the plot of pressure dependence of velocities as shown in Figure 109 (b). It is evident that there is very small change in velocities from 0 to 2000 psi.

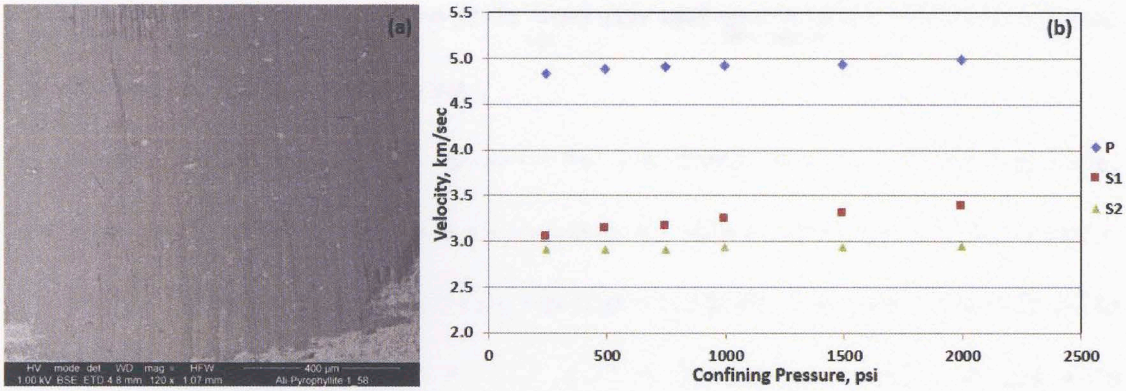

Figure 109: (a) SEM image of pyrophyllite 1000 µm across. Image shows no grain boundaries due to extremely fine grains present. (b) Pressure dependence of P and S-wave velocities in a dry sample showing slight increase in velocities with increasing pressure.

Results from nanoindentation on Lyons sandstone, Sioux quartzite, limestone and pyrophyllite indicate that nanoindentation technology can be applied for fine grained rocks in which size of grains is much less than the area of penetration of the indenter. As the grain size increases the possibility of indenter hitting a single grain increases. Therefore for samples with larger grains, nanoindentation ends up measuring the properties of grains rather than the composite matrix. Results for fine grained samples from dynamic and nanoindentation data were found to match at higher confining pressures due to closure of cracks.

4.15 Summary

1. Results from 134 samples from 3 wells in Wolfcamp shale suggest that Young's modulus, E_i, parallel to bedding varied from 30 to 93 GPa with an average value of 45±5.8 GPa. Hardness, H_i, parallel to bedding varied from 0.48-6.67 GPa with an average value of 1.48±0.32 GPa. E_i perpendicular to bedding in Wolfcamp shale varied from 11 to 93 GPa with an average value of 36±5.8 GPa. H_i perpendicular to bedding Wolfcamp shale from 0.36 to 6.98 GPa with an average value of 1.31±0.36

GPa. Two wells in Wolfcamp shale were clay and quartz rich while the third well was rich in carbonates and quartz.

Average horizontal Young's modulus for Woodford, Barnett, Haynesville, Eagle Ford, Collingwood and Kimmeridge shales are 42±5, 50±6.2, 47±15.6, 41±10.7, 54±4.5, and 7.4±3 GPa respectively, while average horizontal hardness was found to be 1.07±0.15, 1.41±0.3, 1.06±0.57, 0.77±0.37, 1.2±0.16, and 0.3±0.04 GPa respectively.

2. Samples with more carbonate concentration showed larger standard deviation in the nanoindentation results for Young's modulus and hardness. This was due to variable scatter of carbonates in the sample as confirmed by EDS.
3. Nanoindentation allows to measure Young's modulus on differently oriented samples to quantify anisotropy. Previous measurements of Young's modulus anisotropy were 0.25±0.06 (Sondergeld at al., 2000), 0.3±0.1 (Vernik and Nur, 1992), 0.24±0.13 (Vernik and Liu, 1997), 0.18±0.14 (Kumar, 2012a). Anisotropy in this study was found to lie between 0 and 1.4 with majority of the values lying in the range 0.1 to 0.5. Vertical and horizontal measurements of Young's modulus on Wolfcamp shale show average horizontal and vertical Young's modulus ratio to be 1.65. This ratio was much lower for samples rich in carbonates. Larger ratios were observed for clay rich samples indicating that they were more anisotropic. Quantification of anisotropy is necessary from geomechanics standpoint for estimation of stresses, wellbore instability mitigation, seismic applications etc.
4. Young's modulus and hardness are related to rock composition. They are inversely proportional to TOC, porosity and clay content which are the soft components, and

directly proportional to quartz and carbonate content which are the "hard" components. Carbonate streaks were found to be present in shales which led to higher Young's modulus in some intervals.

In Wolfcamp shale, for carbonate concentration more than 40 wt%, the Young's modulus and hardness were found to be constantly increasing with increasing carbonate content and Young modulus was as high as 93 GPa. For clay concentration more than 40 wt%, hardness and Young's modulus were found to vary between 30 to 45 GPa; for the same depths the carbonate concentration was less than 40 wt%.

Large scatter was observed in the crossplots for porosity and TOC versus Young's modulus at low values of porosity and TOC. Equations relating E_i and H_i to mineralogy, TOC and ϕ for Wolfcamp shale and for all the shales are presented. These indicateindicates better predictability from the equation for Wolfcamp shale than the general equation for all the shales indicating that each play is different based on its mineralogy and properties. These equations were

For Wolfcamp Shale

$E_i = 69 - 1.60 * \varphi - 2.13 * \mathrm{TOC} - 0.24 * \mathrm{Clay} + 0.11 * \mathrm{QC}$; $R^2=0.82$

$H_i = 3.53 - 0.04 * \varphi - 0.13 * \mathrm{TOC} - 0.03 * \mathrm{Clay} + 0.002 * \mathrm{QC}$; $R^2=0.64$

General equation for all shales studied

$E_i = 71 - 2.14 * \varphi - 1.18 * \mathrm{TOC} - 0.24 * \mathrm{Clay} + 0.05 * \mathrm{QC}$; $R^2=0.75$

$H_i = 3.34 - 0.08 * \varphi - 0.04 * \mathrm{TOC} - 0.03 * \mathrm{Clay} + 0.005 * \mathrm{QC}$; $R^2=0.55$

5. Nanoindentation Young's moduli on small fine grained samples showed an excellent match with dynamic Young's modulus following the equation $E_d = 1.91 +$

$0.97E_i$, and showing an R^2 of 0.94. Such a finding makes it possible to use nanoindentation test data for shales where core plugs cannot be recovered.

6. Nanoindentation results on simulated drill cuttings at room temperature indicate that Young's modulus measurements on drill cuttings lie between the values measured on vertical and horizontal samples. This provides capability to obtain representative Young's modulus measurements from randomly oriented drill cuttings where cores cannot be obtained.

   Nanoindentation measurements on simulated drill cuttings at room temperature and elevated temperature showed good agreement with horizontal measurements at room temperature. Temperature (110°C) did not significantly affect the results.

7. Nanoindentation results on horizontal samples from Wolfcamp Well#1 indicated that till 100°C (reservoir temperature), there was no significant effect of temperature on carbonate rich samples or in the samples which had carbonates present on the polished sample surface, while Young's modulus was found to be decreasing in clay rich samples at elevated temperature. This decrease was measured to be about 16%. Obviously more work needs to be done.

8. Young's modulus in organics was found to be dependent on organic porosity. More porous organics showed Young's modulus to be as low as 2 GPa while organics with no porosity showed Young's modulus as high as 22 GPa.

   Average Young's modulus in organics was found to be 4 times lower than that of the matrix.

   Results on Young's modulus of organics extracted after dissolution of matrix showed Young's modulus less than 2 GPa for 2 samples. These samples had no inherent organic porosity, and Young's modulus could also depend on the degree of compaction used to make the disc.

9. Nanoindentation results on other rocks suggest that for rocks of large grain size, nanoindentation measures grain properties rather than the bulk matrix behavior which includes cracks.

CHAPTER 5: CONCLUSIONS

1. Nanoindentation Young's modulus measured on shale are related to variations in basic petrophysical parameters like porosity, TOC and mineralogy. TOC and porosity were found to be the dominant factors governing Young's modulus.
2. Nanoindentation Young's modulus was found to agree with dynamic Young's modulus.
3. There was no significant effect of temperature on the shale samples rich in carbonates for the temperatures used in this study. Decrease in Young's modulus was observed for samples rich in clay. Other researchers have found Young's modulus in the shales to decrease with temperature.
4. Measurements on polished simulated drill cuttings in shale show that nanoindentation is a viable technique of obtaining Young's modulus when cores are not available. However anisotropy information cannot be obtained from drill cuttings.
5. Average Young's modulus of organics was found to be 4 times less than average Young's modulus of the matrix. Young's modulus of organics decreases with increase in organic porosity. More studies are needed to establish dependence of Young's modulus on organic maturity.

Application to the Industry

Young's modulus and hardness are important inputs hydraulic fracturing and subsequent propping of the fractures. Conventionally sonic logs are run to obtain mechanical properties. Nanoindentation provides a convenient and cheap method to measure mechanical properties in shales using plugs fragments and/or drill cuttings.

This data can therefore be used as a substitute when other direct measurements are too expensive or impossible. Quantification of mechanical anisotropy in shales can help in correct estimation of minimum horizontal stresses and wellbore instability issues can be controlled. Shales have been found to contain variable amounts of organic content which are laminated parallel to bedding and contribute towards anisotropy. They also contribute toward a significant pore volume in the reservoir. Organics which are non-stress supporting will have larger pores with increasing pore pressure and increase storage capacity of the rock. More mature organics have less volatile matter and tend to be "harder". Measuring mechanical properties of organics can lead to important insights about nature of organic matter in a shale. Sayers, (2013) point out that there is greater change in horizontal effective stress for a given change in pore pressure for organic rich shales. Hence organics can have significant impact on geomechanical properties of such shales making their study all-the-more important.

References

1. www.eia.gov
2. www.engineeringtoolbox.com
3. Agilent Technologies. 2009. G200 User's guide. Chandler, Arizona, USA.
4. Abousleiman, Y., Minh, T., Hoang, S., Bobko, C., Ortega A., and Ulm, F. 2007. Geomechanics Field and Laboratory Characterization of the Woodford Shale: The Next Gas Play. Paper SPE 110120 presented at the SPE Annual Technical Conference Exhibition, Anaheim, California, USA., 11-14 November.
5. Abousleiman, Y., Minh, T., Hoang, S.,Ortega A., and Ulm, F. 2009. Geomechanics Field Characterization of the Two Prolific U.S. Mid-West Gas Plays With Advanced Wire- Line Logging Tools. Paper SPE 124428 presented at the SPE Annual Technical Conference and Exhibition, New Orleans, Louisiana, USA, 4-7 October.
6. Ahmadov, R., Vanorio, T. and Mavko, G. 2009. Confocal Laser Scanning and Atomic Force Microscopy in Estimation of Elastic Properties of the Organic Rich Bezhenov Formation. The Leading Edge, **28** (1): 18-23.
7. Ahmadov, R. 2011. Microtextural Elastic and Transport Properties of Source Rocks. PhD Thesis, Stanford U., Stanford, California, USA.
8. Akrad, O., Miskimins, J., and Prasad, M. 2011. The Effects of Fracturing Fluids on Shale Rock Mechanical Properties Proppant Embedment. Paper SPE 146658 presented at the SPE Annual Technical Conference and Exhibition, Denver, Colorado, USA, 30 October-2 November 2011.

9. Ambrose, R. J., Hartman, R. C., Akkutlu, I, Y. 2011. Multi-Component, Sorbed-Phase Considerations for Shale Gas-in-Place Calculations. Paper SPE presented at the SPE Production and Operations Symposium held in Oklahoma City, Oklahoma, USA, 27-29 March 2011.

10. Annual Energy Outlook, 2009, US Energy Information Administration Report# DOE/EIA – 0383 (2009), **http://www.eia.doe.gov/oiaf/aeo/gas.html**

11. Aoudia, K, Miskimins, L.J., Harris, N.B. and Mnich, C.A. 2010. Statistical Analysis of the Effects of Mineralogy on Rock Mechanical Properties of the Woodford Shale and the Associated Impacts for Hydraulic Fracture Treatment Design. Paper ARMA presented at the 44th US Rock Mechanics Symposium and 5th US-Cananda Rock Mechanics Symposium, Salt Lake City, Utah, USA, 27-30 June.

12. Banik, N.C. 1984. Velocity Anisotropy of Shales and Depth Estimation in the North Sea Basin. Geophysics, **49:** 1411-1419.

13. Bathija, P. L., Prasad, M., Liang, H., Upmanyu, M., Lu, N., and Batzle, M. 2009. Elastic Properties of Clay Minerals. Extended abstract, SEG Annual Meeting, Las Vegas, Nevada, USA, 9-14 November.

14. Boggs, S., Jr., 1992. *Petrology of Sedimentary Rocks*. Macmillan Publishing Co., New York.

15. Castano, A. F., Sondergeld, C. H., Rai, C. S. 2010. Estimation of Uncertainty in Microseismic Event Location Associated with Hydraulic Fracturing. Paper SPE 135325 presented at the SPE Tight Gas Completions Conference, San Antonio, Texas, USA, 2-3 November.

16. Cramer, D.D. 2008. Stimulating Unconventional Reservoirs: Lessons Learned, Successful Practices, Areas for Improvement. Paper SPE 114172 presented at Unconventional Gas Conference, Keystone, Colorado, USA, 10-12 February.
17. Curtis, M.E., Ambrose, R.J., Sondergeld, C.H., and Rai, C.S. 2010. Structural Characterization of Gas Shales on the Micro- and Nano-Scales. Paper SPE 137693 presented at the Canadian Unconventional Resources and International Petroleum Conference, Calgary, Canada, 19-21 October.
18. Curtis, M.E., Ambrose, R.J., Sondergeld, C.H. and Rai, C.S. 2011. Investigation of the Relationship between Organic Porosity and Thermal Maturity in the Marcellus Shale. Paper SPE 144370 presented at the North American Unconventional Gas Conference and Exhibition, Woodlands, Texas, 14-16 June.
19. Curtis, M.E., Cardott, B.J., Sondergeld, C.H., and Rai, C.S. 2012. The Development of Organic Porosity in the Woodford Shale Related to Thermal Maturity. Paper SPE 160158 presented in SPE Annual Technical Conference and Exhibition, San Antonio, Texas, 8-10 October.
20. Dow, W.G. 1977. Kerogen Studies and Geological Interpretations. Journal of Geochemical Exploration. 7: 79-99.
21. Durand, B. 1980. Kerogen: Insoluble Organic Matter from Sedimentary Rocks. Editions TECHNIP, Jan 1, 1980, Paris.
22. Espitalie, J. 1977. Source Rock Characterization Method for Petroleum Exploration. Paper OTC 2935 presented at the 9th Annual OTC, Houston, Texas, 2-5 May.
23. Espitalie, J., Deroo, G., and Marquis, F. 1985. La pyrolyse Rock-Eval et ses Applications, partie I. Rev. Inst. Fr. Pet., **40**: 563-579

24. Eseme, E., Urai, J. L., Krooss, B. M., and Littke, R. 2007. Review of Mechanical Properties of Oil Shales: Implications for Exploitation and Basin Modeling: Oil Shale, Vol. 24, No. 2.
25. Faraj, B., Williams, H., Addison, G., and McKinstry, B. 2004. Gas Potential of Selected Shale Formations in the Western Canadian Sedimentary Basin. *Gas TIPS* **10**(1): 21-25
26. Fischer-Cripps, A.C. 2011. *Nanoindentation.* New York: Springer-Verlag.
27. Griffiths, P.R. and De. Haseth, J.A., *Fourier Transform Infrared Spectrometry*, 2nd Ed., 2007, New Jersey: John Wiley and Sons.
28. Guo, J., and Liu, Y. 2012. Modeling of proppant Embedment: Elastic Deformation and Creep Deformation. Paper SPE 157449 presented at the SPE International Production and Operations Conference and Exhibition, Doha, Qatar, 14-16 May 2012.
29. Gupta, N. 2012. Multi-scale Characterization of the Woodford Shale in West-Central Oklahoma: From Scanning Electron Microscope to 3D Seismic. PhD Dissertation, University of Oklahoma, Norman, Oklahoma, USA.
30. Harper, C. A. 2001. *Handbook of Ceramics, Glasses and Diamonds*. The McGraw-Hill Companies, Inc.
31. Havens, J. Mechanical Properties of the Bakken Formation, MS Thesis, Colorado School of Mines, Golden.
32. Hay, J.L, and Pharr, G.M. 2000. *Instrumented Indentation Testing*. ASM Handbook, 232-243.

33. Hornby, B.E. 1998. Experimental Laboratory Determination of the Dynamic Elastic Properties of Wet, Drained Shales. Journal of Geophysical Research **103**: 29945-29964.

34. Hunt, J.M. 1979, 1996. *Petroleum Geochemistry and Geology*. 2nd Edition. USA. W. H. Freeman and Company.

35. INTEK Shale Report, 2011. Review of Emerging Resources: US Shale Gas and Shale Oil Plays. **http://www.eia.gov/analysis/studies/usshalegas/pdf/usshaleplays.pdf**

36. Jarvie, D.M. 1991. Total Organic Carbon (TOC) Analysis in Treatise of Petroleum Geology: Handbook of Petroleum Geology: Source and Migration Processes and Evaluation Techniques. AAPG Press, Tulsa, USA.

37. Jarvie, D.M. 2004. Evaluation of Hydrocarbon Generation and Storage in Barnett Shale, Ft. Worth Basin, Texas, Humble Geochemical Services Presentation (Unpublished).

38. Jones, L.E.A., and Wang, H.F. 1981. Ultrasonic velocities in Cretaceous Shales from the Williston Basin. Geophysics **46**: 288-297.

39. Kale, S. 2009. Petrophysical Characterization of Barnett Shale Play. MS Thesis, University of Oklahoma, Norman, USA

40. Karastathis A. 2007. Petrophysical Measurements on a Tight Gas Shale. MS Thesis, University of Oklahoma, Norman.

41. Katahara, K.W., 1996. Clay Mineral Elastic Properties. 66th Annual International Meeting, SEG, Expanded Abstratcs, 1691-1694.

42. Kaufmann, E. N. 2003. *Characterization of Materials*. Volume 1, John Wiley and Sons, Inc.

43. King, G.E. 2010. Thirty years of gas shale fracturing: What have we learned?. SPE 133456 presented in SPE Annual Technical Conference and Exhibition, Florence, Italy, 19-22 September 2010.

44. Kuhn, H., Medlin, D. 2000. *ASM Handbook: Mechanical Testing and Evaluation*. Volume 8, ASM International, October 2000.

45. Kumar, V. 2012 (a). Geomechanical Characterization of Shales Using Nanoindentation. MS Thesis, University of Oklahoma, Norman, USA.

46. Kumar, V., Sondergeld, C.H., and Rai, C.S. 2012 (b). Nano to Macro Mechanical Characterization of Shale. SPE 159804 presented in SPE Annual Technical Conference and Exhibition, San Antonio, Texas, 8-10 October 2012.

47. Kumar V., Curtis, M.E., Gupta, N., Sondergeld, C.H., and Rai, C.S. 2012 (c). Estimation of Elastic Properties of Organic Matter and Woodford Shale through Nanoindentation Measurements. SPE 162778 presented in SPE Canadian Unconventional Resources Conference, Calgary, Alberta, Canada, 30 October – 1 November 2012.

48. Lempp, Ch., Natau, O., Bayer, U., Welte, D. H. 1994. The Effect of Temperature on Rock Mechanical Properties and Fracture Mechanisms in Source Rocks – Experimental Results. Paper SPE 28039 presented at the SPE/ISRM Rock Mechanics in Petroleum Engineering Conference, Delft, The Netherlands, 29-31 August.

49. Luo, J., Stevens, R. 1998. Porosity-dependence of elastic moduli and hardness of 3Y-TZP ceramics. Ceramics International 25 (1999) 281-286.

50. Marz, T., DuBow, J., and Rashejuar, K. 1983. Acoustic Wave Propagation in Oil Shale. FUEL, Vol. 62, October.

51. Moustafa, M., Malek, S., and Jianfu, S. 2008. Experimental Study of the Thermomechanical Behavior of the Petroleum Reservoir. Paper SPE 116953 presented at the 2008 SPE Eastern Regional/AAPG Eastern Section Joint Meeting, Pittsburg, Pennsylvania, 11-15 October.

52. Mavko, G., Mukerji, T., and Dvorkin, J. 2003. *The Rock Physics Handbook*, 1st Ed., Cambridge, UK: Cambridge University Press.

53. Mba, K.C., and Prasad, M. 2010. Mineralogy and its Contribution to Anisotropy and Kerogen Stiffness Variations with Maturity in the Bakken Shales. SEG extended abstract presented at Annual meeting, Denver, Colorado, USA. 17-22 October.

54. Navigant Consulting Inc (NCI), 2008, North American Natural Gas Supply Assessment, prepared for US Department of Energy's 2009 Annual Energy Outlook.

http://www.afdc.energy.gov/adfc/pdfs/ng_supply_assessment_2.pdf

55. Network for Excellence in Training (NExT), 2008. Course notes

56. Oliver, W.C., and Pharr, G.M. 2004. Measurement of Hardness and Elastic Modulus by Instrumented Indentation: Advances in Understanding and Refinements in Technology. J. Mater. Res. 19(1): 3-20.

57. Oliver, W.C. and Pharr, G.M. 1992. An Improved Technique for Determining Hardness and Elastic Modulus using Load and Displacement Sensing Indentation Experiments, J. Mater. Res. 7(6), 1564-1583, 1992.

58. Ortega, J.A., Ulm, F.J. 2010. A Multi-scale Micromechanics Framework for Shale using nano-tools. Paper ARMA 10-450 presented at the 44th US Rock Mechanics Symposium and 5th US-Canada Rock Mechanics Symposium, Salt Lake City, UT, 24-27 June 2010.

59. Parker, E. R. 1967. *Materials Data Handbook for Engineers and Scientists*. McGraw-Hill Book Company.

60. Passey, Q.R., Creaney, S., Kulla, J.B., Moretti, F.J., and Stroud, J.D. 1990 AAPG Bulletin 74 (12): 1777-1794.

61. Passey, Q.R., Bohacs, K.M., Esch, W.L., Klimentidis, R., and Sinha, S. 2010. From Oil-Prone Source Rock to Gas-Producing Shale reservoir – Geologic and Petrophysical Characterization of Unconventional Shale-Gas Reservoirs. Paper SPE 131350 presented at the CPS/SPE International Oil and Gas Conference and Exhibition in China, Beijing, China, 8-10 June.

62. Pollastro, R.M., Cook, T.A., Roberts, L.N.R., Schenk, C.J., Lewan, M.D., Anna, L.O., Gaswirth, S.B., Lillis, P.G., Klett, T.R., Charpentier, R.R. 2008. Assessment of undiscovered oil resources in the Devonian-Mississipian Bakken formation, Williston basin province, Montana and North Dakota, Fact sheet. US Geological Survey, Report FS 2008-3021:2.

63. Prasad, M. 2001. Mapping Impedence Microstructures in Rocks with Acoustic Microscopy, The Leading Edge 20: 172-179.

64. Prasad, M., Hofmann, R., and Batzle, M. 2005. Values of Mineral Modulus of Clay. Presented at SEG Annual Meeting, Houston.

65. Prasad, M., Mba, K.C., McEvoy, T.E., Batzle, M.L. 2009. Maturity and Impedance Analyses of Organic-Rich Shales. Paper SPE 123531 presented at SPE Rocky Mountain Petroleum Technology Conference, Denver, Colorado, 14-16 April.

66. Prothero D.R. and Schwab F. 2004. *Sedimentary Geology: An Introduction to Sedimentary Rocks and Stratigraphy*. 2nd Ed. New York: W.H. Freeman.

67. Rai, C.S., and Sondergeld, C.H. 2011. Seismic Reservoir Modeling PE 6283, Course Notes, University of Oklahoma, Norman, USA

68. Rongzun, H., Zuhui, Z., and Jingen, D. 1987. The Creep Characteristics of Shale Formation and the Analysis of its Loading on the Oil Well Casing. Paper 6CONGRESS-1987-024 presented at the 6th ISRM Congress, Montreal, Canada, 30 August-3 September 1987.

69. Sarkar, M. 2008 Petrophysical Study of Shales under High Temperature and Pressure. MS Thesis, University of Oklahoma, Norman, USA.

70. Sayers, C.M. 2008. The effect of Low Aspect Ratio Pores on the Seismic Anisotropy of Shales. Paper SEG 2008-2750 presented in SEG Annual Meeting, Las Vegas, Nevada, 9-14 November.

71. Sayers, C. M. 2010. The effect of anisotropy on the Young's Moduli and Poisson's Ratio of Shales. Paper SEG 2010-2606 presented in SEG Annual Meeting, Denver, Colorado, 17-22 October.

72. Sayers, C. M. 2013. The Effect of Kerogen on the Elastic Anisotropy of Organic-Rich Shales. Geophysics, Vol. 78, No. 2. March-April 2013.

73. Schmoker, J.W. and Hester, T.C. 1983. Organic Carbon in Bakken Formation, United States portion of Williston Basin. American Association of Petroleum Geologists Bulletin 67 (12): 2165-2174.

74. Schuh, C.A., Packard, C.E., and Lund, A.C. 2006. Nanoindentation and Contact-Mode Imaging at High Temperatures. J. Mater. Res., Vol 21, No. 3, March.

75. Screiber, E., Andersen, O., Soga, N. 1973. Elastic Constants and their Measurements, McGraw-Hill, New York.

76. Sharma, A. 2013. Acoustic Mapping and Microscopic Analysis of Laboratory Induced Hydraulic Fracture under Triaxial Conditions. MS Thesis, University of Oklahoma, Norman

77. Shukla, P., Kumar, V., Curtis, M.E., Sondergeld, C.H., and Rai, C.S. 2013. Nanoindentation Studies on Shales. Paper ARMA 13-578 presented at 47th US Rock Mechanics/Geomechanics Symposium, San Francisco, CA, USA 23-26 June. (Unpublished)

78. Simmons, G., and Wang, H. 1971. *Single Crystals Elastic Constants and Calculated Aggregate Properties: A Handbook.* Cambridge: The MIT Press.

79. Sondergeld, C.H., and Rai, C.S. 1993. A New Concept of Quantitative Core Characterization, The Leading Edge, V.12 (7): 774-779.

80. Sondergeld, C.H., Rai, C.S., Margesson, R.W., and Whidden, K.J. 2000. Ultrasonic Measurements of Anisotropy on Kimmeridge Shale. Extended abstract, SEG, 78th Annual International meeting, Calgary, Canada, 6-11 August.

81. Sondergeld, C.H., Ambrose, R.J., Rai, C. S., Moncrieff, J. 2010. Micro-Structural Studies of Gas Shales. Paper SPE 131771-MS presented at the SPE Unconventional Gas Conference, Pittsburgh, Pennsylvania, USA, 23-25 February.

82. Sondergeld, C.H., and Rai, C.S. 2011. Elastic Anisotropy of Shales. The Leading Edge **30**: 324-331.

83. Sone, H., and Zoback, M.D. 2010. Strength, Creep and Frictional Properties of Gas Shale Reservoir Rocks. Paper ARMA 10-463 presented at 44th US Rock Mechanics Symposium and 5th US Canada Rock Mechanics Symposium, Salt Lake City, Utah, 27-30 June 2010.

84. Taylor, W. E., Cooke, M. 1949. Correlation of the Mohs's Scale of Hardness with the Vickers's Hardness Numbers. Journ. Inst. Metals, 1948, Vol 74, p. 493 and Nature, 1949, Vol. 163, p. 323.

85. Tissot, B., Bard, J.F., and Espitalie, J. 1980. Principal Factors Controlling the Timing of Petroleum Generation. In A.D. Miall, ed., Facts and Principles of World Petroleum Occurrence: Canadian Society of Petroleum Geologist Memoir **6**: 143-152

86. Vernik, L. and Nur, A.1992. Ultrasonic Velocity and Anisotropy of Hydrocarbon Source Rocks. Geophysics **57**: 727-735.

87. Vernik, L., and Landis, C., 1996. Elastic Anisotropy of Source Rocks: Implications for Hydrocarbon Generation and Primary Migration. Bulletin of the American Association of Petroleum Geologists **80**: 531-544.

88. Vernik, L., and Liu, X. 1997. Velocity Anisotropy in Shales: A Petrophysical Study. Geophysics **62**: 521-532.

89. Wang, Z., Wang, H., and Cates, M.E. 2001. Effective Elastic Properties of Solid Clays: Geophysics, 66, 428-440.

90. Zargari, S., Prasad, M., Mba, K.C. and Mattson, E.D. 2011. Organic Maturity, Hydrous Pyrolysis and Elastic Property in Shales. Paper SPE 149403 presented at the 11th Canadian Unconventional Resources Conference, Alberta, Canada, 15-17 November.

91. Zeszotarski, J.C., Chromik, R.R., Vinci, R.P., Messmer, M.C., Michels, R. and Larsen, J.W. 2004. Imaging and Mechanical Property Measurements of Kerogen via Nano-indentation.Geochimica Acta **68**(20): 4113-4119.

Appendix A: Crossplots for Shales

As discussed in Chapter 4, plots for Young's modulus versus composition have been presented here for Wolfcamp shale. Plots have also been presented for compositional dependence of Young's modulus in different ranges of Young's modulus.

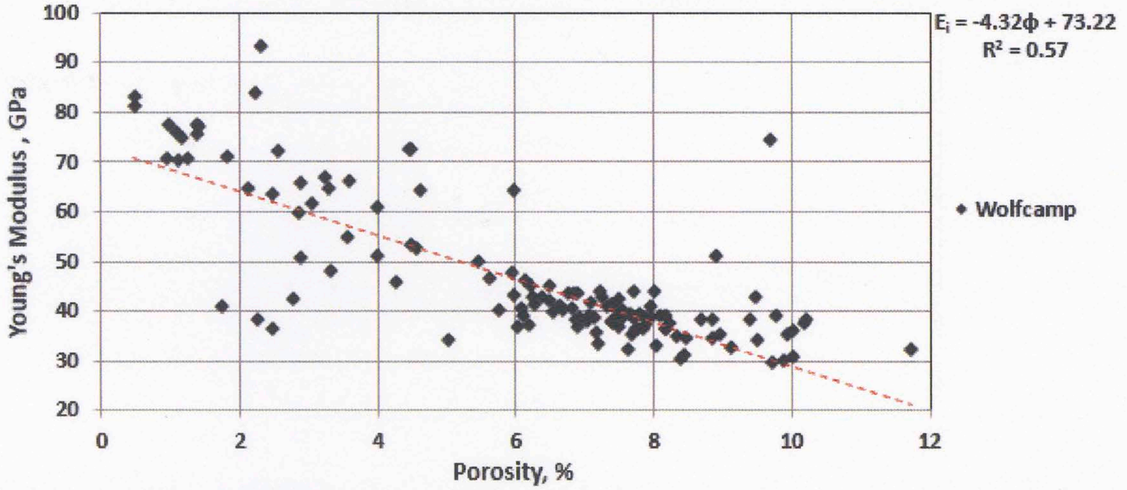

Figure 110: Crossplot of E_i versus porosity for Wolfcamp shale. Young's modulus is inversely proportional to porosity described by the equation E_i=73.22-4.32ϕ. 57% correlation is observed. More scatter is observed in the data at high porosity.

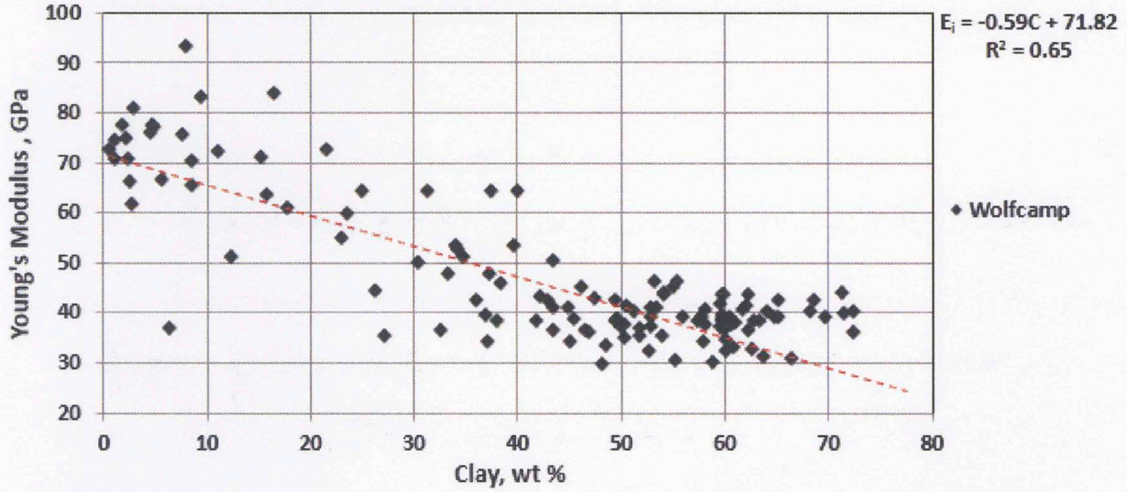

Figure 111: Crossplot of E_i versus clay content for Wolfcamp shale. Young's modulus is inversely proportional to clay content described by the equation E_i=71.82-0.59C. 65% correlation is observed. Less scatter is observed in the data at high clay content.

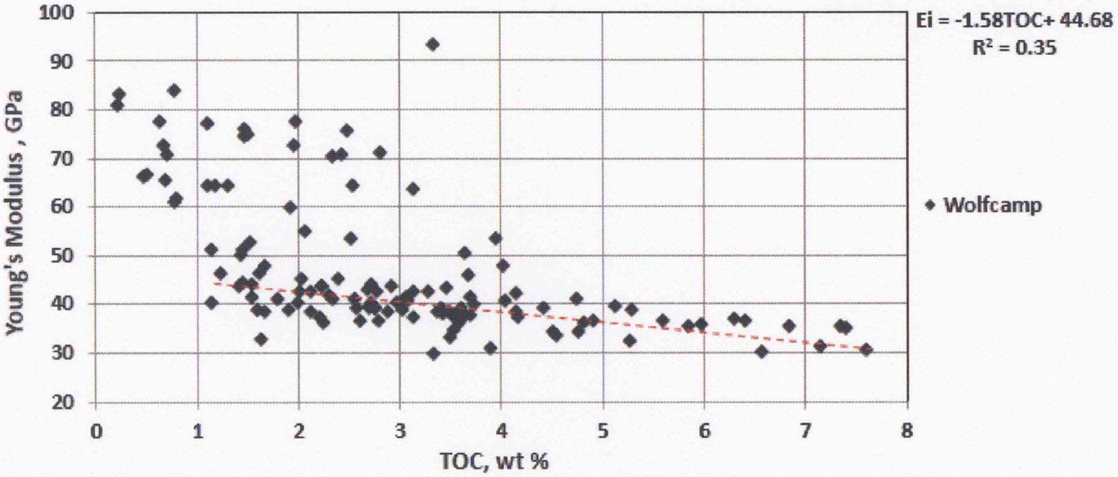

Figure 112: Crossplot of E_i versus TOC for Wolfcamp shale. Plot ignores samples with E_i>50 GPa and TOC<2%. Young's modulus is inversely proportional to organic content described by the equation E_i=44.68-1.58TOC. Less scatter in the data is observed at high TOC. 35% correlation is observed.

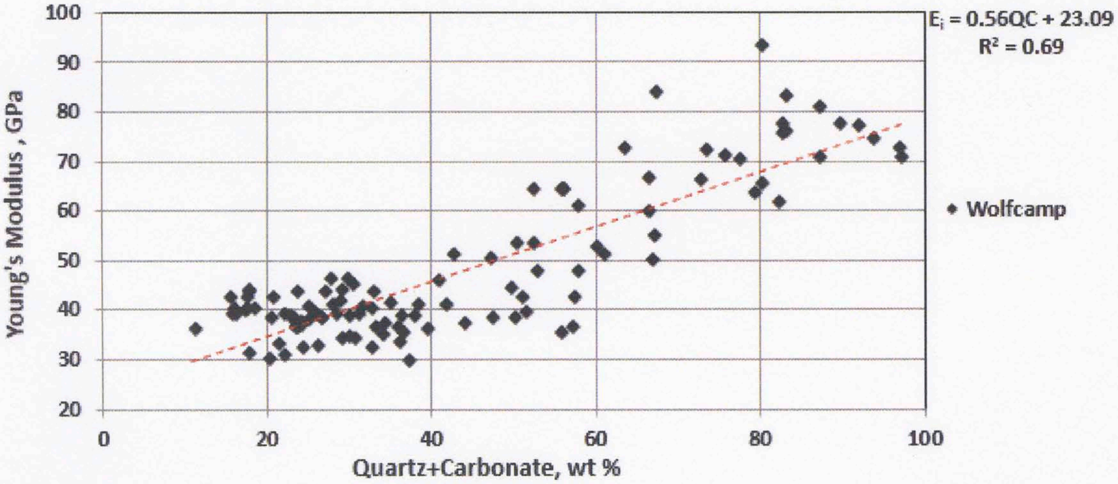

Figure 113: Crossplot of Ei versus quartz+carbonate content for Wolfcamp shale. Young's modulus is directly proportional to quartz+carbonate content described by the equation 23.09+0.56QC. 69% correlation was observed.

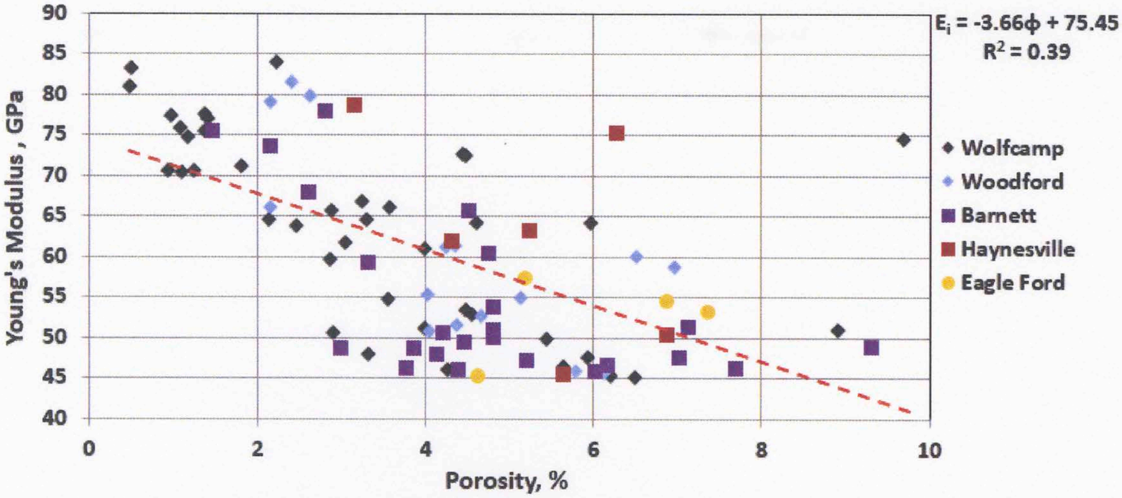

Figure 114: Crossplot of E_i versus porosity for all shale samples with horizontal Young's modulus greater than 45 GPa. Young's modulus is inversely proportional to porosity described by the equation E_i=75.45-3.66ϕ. 39% correlation was observed.

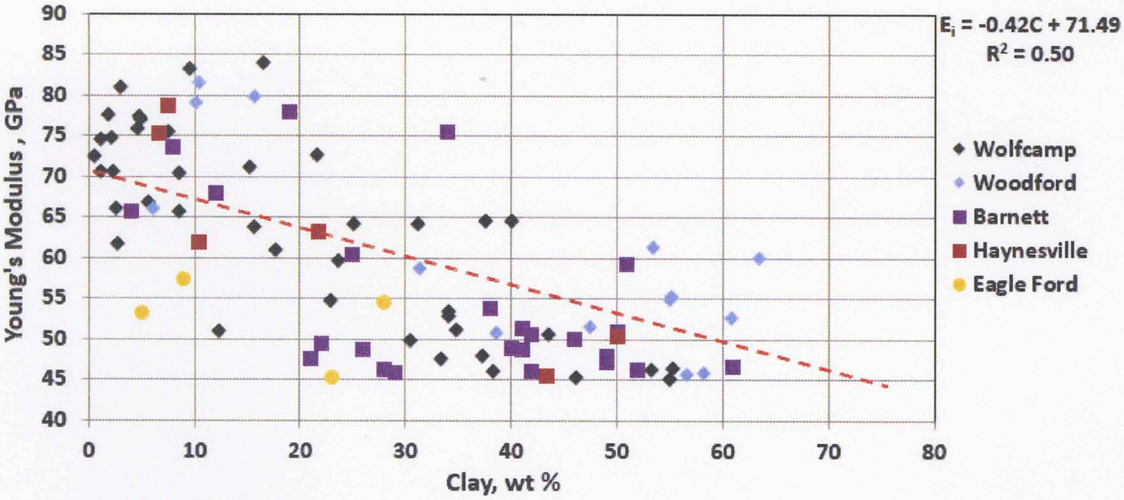

Figure 115: Crossplot of E_i versus clay content for all shale samples with horizontal Young's modulus greater than 45 GPa. Young's modulus is inversely proportional to clay content described by the equation E_i=71.49-0.42C. 50% correlation was observed.

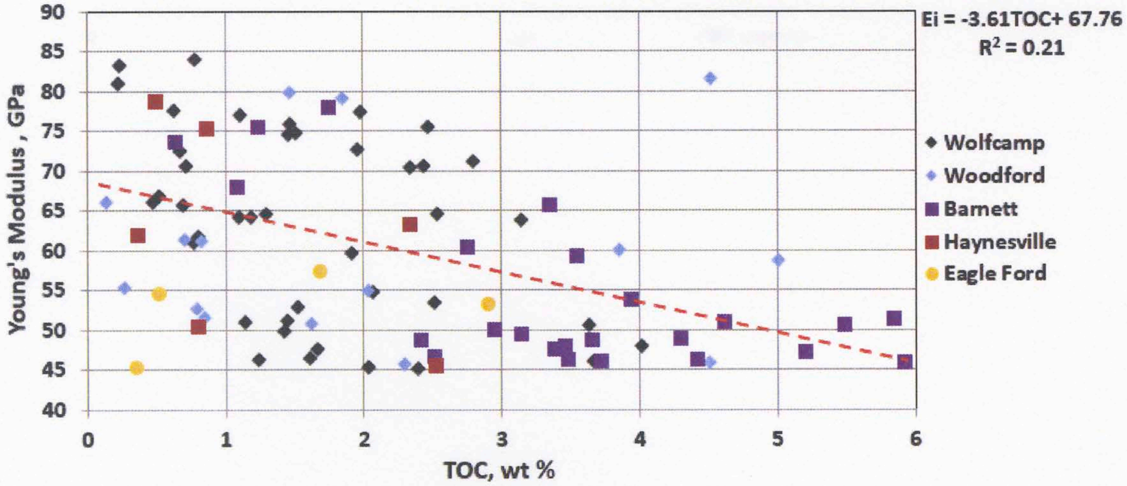

Figure 116: Crossplot of E_i versus TOC for all shale samples with horizontal Young's modulus greater than 45 GPa. Young's modulus is inversely proportional to TOC described by the equation E_i=67.76-3.61TOC. 21% correlation was observed.

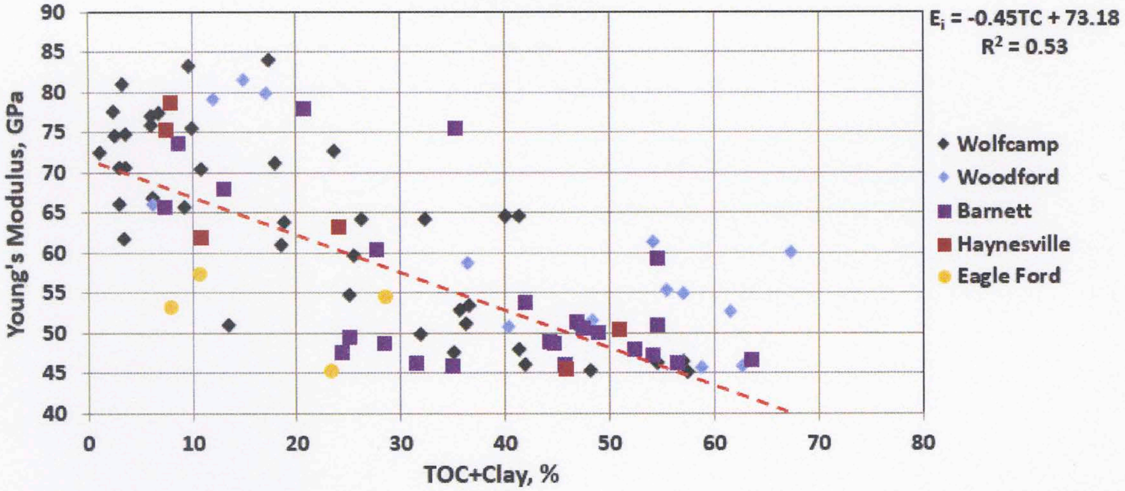

Figure 117: Crossplot of E_i versus TOC+clay for all shale samples with horizontal Young's modulus greater than 45 GPa. Young's modulus is inversely proportional to TOC+Clay described by the equation E_i=73.18-0.45TC. 53% correlation was observed.

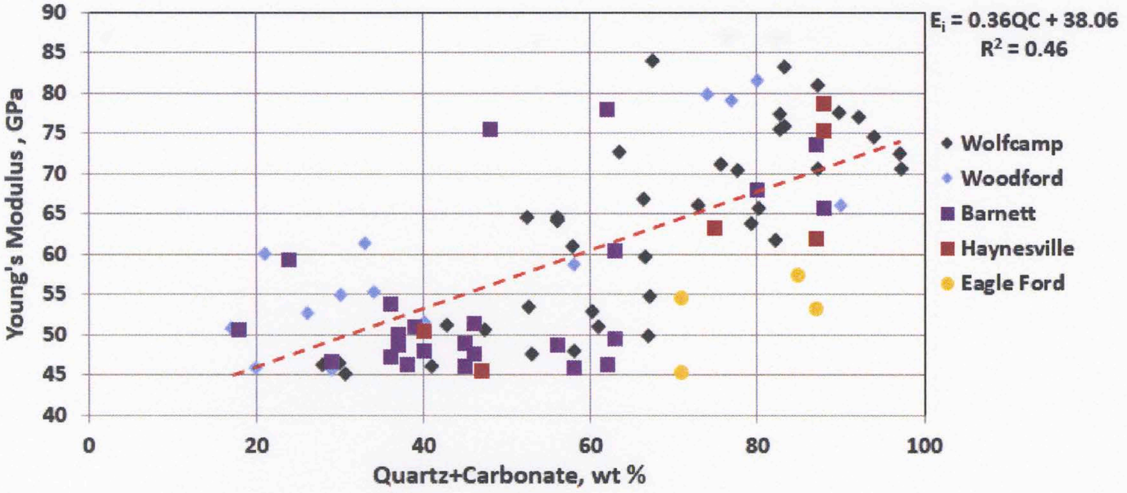

Figure 118: Crossplot of E_i versus quartz+carbonate content for all shale samples with horizontal Young's modulus greater than 45 GPa. Young's modulus is directly proportional to quartz+carbonate described by the equation $E_i=38.06+0.36QC$. 46% correlation was observed.

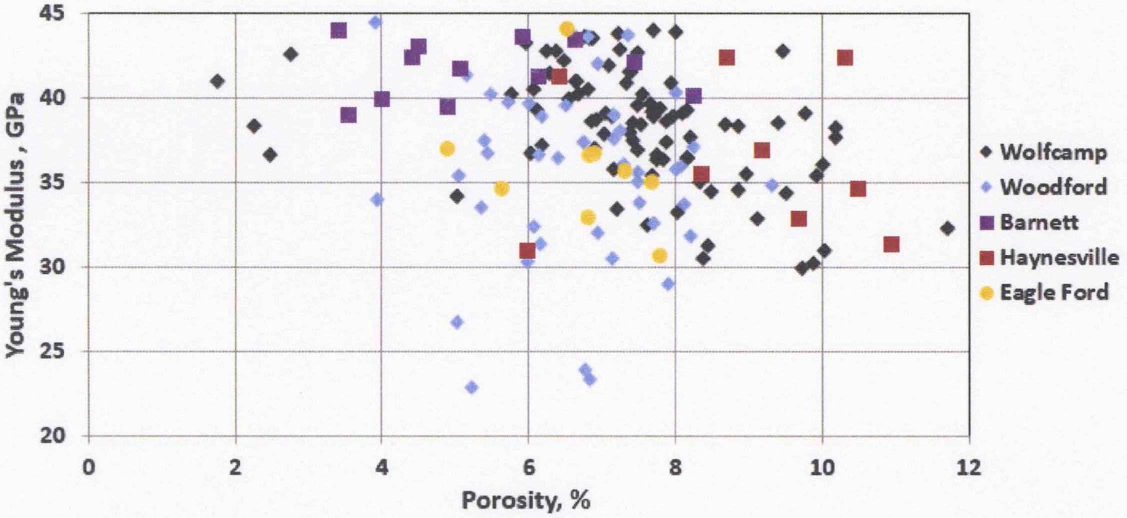

Figure 119: Crossplot of E_i versus porosity for all shale samples with horizontal Young's modulus less than 45 GPa. No correlation was observed.

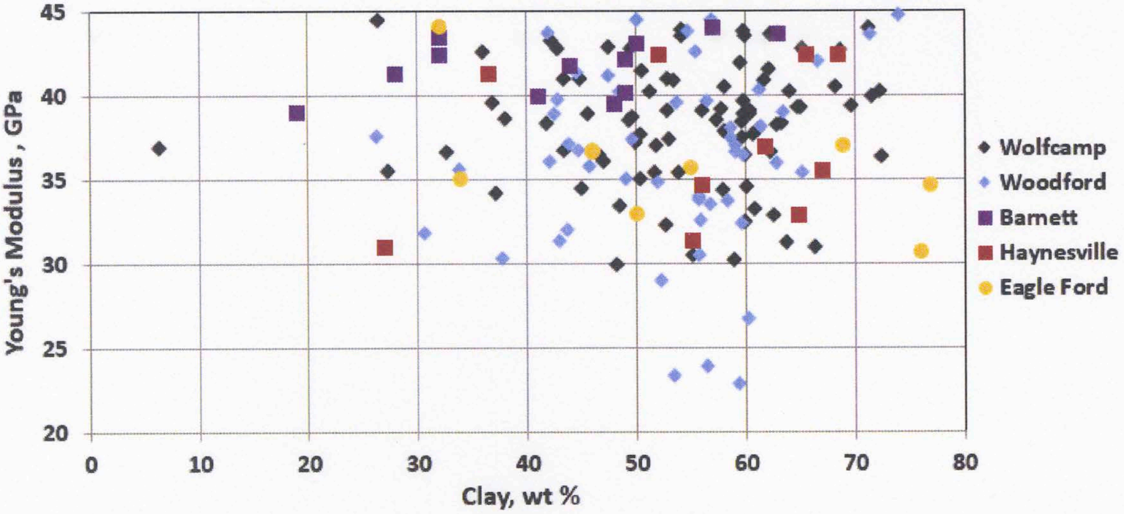

Figure 120: Crossplot of E_i versus clay content for all shale samples with horizontal Young's modulus less than 45 GPa. No correlation was observed.

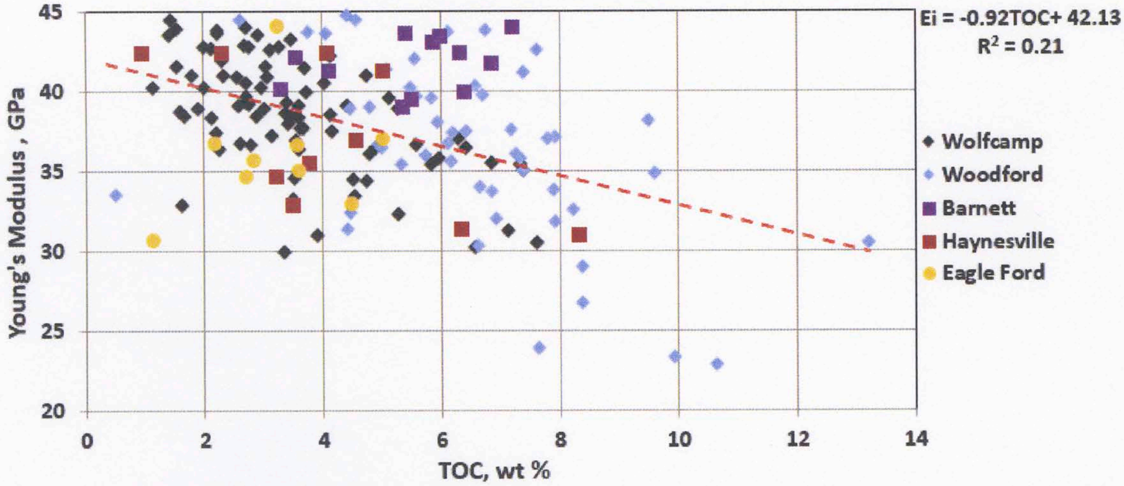

Figure 121: Crossplot of E_i versus clay TOC for all shale samples with horizontal Young's modulus less than 45 GPa. No correlation was observed.

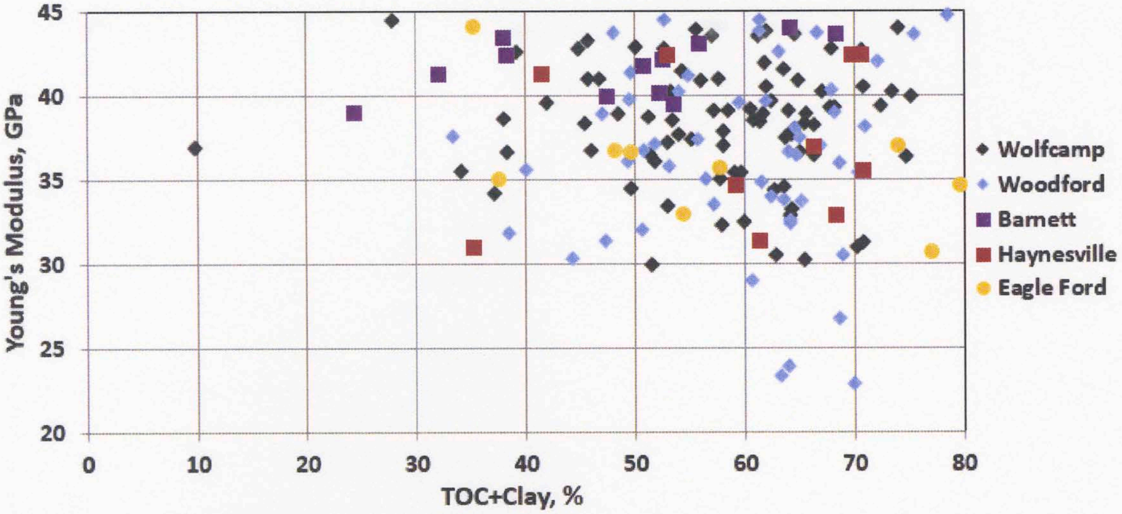

Figure 122: Crossplot of E_i versus TOC+clay for all shale samples with horizontal Young's modulus less than 45 GPa. No correlation was observed.

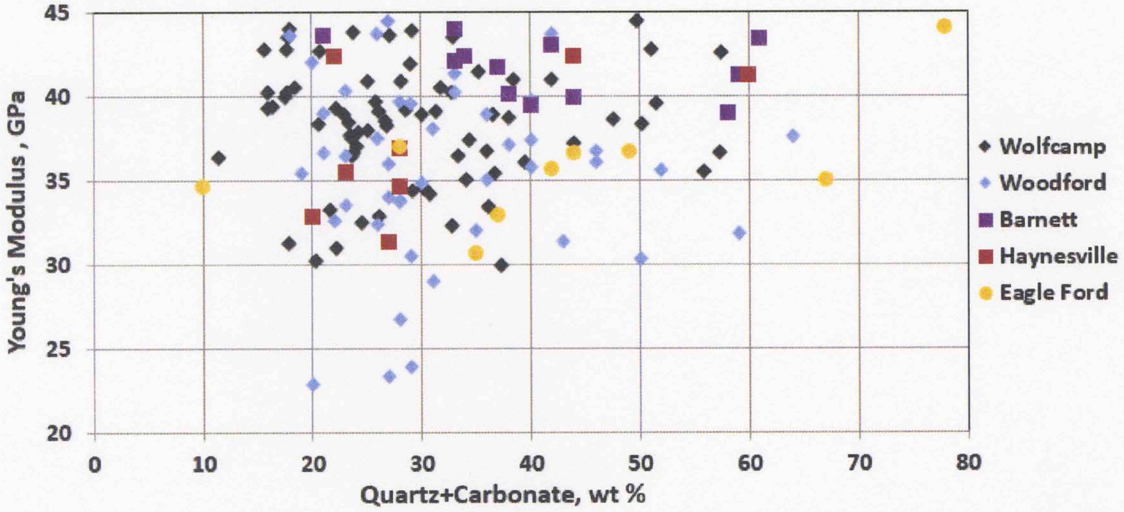

Figure 123: Crossplot of E_i versus quartz+carbonate content for all shale samples with horizontal Young's modulus less than 45 GPa. No correlation was observed.